



Terms and Conditions of Use of Digitised Theses from Trinity College Library Dublin

Copyright statement

All material supplied by Trinity College Library is protected by copyright (under the Copyright and Related Rights Act, 2000 as amended) and other relevant Intellectual Property Rights. By accessing and using a Digitised Thesis from Trinity College Library you acknowledge that all Intellectual Property Rights in any Works supplied are the sole and exclusive property of the copyright and/or other IPR holder. Specific copyright holders may not be explicitly identified. Use of materials from other sources within a thesis should not be construed as a claim over them.

A non-exclusive, non-transferable licence is hereby granted to those using or reproducing, in whole or in part, the material for valid purposes, providing the copyright owners are acknowledged using the normal conventions. Where specific permission to use material is required, this is identified and such permission must be sought from the copyright holder or agency cited.

Liability statement

By using a Digitised Thesis, I accept that Trinity College Dublin bears no legal responsibility for the accuracy, legality or comprehensiveness of materials contained within the thesis, and that Trinity College Dublin accepts no liability for indirect, consequential, or incidental, damages or losses arising from use of the thesis for whatever reason. Information located in a thesis may be subject to specific use constraints, details of which may not be explicitly described. It is the responsibility of potential and actual users to be aware of such constraints and to abide by them. By making use of material from a digitised thesis, you accept these copyright and disclaimer provisions. Where it is brought to the attention of Trinity College Library that there may be a breach of copyright or other restraint, it is the policy to withdraw or take down access to a thesis while the issue is being resolved.

Access Agreement

By using a Digitised Thesis from Trinity College Library you are bound by the following Terms & Conditions. Please read them carefully.

I have read and I understand the following statement: All material supplied via a Digitised Thesis from Trinity College Library is protected by copyright and other intellectual property rights, and duplication or sale of all or part of any of a thesis is not permitted, except that material may be duplicated by you for your research use or for educational purposes in electronic or print form providing the copyright owners are acknowledged using the normal conventions. You must obtain permission for any other use. Electronic or print copies may not be offered, whether for sale or otherwise to anyone. This copy has been supplied on the understanding that it is copyright material and that no quotation from the thesis may be published without proper acknowledgement.

**An asperity deformation model for the sliding
cylinder problem: theoretical and
experimental investigations**

Magali Busquet

Department of Mechanical Engineering,
Trinity College,
Dublin 2,
Ireland.

2000

A thesis submitted to the University of Dublin in partial
fulfilment of the requirements for the degree of Ph. D.

TRINITY COLLEGE
10 JUL 2000
LIBRARY DUBLIN

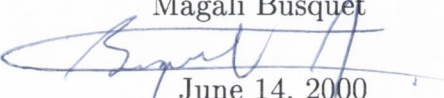
THESIS
5738

Declaration

I declare that I am the sole author of this thesis and that all the work presented in it, unless otherwise referenced, is my own. I also declare that this work has not been submitted, in whole or in part, to any other university or college for any degree or other qualification.

I authorise the library of the University of Dublin to lend this thesis.

Magali Busquet



June 14, 2000

Abstract

Statistical analysis shows that the main reason for the failure of machines is not breakage but wear of the moving parts resulting from rubbing stress. Although the laws of friction are fairly well substantiated, there are still no satisfactory quantitative laws of wear.

However, significant progress has been made in calculating how asperity contacts strain a wearing surface and in estimating how this may relate to wear rates. Among many attempts to develop quantitative models, the rigid-plastic approach neglects elastic effects and allows slipline field theory to be used. Combining this with a damage rule, wear rates can be predicted from the strain calculations and the mechanical properties of the wearing material. In this theory, the hard asperity is represented as a rigid wedge, which is a limitation. Real asperities are more likely to have rounded tips and a more realistic approach is to model them with cylinders.

The present investigation proposes a new rigid-plastic asperity contact, which models a wave of plastically deformed material pushed ahead of a cylinder. This model is valid for small values of surface roughness parameters and good lubrication conditions. For given loading and lubrication conditions, this model is able to predict the friction coefficient and the strains involved within each pass of the asperity. Maps are provided in this thesis, which give calculated friction coefficients and strains for a wide range of roughness and lubrication conditions.

Scaled-up model asperity experiments are presented, where a rigid cylinder slides across two non-ferrous metals. It is shown that friction is influenced

by both elastic effects and the presence of a third body layer, trapped at the interface between the cylinder and the soft metal. Slipline field theory predicts friction satisfactorily above a given load, whose value depends on the degree of elasticity of the deforming material and on the lubrication parameter. Below this load, elastic effects cannot be neglected to predict friction. Experiments are also performed with a cut cylinder, whose trailing side has been removed which show that, under this new configuration both elastic effects and the influence of a third body layer are reduced. Slipline field theory can predict friction well for the two materials tested.

When compared with the measured strains observed after model asperity experiments in previous work, our numerical model appears to predict well the highly strained layer near the surface. This new model provides thus a new quantitative tool to relate calculated strains to the detachment of particles.

Acknowledgements

I wish to thank:

Professor A.A. Torrance for welcoming me to his team and for his advice, patience and guidance throughout this work. I am also very thankful for his availability and support until the end of this thesis.

Late Professor P.L.B. Oxley for his interest and involvement in this work. I am sincerely in debt for the help and encouragement he gave me during his several visits to Dublin.

The technical staff at the Mechanical department, especially Tom Haveron, Paul Normoyle and Peter O'Reilly. Special thanks to Tom Haveron who taught me first how to use a screwdriver but especially for the invaluable technical support he provided me in my experimental work.

The “solid third body” team of the Laboratoire de Mécanique des Contacts, I.N.S.A., Lyon, especially Dr. Sylvie Descartes, Professor Yves Berthier and Claude Godeau for collaboration and for welcoming me to their team.

Dr. Michael Carley for this thesis. His permanent concern for detail was an invaluable help with this thesis (cinq verres en moins).

Dr. Sylvie Plumet, Dr. Sylvie Descartes, Damien Lacroix, Dr. Yanyi

Yang, Dr. Josette Galligan and Danny Bellett for the fructuous discussions we had, their advice and help with this thesis.

The postgrad team at the Mechanical department for having pretended sometimes to understand my brilliant English, for Friday nights, for week-ends.

My friends from Dublin.

My friends from Lyon.

My parents and my sisters.

Contents

General Introduction	1
1 Relating surface strains to a wear model	5
1.1 Introduction	5
1.2 Elastic-plastic models	7
1.2.1 The theory of strain in rolling contact	7
1.2.2 Extension to sliding wear calculations	9
1.3 Rigid-plastic models	10
1.3.1 Friction calculation	10
1.3.2 Strain calculation	16
1.3.3 Mild wear calculations	18
1.3.4 Limits of rigid-plastic models	20
1.4 Boundary friction with fatty acids	22
1.4.1 Stearic acid as a boundary lubricant	22
1.4.2 Boundary friction	22
1.4.3 Limits of boundary lubrication models	25
2 Analysis of the methods for constructing a slipline field	27
2.1 The slipline field theory	27
2.2 Methods available for constructing a slipline field: Choice of an approach for the present problem	31
2.2.1 Introduction	31
2.2.2 The trial and error process	32

2.2.3	Methods available to assist with the trial and error process	33
2.2.4	Conclusion: choice of a method	35
2.3	The numerical calculation of slipline field	35
2.4	Requirements for a complete solution	37
3	Theoretical analysis: development of a slipline field for the sliding cylinder problem	40
3.1	The general slipline field structure and method of construction	40
3.1.1	General features of the field	40
3.1.2	Boundary Conditions	42
3.1.3	Construction of the slipline field solution	43
3.1.4	Construction of the velocity field	44
3.2	Details of the programme	45
3.2.1	General organisation and flow diagram for the programme	45
3.2.2	Slipline field computations	47
3.2.3	Velocity field computations	49
3.2.4	Optimization	50
3.2.5	Computation of stresses and friction coefficient	51
3.2.6	Checks on plastic work	52
3.3	Strain analysis	52
3.3.1	Deformed grid generation	53
3.3.2	Strain calculation	54
4	Results of the model	58
4.1	Main features of the solution	58
4.1.1	The slipline field and velocity field solution	58
4.1.2	Optimization	60
4.1.3	Limitations of the model	62
4.2	Friction results	63

4.2.1	Evolution of friction as a function of θ , the angle of the interface and f , the Tresca factor.	63
4.2.2	Comparison with the chord approximation model developed by Challen and Oxley [1]	66
4.3	Strain results	69
4.3.1	Deformation of a grid	69
4.3.2	Strain calculation	71
4.3.3	Comparison with finite element analysis	74
5	Experimental methods	79
5.1	Experimental investigation of a hard cylinder in C.B.N. sliding across two non-ferrous metals	80
5.1.1	Objectives	80
5.1.2	Experimental set-up	80
5.1.3	Experimental procedure	85
5.1.4	Test conditions and parameters involved	85
5.2	The visualisation investigation	86
5.2.1	Principles of the visualisation technique	86
5.2.2	Objectives for the present work	88
5.2.3	Experimental set-up	88
5.2.4	Experimental procedure	92
5.2.5	Test conditions	94
6	Experimental results	95
6.1	Friction results and observations when a hard cylinder in C.B.N. slides across two non-ferrous metals	96
6.1.1	Full cylinder tests: S_1	96
6.1.2	Cut cylinder tests: S_2	100
6.2	Results of the visualisation investigation	103
6.2.1	Introduction: objectives and method	103
6.2.2	Results for aluminium	105

6.2.3	Results for copper	111
6.3	Conclusions	116
6.3.1	Friction results	116
6.3.2	Visualisation results	117
7	Discussion	118
7.1	Friction	118
7.1.1	Introduction	118
7.1.2	Influence of elastic effects	119
7.1.3	Influence of a third body layer at the interface	122
7.1.4	Interpretation of our experimental results	125
7.2	Prediction of Strains	128
7.2.1	Introduction	128
7.2.2	Comparison with strain patterns observed in previous work	130
7.2.3	Comparison with the morphology of wear debris col- lected after wedge experiments	135
7.3	conclusions	136
7.3.1	Friction	136
7.3.2	Strains	137
8	Conclusions	138
8.1	The present investigation	138
8.2	Perspectives	141
	References	143
A	The wave model [2]: friction calculation	153
B	The chord approximation model [1] and the developed chord model [3]: friction calculation	156
B.1	The chord approximation model [1]	156

B.2	The developed chord model [3]	158
C	Geometrical properties of a slipline field - Stress and velocity boundary value problems [4, 5]	161
C.0.1	Hencky's first theorem	161
C.1	Second boundary value problem	162
C.2	Third boundary value problem	164
D	Optimisation of the numerical solution with an ellipse	165
E	Calculation of stresses along the interface and of the friction coefficient μ	167
F	Checks on plastic works	169
G	Strain maps	173
G.1	Evolution of the angle of the interface θ versus (N/kR) for different values of the Tresca factor f	174
G.2	Evolution of the friction coefficient μ with (N/kR) for different values of the Tresca factor f	175
G.3	Evolution of the depth of the deformed layer (h_{max}/R) versus (N/kR) for different values of the Tresca factor f	177
G.4	Evolution of the shear strain (γ_{xy}) versus the depth (h/h_{max}) for $f = 0.3$ and for different loads (N/kR)	179
G.5	Evolution of the shear strain (γ_{α}) versus the depth (h/h_{max}) for $f = 0.3$ and for different loads (N/kR)	182
G.6	Evolution of the maximum shear strains (γ_{xyMAX}) and $(\gamma_{\theta MAX})$ versus the load (N/kR) for different f	185
H	Determination of the Tresca factor f	190
H.1	Test procedure	190
H.2	Friction results	191
H.3	Data	194

H.3.1	Data for aluminium	194
H.3.2	Data for copper	195
I	Velocity accommodation mechanism in a three body contact	196
J	Presentation of the finite element models	198
J.0.3	Description of the models	198
J.0.4	Scheme of the simulations	200
K	Friction data	203
K.0.5	Friction tests on aluminium	204
K.0.6	Friction tests on copper	208
L	Compression tests	212

List of Figures

1.1	Strain cycle induced by a rolling and sliding roller: ϵ_a = reversing strain; γ_r ratchetting strain	8
1.2	Slipline field proposed by Challen and Oxley [2] for the sliding wedge problem	12
1.3	Two views of the plastic wave after wedge shape experiments on copper: (a) A section parallel to wear track and (b) normal to the worn surface. Taken from [6]	14
1.4	Chord approximation model developed by Challen and Oxley [1]	16
1.5	Typical plastic strain cycle induced by a sliding asperity. . . .	17
1.6	Experimental deformed grid after wedge experiments taken from [7]	18
1.7	Mean pressure p_w on front face of wedge versus α for $E^*/Y = 200$ (The solid line is from the analytical model of Torrance et al [8], the dotted line is from slipline field theory [2] and the points are from finite element analysis [8]).	21
1.8	Slipline field proposed by Challen and Oxley [2] for the sliding wedge problem	23
2.1	State of stress and velocity in the α and β slipline directions .	29
2.2	Slipline field proposed by Challen and Oxley [2] for the sliding wedge problem and sketch of a possible solution for the sliding cylinder problem	32
2.3	Trial and error process	33

2.4	Portion of a slipline field subdivided into elemental sections . . .	36
3.1	Sketch of the slipline field	40
3.2	Stress boundary conditions at the interface and at the free surface	43
3.3	Construction of the nodal point of the slipline field	43
3.4	Array to store the data	46
3.5	Procedure of the construction of a solution	48
3.6	Boundary conditions	49
3.7	Generation of the streamlines	53
3.8	Finite strain calculation	55
4.1	Inputs of the simulation	59
4.2	Slipline field solution	59
4.3	Velocity field solution	60
4.4	Evolution of the local errors after the free surface shape corrections	62
4.5	Evolution of the average error with θ	63
4.6	Evolution of θ with N/kR for different f	65
4.7	Evolution of μ with f and N/kR	65
4.8	Comparison between the wave model and the model developed in the present work.	67
4.9	Comparison of the friction predictions of the chord model [1] and the model developed in the present work	68
4.10	Deformation of an initially square grid. $n=100$; $m=100$; $o=100$ and deviations from the constant volume condition	70
4.11	Strain results- $n = 100, m = 100, o = 10—f = 0.25, \theta = 0.2\text{rad.}$	72
4.12	Strain results- $n = 100, m = 100, o = 10—f = 0.25, \theta = 0.2\text{rad.}$	73
4.13	Deformation pattern obtained by finite element analysis with a full cylinder - $N/kR = 1.6, f = 0$	75
4.14	Deformation pattern obtained by finite element analysis with a cut cylinder - $N/kR = 1.3, f = 0$	76

4.15	Comparison between the friction predictions of the finite element analysis our numerical model	77
5.1	Material properties	81
5.2	Bar of tested material	81
5.3	S1 set	83
5.4	S2 set	83
5.5	Schematics of the set-up used	84
5.6	Tribological circuit. Taken from [9]	88
5.7	Geometry of the contact for the visualisation tests	89
5.8	Photographs of the PEDEBA rig.	91
5.9	PEDEBA rig. Taken from [10]	91
5.10	Dynamic observations	92
5.11	Static post-mortem observations	93
5.12	Test conditions	94
6.1	Detached particle accumulation for the full cylinder experiment for aluminium - Top view of the cylinder - $N/kR=0.5$ - Width of the tool=3.15mm	97
6.2	Detached particle accumulation for the full cylinder experiment for copper - Top view of the tool - $N/kR=0.5$ - Width of the tool=3.15mm	97
6.3	Experiments with full cylinders. Aluminium	99
6.4	Experiments with full cylinders. Copper	99
6.5	Detached particle accumulation for the cut cylinder experiments on aluminium - Top view of the tool - $N/kR=0.25$ - width of the tool=3.15mm	100
6.6	Detached particle accumulation for the cut cylinder experiments on copper—Top view of the tool— $N/kR=0.52$ - Width of the tool=3.15mm	101
6.7	Experiments with a cut cylinder: Aluminium	102

6.8	Experiments with a cut cylinder: Copper	103
6.9	Image extracted from a video- Visualisation test on aluminium- N=25N- Average width of the friction track $\simeq 0.7\text{mm}$ - velocity $\simeq 10\text{rev}/\text{min}$	106
6.10	SEM images of the friction track of the crowned disc after the visualisation test on aluminium (see test conditions in figure (5.12))	108
6.11	Optical microscope images of the transparent tool after the vi- sualisation test on aluminium - (a) overview of the contact - (b) zoom of (a)	108
6.12	Detached particle organisation on the transparent tool after the visualisation test and on the C.B.N. cylinder after a blind test ($N/kR = 0.56$)- aluminium	110
6.13	S3M3 sites for the visualisation test and for the blind test - Aluminium	110
6.14	Image extracted from a video- Visualisation test on copper- N $\simeq 25\text{N}$ around- Average width of the friction track $\sim 1.5\text{mm}$ - velocity $\sim 10\text{rev}/\text{min}$	112
6.15	SEM images of the friction track of the crowned disc after the visualisation test on copper	113
6.16	SEM images of the friction track of the crowned disc after the visualisation test on copper	114
6.17	Optical microscope image of the transparent tool - copper	114
6.18	Detached particle organisation on the cylinder after the blind test and on the transparent tool after the visualisation test for copper	115
6.19	S3M3 sites for the visualisation test and for the blind test (full cylinder)—Copper	116

7.1	Comparison between the friction predictions of the elasto-plastic model of Torrance et al [8] and our numerical model- $E/\sigma_y = 300$	121
7.2	Influence of elasticity and a third body layer on the parameter α	123
7.3	Experimental results and the predictions of the elasto-plastic model of Torrance et al [8] - Aluminium	126
7.4	Experimental results and the predictions of the elasto-plastic model of Torrance et al [8] - Copper	127
7.5	Distorted grid predicted - Conditions: $\theta = 0.2rad, f = 0.25$. .	129
7.6	ϵ_{xx} versus γ_{xy} - full line: chord model[1] - Conditions: $\theta = 0.2rad, f = 0.25$	129
7.7	S.E.M. image taken from [6]. Grid size: $100\mu m$	131
7.8	Grid obtained by our model. $\theta = 20^\circ, f = 0.25, k_s = 236MPa$.	132
7.9	Variation of γ_α with depth predicted by our model. $\theta = 20^\circ, f = 0.25, k_s = 236MPa$	132
7.10	Grid taken from [11], $N/kR = 0.7, f = 0.2 - 0.5$, grid size = $100\mu m$	134
7.11	Comparison of γ_α as a function of h/R measured from the grid and calculated from the numerical model for different values of f	134
7.12	Evolution of γ_θ for $\alpha = 2.5$ deg, ($\theta = 0.087$ rad) and $\alpha = 8$ deg, ($\theta = 0.28rad$) for $f = 0.275$	136
A.1	Slipline field proposed by Challen and Oxley [2] for the sliding wedge problem	153
B.1	Chord approximation model developed by Challen and Oxley [1]	158
B.2	The developed chord model	159
B.3	Variation of μ with N/kR for the chord model [1] and the developed chord model for different β_c and $f = 0$	160
C.1	Typical slipline field, demonstrating Hencky's first theorem . .	161

C.2	Second boundary value problem	162
C.3	Third boundary value problem	164
D.1	Boundary conditions for the ellipse	165
E.1	Calculation of stresses at the interface	167
F.1	An element of slipline field showing correct material deformations	169
F.2	Computation of material deformation directions along the free surface	170
F.3	Computation of material deformation directions along the in- terface	171
F.4	Computation of material deformation directions in the field . .	172
G.1	Evolution of the depth of the deformed layer (h_{max}/R) versus (N/kR) for different values of the Tresca factor f	177
G.2	Evolution of the shear strain γ_{xy} versus the depth (h/h_{max}) for $f = 0.3$ and for different loads (N/kR)	179
G.3	Evolution of the shear strain γ_{α} versus the depth (h/h_{max}) for $f = 0.3$ and for different loads (N/kR)	182
G.4	Evolution of the maximum shear strain (γ_{xyMAX}) versus the load (N/kR) for different f	185
G.5	Evolution of the maximum shear strain ($\gamma_{\alpha MAX}$) versus the load (N/kR) for different f	186
H.1	Wedge in C.B.N.	191
H.2	Experiments with wedge-shaped asperities on aluminium . . .	192
H.3	Experiments with wedge-shaped asperities on copper	192
H.4	Particle organisation inside the contact area on the wedge - Aluminium - $W = 500N$	193
H.5	Particle organisation inside the contact area on the wedge - Copper - $W = 500N$	193

I.1	Velocity accommodation in a three-body contact. Taken from [12]	197
J.1	Full cylinder model	199
J.2	Cut cylinder model	199
J.3	Size of the models in mm	200
J.4	dashed line: plot of μ - full line: plot of the effective vertical displacement $\Delta y_e/R$ of the cylinder - versus $\Delta x/R$, the imposed horizontal displacement	202
K.1	Measured normal and frictional forces of a test with a full cylinder on aluminium	204
K.2	Measured normal and frictional forces of a test with a cut cylinder on aluminium	206
K.3	Measured frictional and normal forces of a test with a full cylinder on copper	208
K.4	Measured normal and frictional forces of a test with a cut cylinder on copper	209
L.1	Compression test on aluminium	212
L.2	Compression test on copper	213

List of Tables

4.1	Evolution of the errors with the parameters n and m	61
G.1	Evolution of the angle of the interface θ versus (N/kR) for different values of the Tresca factor f	174
G.2	Evolution of the friction coefficient μ with (N/kR) for different values of the Tresca factor f	175
G.3	Evolution of the friction coefficient μ with (N/kR) for different values of the Tresca factor f	176
G.4	Evolution of the depth of the deformed layer (h_{max}/R) versus θ for different values of the Tresca factor f	178
G.5	Evolution of the shear strain γ_{xy} versus the depth (h/h_{max}) for $f = 0.3$ and for different angles (N/kR)	180
G.6	Evolution of the shear strain γ_{xy} versus the depth (h/h_{max}) for $f = 0.3$ and for different angles (N/kR)	181
G.7	Evolution of the shear strain γ_{θ} versus the depth (h/h_{max}) for $f = 0.3$ and for different angles (N/kR)	183
G.8	Evolution of the shear strain γ_{θ} versus the depth (h/h_{max}) for $f = 0.3$ and for different angles (N/kR)	184
G.9	Evolution of the maximum shear strain (γ_{xyMAX}) and $(\gamma_{\theta MAX})$ versus the load (N/kR) for $f = 0$	187
G.10	Evolution of the maximum shear strain (γ_{xyMAX}) and $(\gamma_{\theta MAX})$ versus the load (N/kR) for $f = 0.1$	188

G.11 Evolution of the maximum shear strain (γ_{xyMAX}) and ($\gamma_{\theta MAX}$) versus the load (N/kR) for $f = 0.2$	188
G.12 Evolution of the maximum shear strain (γ_{xyMAX}) and ($\gamma_{\theta MAX}$) versus the load (N/kR) for $f = 0.3$	189
H.1 Data for the wedge tests - Aluminium	194
H.2 Data for the wedge tests - Copper	195
J.1 Details of the FEA simulations for the full cylinder	201
J.2 Details of the FEA simulations for the cut cylinder	201
K.1 Data for the full cylinder tests - Aluminium	205
K.2 Data for the cut cylinder tests - Aluminium	207
K.3 Data for the full cylinder tests - Copper	210
K.4 Data for the cut cylinder tests - Copper	211

Nomenclature and abbreviations

Latin symbols

A, B, C, D, E	points defining the slipline field
A_s	$A_s = 1 + \frac{\pi}{2} + 2\epsilon - 2\eta - 2\alpha$
A_o, A	A_o : initial grid area, A : grid area
C, D	material constants for the Coffin-Manson relation
$C.B.N.$	Cubic Boron Nitride
$error(i), error_{local}$	local error at the point $M_{i,i}$
$error_{aver}$	average error
E^*	reduced modulus of the contact
ED	interface
E/σ_y	degree of elasticity
f	Tresca factor or lubrication parameter, $f = \tau/k$
f'	fraction of surface at the interface not covered by boundary film

F	resultant frictional force per unit width
h	given depth in the deformed layer, with $h < h_{max}$
h_{max}	depth of the deformed layer
H, H_v	hardness of the material
i_{max}	$i_{max} = n$, number of α lines
k, k_s	shear flow stress
k, k_{max}	number of a given streamline, with $k_{max} = o$
K	Archard's wear coefficient
L	sliding distance
$m + 1$	number of β lines to describe the fan (EBC)
N	resultant normal force per unit width
N_f	number of cycles to failure
N/kR	load parameter
n	number of points to describe numerically the free surface (ED)
o	number of streamlines
p	hydrostatic stress
p_w	mean pressure on front face of wedge in chapter (1)
p_s	asperity shakedown pressure
P	contact pressure

P_{max}	maximum hertzian pressure
Q_s, Q_i, Q_r, Q_w	flows of solid particles defined in chapter (5)
r	index of a point on a streamline
R_2	radius of the circle defining the free surface
r	ratio of plastic to total work
R	radius of the cylinder
$R.A.$	reduction in area (%) in tensile test
R_c	combined asperity tip radius
S_1, S_2	full cylinder tests, cut cylinder tests
S_{1al}, S_{2al}	tests for aluminium
S_{1co}, S_{2co}	tests for copper
$SBVP1, SBVP2, SBVP3$	stress boundary value problems
$S_i M_j, S_3 M_3$	mechanism of velocity accommodation
$t_{r,k}$	time of $M_{r,k}, r^{\text{th}}$ point on the k^{th} streamline
u	velocity component measured in the α direction
v	velocity component in the β direction
V_x, V_y	velocity component in (x,y)
V, U	rigid material velocity

X, Y	coordinates of the nodal points defining the field
$X_{i,j}, Y_{i,j}, \phi_{i,j}, u_{i,j}$ and $v_{i,j}$	arrays to store the data
w	width of the cylinder
W	normal load
Y	tensile yield strength

Greek symbols

γ_{xy}, γ_r	shear strain, ratchetting strain
γ_α	finite shear strain
α line	first shear line, or direction of maximum shear stress
β line	second shear line
ϕ	anticlockwise angle of the slipline α measured from a fixed reference axis
θ	angle of the interface cylinder/deformed material
$\beta_{calc}(i), \beta, \beta_E$	slope of the velocity vector at the point $M_{i,i}$ of the free surface
$\beta_{tan}(i)$	slope of the vector tangent to the free surface at the point $M_{i,i}$
μ	overall friction coefficient
Δt	time step for the grid
ϵ	$\epsilon = \frac{1}{2} \arccos(f)$
η	$\eta = \arcsin\left[\frac{\sin(\alpha)}{\sqrt{(1-f)}}\right]$

$\Delta\gamma_e$	maximum effective shear strain
τ_0	true shear strength of the material
μ_0	intrinsic μ of boundary film
$\epsilon_a, \epsilon_{xx}$	reversing strain, direct strain
Φ_s	plasticity index
σ	combined rms roughness of the two surfaces
τ, τ_s	shear strength of the interface
α	asperity angle (wedge) or chord angle (cylinder)
$\sigma_x, \sigma_y, \tau_{xy}$	stress components in (x,y)
θ'	angle of the free surface
Δ_y	spacing between the streamlines
Δ_x	spacing between the transverse lines of the distorted grid
$\Delta s_{r,k}$	distance of the segment $M_{r-1,k}M_{r,k}$
$\Delta\gamma_{x,y}$	shear strain increment
σ_y	yield strength
ϵ_f	true strain to fracture
β_c	angle between the leading edge and the center line of the cut cylinder
α_1, α_2	effective attack angle of the cylinder

Φ

angle defined in the
wave model [2]

General introduction

Statistical analysis shows that the main reason for the failure of machines is not breakage but wear of the moving parts resulting from rubbing stress. Although the laws of friction are fairly well substantiated, there are still no satisfactory quantitative laws of wear[13].

When one metal slides across another, frictional energy is generally dissipated both by shearing an interfacial layer, or third body, and by plastic strain in the metal surfaces themselves. It has now become clear from the examination of worn surfaces and of wear particles that the accumulation of this surface strain is linked to the detachment of wear particles. The calculation of mechanical wear rates thus requires a model which can predict the extent and rate of strain due to sliding, and the amount of strain needed to produce wear particles. It must begin with an idealized asperity contact model which is able to calculate the strain imposed on a wearing surface by an asperity sliding across it, and then be combined with a damage rule or damage rules so that the beginning and the rate of debris generation can be found. Finally, a way of characterizing the surface texture must be found in order to extend this single asperity to a real surface.

Over the last few years, quantitative models of wear based on the calculation of plastic strains induced by hard asperities sliding against soft surfaces have been developed. One approach is to assume a rigid-plastic behaviour of the wearing material, neglecting elastic effects and allowing slipline field theory to be used. Combining this with a damage rule, wear rates can be predicted from the strain calculations and the mechanical properties of the

wearing material. Recent investigations have shown that this approach can predict well friction and wear of some non-ferrous metals [14, 15, 16, 6]. The hard asperity is simulated by a rigid wedge, which pushes a wave of plastically deformed material ahead of it. Well-established slipline fields then allow the measured friction and wear coefficients to be related to calculated stresses and strains via a Coffin-Manson low cycle fatigue rule. While the general features of the rigid-plastic model described above are compatible with observations, the representation of the asperity by a simple two dimensional wedge is clearly a limitation. Asperities on real surfaces are three-dimensional and are likely to have their peaks rounded. A more realistic approach is to model the hard asperity with a cylinder; but slipline fields for this type of contact are not so well established.

The general aim of the present investigation is to understand and predict wear for engineering contacts.

The first aim is to develop a new rigid-plastic asperity contact, which models a wave of plastically deformed material pushed ahead of a cylinder. This model must provide friction coefficient and strain pattern associated with the deformation process.

The second aim is to perform scaled-up model asperity experiments, where a hard cylinder slides across the surface of a softer metal and test the predictions of the developed model.

This thesis is composed of eight chapters:

1. In chapter (1), the quantitative models developed over the last few years to calculate how asperity contacts strain a wearing surface and to estimate how this may relate to wear rates are presented. It is shown that there are two distinct system approaches: the first, the elastic-plastic model is the extension of an elastic-plastic model of rolling contact to an asperity contact, which is most appropriate at low strain. The second is a rigid-plastic asperity model which neglects elastic effects. As the

present investigation uses the rigid-plastic approximation, more details are given concerning this approach. Some models of boundary friction to describe the interface, or third body, are also presented.

2. In chapter (2), the basis of slipline field theory and the formulation of the problem of constructing a slipline field are described. The different methods for solving statically indeterminate problems, such as the problem of the present work are presented. A critical analysis of their advantages, drawbacks and limitations leads to the choice of an approach to solve the sliding cylinder problem. It is shown that there is no systematic solution procedure and that a trial and error process has to be carried out.
3. In chapter (3), it is presented in detail how the trial and error process has been successfully applied to determine the slipline field solution for the sliding cylinder problem. The general structure of the solution is described and the conditions imposed by the problem are enumerated. Starting from these conditions, the procedures used to generate the slipline field solution and velocity field solution are described. Finally, the procedures developed to determine the strain pattern undergone by the material going through the plastic region are described.
4. Chapter (4) presents the main results of the developed model: the shape and extent of the plastic region, the overall friction coefficient μ associated with the process and finally the plastic strain cycle undergone by the material during the deformation process predicted. The results are also compared to elasto-plastic finite element analysis.
5. In chapter (5), the two parts of the experimental investigation are described.
 - The first part consists of testing the predictions of our numerical model when a rigid cylinder slides across two non-ferrous metals.

In order to decrease elastic effects, an additional experimental investigation with the use of a cut cylinder has been performed too. Details of the experiments and the equipment involved are given.

- The second part of the experimental work consists of investigating the influence of detached particles accumulated around the contact when a rigid cylinder slides across a soft surface. For the present work, the technique of visualization through a transparent tool, developed in the L.M.C. (Laboratoire de Mécanique des Contacts, I.N.S.A. de Lyon, France) has been used. Details concerning the visualisation technique and the tests performed for the present investigation are also presented.

6. In chapter (6), the friction results are presented and compared to our numerical model for the two tested materials and for the full cylinder configuration and the cut cylinder configuration. Then the results of the visualisation investigation are presented for both materials: the dynamic observations of the particle flows observed at the interface through the transparent tool are correlated to the static observations of the friction track after the test. These results are extrapolated to the tests under investigation. The analysis allows to determine whether the detached particles are trapped inside the contact area and flow at the interface.
7. In chapter (7), we discuss the ability of the new model proposed in this thesis to predict quantitatively friction and strain patterns. Deviations in friction from theory observed in our experimental results are discussed by integrating the relative influence of elastic effects and the presence of third body at the interface. Then, the strain pattern predicted by our numerical model is compared to the results of previous work.
8. Finally, the main conclusions of the present work are recalled and presented in the general context of friction and wear predictions. Perspectives are then proposed.

Chapter 1

Relating surface strains to a wear model

1.1 Introduction

It has long been realized [17] that metallic wear may involve significant plastic strains in the wearing surfaces. Observations of wear tracks and of cross sections normal to the worn surfaces reveal large plastic strains and strain gradients adjacent to the sliding interface [18]. The local microstructure that develops is consistent with work hardening (or work softening in some cases) and with microstructures produced by other methods of achieving large plastic strains. For ductile materials such as copper and silver, the microstructure of the surface layer is very similar to the fine equiaxed cell structure which is generated in high strain torsion-compression or rolling tests [19, 20]. In hardened steels, white-etching microstructures are formed due to the large plastic strains which develop under high hydrostatic stress in both rolling and sliding contacts, which also have an extremely fine cell size [21, 22, 23, 24, 25].

The wear debris produced also has this structure. It is thus logical to suppose that detachment of wear debris is linked to the accumulation of this surface strain [26, 27, 21, 28] and to develop a wear model of debris detachment based on fatigue in the plastic regime.

The calculation of mechanical wear rates thus requires a model which can predict the extent and rate of strain due to sliding, and the amount of strain needed to produce wear particles. It must begin with an idealized asperity contact model which is able to calculate the strain imposed on a wearing surface by an asperity sliding across it, and then be combined with a damage rule or damage rules so that the beginning and the rate of debris generation can be found. Finally, the way of characterizing the surface texture must be found in order to extend this single asperity to a real surface [29].

Over the past few years, quantitative models of wear have been developed, based on the calculation of plastic strains induced by hard asperities sliding against soft surfaces [2, 30, 31, 32, 33, 34]. In all these models, friction energy is assumed to be dissipated both by plastic deformation in the metal surface and by shearing an interfacial layer, or third body. Two distinct approaches have been proposed:

- The first is the extension of an elastic-plastic model of rolling contact to an asperity contact [32, 33, 34], which is most appropriate at low strain.
- The second is a rigid-plastic asperity model which neglects elastic effects [2, 30, 31].

In this chapter, these two different approaches will be described and compared. It will be seen that each model of asperity interaction leads to a distinct way of characterizing surfaces, and has a range of application, which is governed by its underlying assumptions.

Finally, some models of boundary friction to describe the interface, or third body, will be given.

1.2 Elastic-plastic models

1.2.1 The theory of strain in rolling contact

Elasto-plastic models are based on observations made by Crook [35], who showed significant plastic deformation in the rolling direction for pure rolling contacts. Subsequent theoretical studies of the stress-strain cycle in rolling contact, [32, 33], have been performed with loads too small to cause general yield. It was predicted then that a cumulative forward displacement of the surface would be expected from the nature of the stress-strain cycle in rolling contact. In the case where the contact loads are greater than the yield strength, Johnson [33] suggested that the plastic strain can be estimated by assuming that the total strain is the same as in the absence of yield. This led to a reasonable estimation of the shakedown limit (i.e. the load that can be carried purely elastically in the steady state) but the predicted deformations were smaller than in the experiments. Bhargava et al [36] confirmed the previous prediction of the shakedown limit with a more accurate finite element analysis and their predictions of plastic strain cycles were very close to experimental results. A more accurate semi-analytical model, using the movement of edge dislocations to model small plastic strains, was developed by Hearle and Johnson [37]. It gave results that were very close to those of the finite element analysis, which required much more computing time. Since there were still some restrictions to the application of the above theory, it was then developed further to allow for strain hardening [38]. The predictions of strain accumulations in copper and in rail steel loaded just beyond the shakedown limit were accurate.

It should be noted that the strain cycle induced by the rolling/sliding contact of cylinders consists of two components:

1. a fully reversing strain ϵ_a ,
2. an accumulating, also called ratchetting strain γ_r .

A typical strain cycle induced by a rolling and sliding roller is shown in figure (1.1). Rolling contact fatigue lives could be related to an accumulation over many cycles of γ_r to a critical value, or they could be related to the closed part of the strain cycle ϵ_a [33].

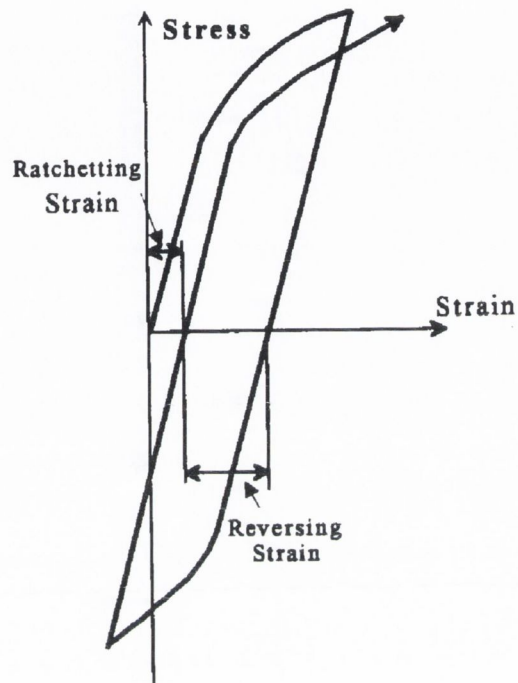


Figure 1.1: Strain cycle induced by a rolling and sliding roller: ϵ_a = reversing strain; γ_r ratchetting strain

1.2.2 Extension to sliding wear calculations

All the previous studies were focused on the understanding of rolling contacts. However, as sliding wear is controlled also by plastic strain, this gave the idea to several authors to apply this theory to sliding contacts.

As a starting point, Crook's observations [35] of forward flow in the surface of rolling discs were correlated to the observations made by Akagaki and Kato [39, 40] regarding the extrusion of thin silvers from the crest of the asperities on a hard steel surface using a pin-on-disc configuration. The flakes break off to form wear particles when sufficient material has been extruded.

These experiments suggested that the extrusion phenomenon, also called film wear could be modelled, using the techniques developed for rolling contact, as a progressive accumulation of ratchetting strain γ_r at the tip of the asperities.

This prompted Kapoor et al [41, 42] to devise an experiment, where they loaded sector-shaped copper pads against steel rings which were machined to different finishes. The test results turned out to be very similar to the work of Akagaki and Kato [39, 40]: when the load was increased above a critical value, the copper experienced continuous incremental deformation which gradually extruded sideways causing nominal contact pressure to fall to a value at which the extrusion ceased. This final shakedown pressure was strongly dependent on the surface finish. In order to model these results and correlate these experiments, Kapoor et al [41, 42] used spherical tipped asperities as an idealised surface texture to model the surface since the equations describing the rolling elastic contact were initially applied to curved surfaces. Following the work of Greenwood [43] and of Whitehouse [44], a plasticity index was defined as:

$$\Phi_s = \frac{E^*}{p_s} \left(\frac{\sigma}{R_c} \right)^{\frac{1}{2}} \quad (1.1)$$

where the plasticity index, ϕ_s is a function of the asperity shakedown pressure p_s , the reduced modulus of the contact E^* , the combined rms roughness

of the two surfaces σ , and the combined asperity tip radius R_c .

An important point, resulting from equation (1.1), is that the shakedown pressure can be related to surface characteristics and the loading conditions. But principally, this plasticity index describes the transition from elastic to plastic contacts. When the nominal pressure of the contact is below the shakedown limit, the system remains in a steady state and will carry the load purely elastically and give a very low wear rate. Above this limit, the steady state will not be elastic and the cumulative incremental plastic flow will be encountered. Wear by extrusion can occur and could in principle be predicted by calculating the ratchetting strain at the asperity tips.

Kapoor and Johnson [34] presented an analysis of the asperity contact in which lamellar debris is generated by the process of plastic ratchetting, under the repeated pummeling by the asperities of a harder mating surface. They showed how wear could be predicted using the above theory.

This approach to the strain induced by sliding predicts many phenomena very well and in principle the model enables an absolute value of the wear rate to be calculated. However, so far, the difficulty of defining the plasticity index of a surface with sufficient precision, [44], limits the value of this theory as a tool for the quantitative prediction of wear rates for real contacts.

1.3 Rigid-plastic models

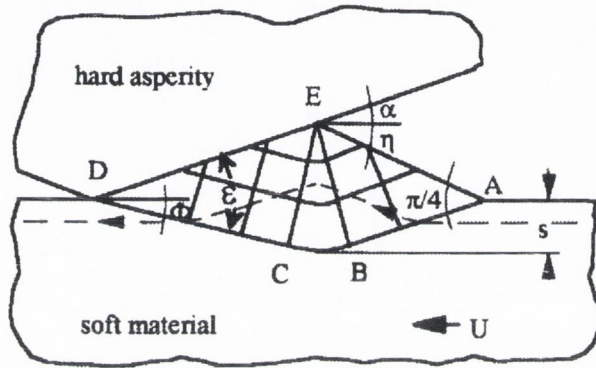
1.3.1 Friction calculation

Another approach to the calculation of strains in asperity contact is to neglect elastic effects entirely. Assuming plane strain and ideal plasticity, the stresses and strains in a contact between a hard asperity and a soft surface can be calculated by a slip-line field.

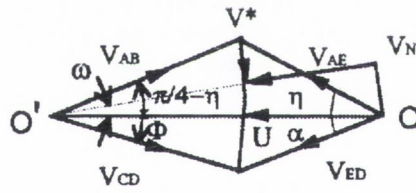
Challen and Oxley [2] introduced a slipline field model of asperity deformation to describe the interaction between a hard asperity and a soft surface,

which is similar to the slipline fields proposed by Green [45] for a weak junction. As shown in figure (1.2), the hard asperity is idealised as a rigid wedge, which pushes a wave of plastically deformed material ahead of it as it slides across the softer surface. This steady state slipline field corresponds to the situation when the shear strength of the interface τ is less than the shear strength of the metal k and is more adapted to mild wear calculation. For more severe wear conditions, a wear model (wave removal model) and a cutting model (or chip formation model) were proposed to model abrasive wear and seizure respectively [2].

In the construction of the slipline field (see figure(1.2)), the independent variables are the asperity angle α , and the normalised strength, (f) of the interfacial film along ED . Therefore, friction in this model may be taken as being related to a single surface parameter α and a lubrication parameter, f , and thus combines the adhesion and ploughing mechanisms which have been studied independently in previous theories [46], and allows interaction between them.



(A) SLIP-LINE FIELD



(B) HODOGRAPH

Figure 1.2: Slipline field proposed by Challen and Oxley [2] for the sliding wedge problem

All the details concerning the calculation of the angles of the slipline field and the stresses are given in appendix (A). Calculation of the stresses on the hard asperity allows the normal load N , and frictional load F , per unit width, and hence the friction coefficient, to be determined as follows,

$$\mu = \frac{F}{N} = \frac{(A_s \cdot \cos(\alpha) + \sin(2\epsilon - \alpha)) \cdot ED \cdot k_s}{(A_s \cdot \cos(\alpha) + \sin(2\epsilon - \alpha)) \cdot ED \cdot k_s} \quad (1.2)$$

where:

$$A_s = 1 + \frac{\pi}{2} + 2\epsilon - 2 \arcsin[\sin \alpha / \sqrt{(1 - f)}] - 2\alpha,$$

$$2\epsilon = \arccos f,$$

$$f = \frac{\tau_s}{k_s},$$

k_s is the shear strength of the soft material,

τ_s is the shear strength of the interface.

Results calculated from equation (1.2) showing the influence of the roughness parameter α and the interfacial film strength parameter f are in agreement with the trends usually observed in experiments, that μ is predicted to increase with an increase in α and f .

Other researchers have also investigated the wave model. Petryk [47] suggested an alternative slipline field to represent wave formation but found that the model of figure (1.2) is the most acceptable because for a given set of conditions it gives the smallest frictional force. Avitzur et al [48] have covered much the same ground as Challen and Oxley but have used the upper bound method in preference to the slipline field method. At about the same time as that of Challen and Oxley, Johnson [49] investigated the transitional period from initial indentation to the wedge reaching the surface. He did this by constructing a series of slipline fields representing the progression of the deformation.

Experiments have been performed by several authors [50, 51, 6] to check the wave model and to determine the accuracy of equation (1.2). They made scaled-up model asperity experiments, in which a hard wedge was indented

into the surface of a softer material and then slid along it with the normal load held constant. The results obtained showed that equation (1.2) gives accurate predictions of μ for a wide range of α and f values. The above experiments showed also that a wave can be formed by plastic deformation without fracture being involved. An example of the plastic wave is given in figure (1.3).

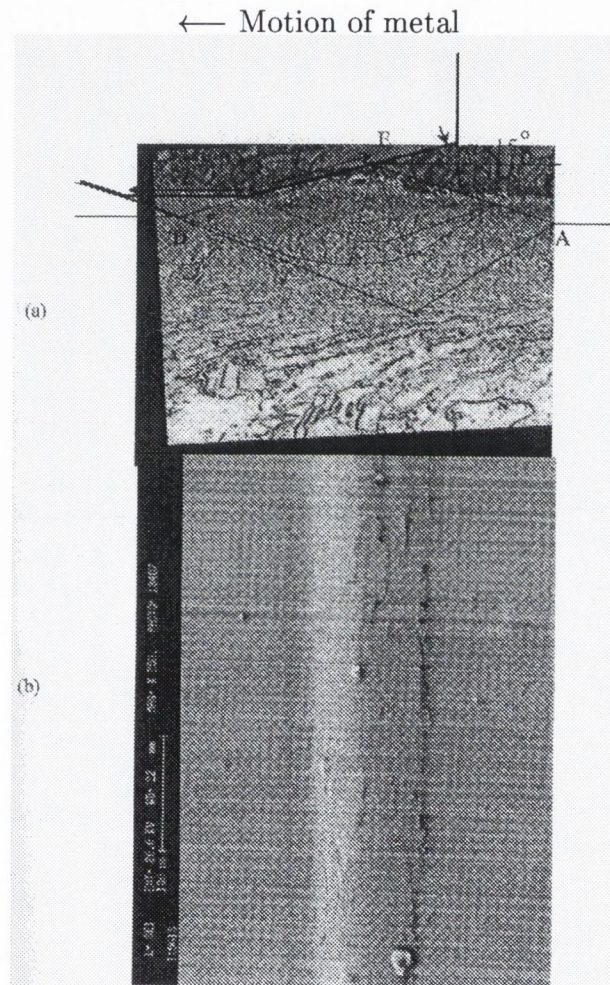


Figure 1.3: Two views of the plastic wave after wedge shape experiments on copper: (a) A section parallel to wear track and (b) normal to the worn surface. Taken from [6]

In considering real asperities as opposed to scaled-up model-asperities, Moalic et al [52] have shown that equation (1.2) predicts μ accurately for actual surfaces as long as α is measured from those regions of the asperities actually in contact during sliding.

Pointing out that the representation of the asperity by the single wedge-shape is unrealistic, Challen and Oxley [1] proposed the chord approximation model, as shown in figure (1.4). In this model, the asperity is idealised as a rigid cylinder. If the area of contact between the asperity and the deformed material is approximated by its chord, the slipline field and associated hodograph previously established by Challen and Oxley [2] for wedge-shaped asperities can be used. The main difference is that for a cylindrical asperity of radius R , the asperity angle α and the length of the interface ED are now interrelated and depend on the geometrical and loading conditions.

Petryk [47] also developed a slipline field model that he proposed for the sliding of a rigid wedge-shaped asperity over a flat ductile surface, to account for an asperity with a rounded wedge tip. The proposed slipline field was associated with a severe type of deformation process, which was adhesion of the deformed material to the wedge combined with localized large plastic strains.

More recently, Bressan et al [53] developed the chord approximation model of Challen and Oxley [1], in order to account for an interface which exhibits a shear strength which is a known function of the local pressure, a fact not taken into account with the Tresca factor f . The authors compared their numerical results with friction coefficients obtained for constant values of f , as assumed in the chord model [1]. In some cases, they observed noticeable deviations in friction from the chord model.

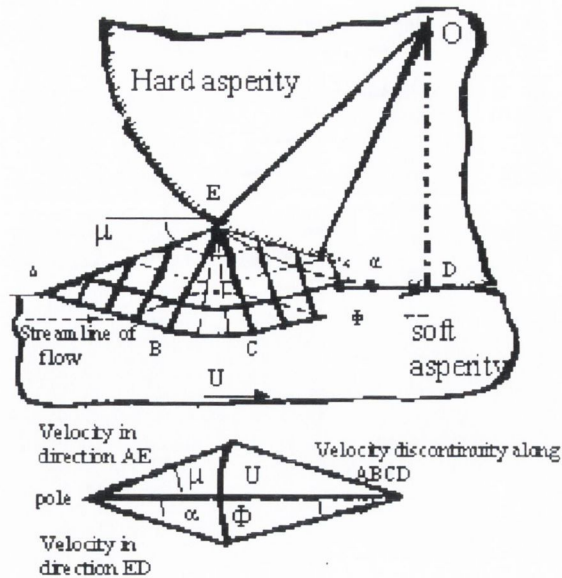


Figure 1.4: Chord approximation model developed by Challen and Oxley [1]

1.3.2 Strain calculation

An interesting feature of the wave model is that material that passes through the wave is retarded relative to the rest of the material and the surface is plastically worked, which is a common observation in practice. Challen et al [30] have shown how with each wave pass the maximum effective shear strain $\Delta\gamma_e$ induced in the surface can be calculated from a simplified wave model, where the centred fan has been replaced by a velocity discontinuity. More accurate analyses of the strain cycle have been proposed by Kapoor [54] and Yang and Torrance [15]. The latter authors have described how the direct, or cyclic strain ϵ_a and ratchetting strain γ_r , involved in wave formation can be calculated and given equations for this purpose. An example of the cyclic and ratchetting strain cycle experienced as material passes through the wave is given in figure (1.5). As in rolling and sliding contact, it consists of two parts:

1. a direct, or cyclic strain cycle ϵ_a , which fully reverses,
2. a shear, or ratchetting strain cycle γ_r , which accumulates.

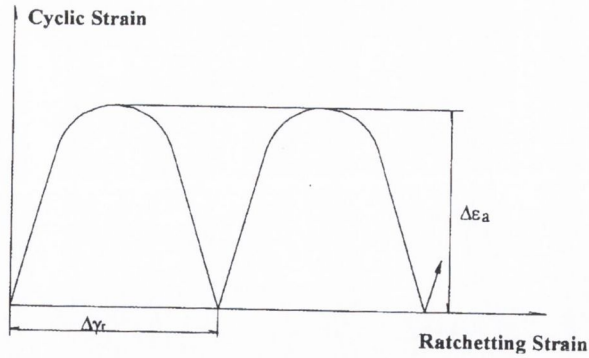


Figure 1.5: Typical plastic strain cycle induced by a sliding asperity.

Experiments have been performed by several authors [55, 7, 6], where the plastic strains left by model wedge shaped asperities were measured by visio-plastic methods as shown in figure (1.6). The specimen observed presents a highly strained layer near the surface and the strains gradually decrease to zero at the boundary of the deformed layer. This last feature is not consistent with the strain pattern predicted by the wave model, which states a homogeneously deformed layer left at the exit of the wave. So far, strain-hardening [55, 7] and elastic effects [56, 57] have been the main effects investigated to explain these last observations for wedge shaped asperities. However, it has been observed in Yang's experiments that the tip of the wedge used rapidly became rounded, so that it could be better described as cylindrical. Nevertheless, the chord model [1] is based on the wave model and thus cannot predict the experimental observations.

Torrance [29] performed finite element analysis for the sliding wedge problem. As predicted by slipline field theory, he found that there is a highly strained layer at the surface. However, although the general level of strain in the layer is close to that predicted by the wave model [2], it is not uniform with depth, and instead rises to a maximum beneath the surface, which confirms the experiments of Kopalinsky [55, 7].

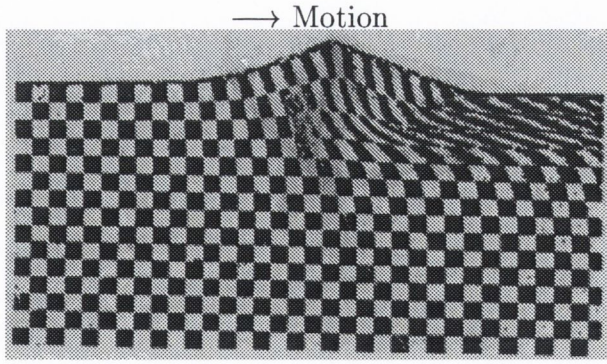


Figure 1.6: Experimental deformed grid after wedge experiments taken from [7]

1.3.3 Mild wear calculations

On the assumption that wave formation is fully plastic and the process of debris detachment is one of low cycle fatigue, the passage of the hard asperity leaves a plastically strained layer. After a critical number of strain cycles (N_f) this layer will be detached as wear particles. To determine N_f , a relationship must be found which relates it to the strain cycle and the material properties.

As a starting point, Challen et al [30] suggested that it would be related to the maximum effective shear strain increment $\Delta\gamma_e$ in each pass, by a Coffin-Manson low cycle fatigue relation:

$$N_f = \left(\frac{C}{\Delta\gamma_e}\right)^D \quad (1.3)$$

where C and D are material constants which must be found experimentally.

Equating the plastic work needed to generate a wear particle calculated from equation (1.3), and the total plastic work determined from the frictional force, Challen et al [30] established an expression for the wear volume V occurring in a sliding distance L as follows:

$$V = \frac{9 \cdot \sqrt{3} \cdot r \cdot \mu \cdot N \cdot L}{C^D \cdot \Delta\gamma_e^{1-D} \cdot 3 \cdot H} \quad (1.4)$$

where r , ratio of plastic to total work, μ , and $\Delta\gamma_e$ can all be determined from the wave model in terms of α and f [30, 6]. N is the normal load per unit width acting on the surface and H is the hardness of the wearing material. The Archard's wear coefficient K is then equivalent to :

$$K = \left(\frac{9 \cdot \sqrt{3} \cdot r \cdot \mu}{C^D \Delta\gamma_e^{1-D}} \right) \quad (1.5)$$

Experimental wear results [58] have been shown to be in reasonable agreement with the predictions of equation (1.5) by Challen et al [59] by choosing appropriate values of C and D . However, in order to use this theory in a predictive manner, the constant C and D must be determined independently. Yang and Torrance [15, 16] devised the wedge wear test for this purpose.

An alternative approach has been suggested by Kapoor [54], who proposed two competing failure mechanisms: low-cycle fatigue with the equation:

$$N_f = \left(\frac{C}{\epsilon_a} \right)^2 \quad (1.6)$$

and ratchetting, with the equation

$$N_f = \left(\frac{2C}{\gamma_r} \right) \quad (1.7)$$

Kapoor argued that, although the reversing strain cycle will produce low cycle fatigue, in most cases, the failure mechanism would be ratchetting as the ratchetting strain would be much larger than the reversing one. These competing mechanisms have been investigated by several authors [14, 15, 16, 6], who performed wear tests on non-ferrous metals. The authors showed that, for aluminium and brass experiments, although ratchetting was involved in wear, the dominant damage mechanism seems to be best described by low-cycle fatigue. However, as pointed out by Torrance [29], when the strain per asperity contacts is very low, ratchetting wear will certainly occur and will

be better analysed by elasto-plastic models [41, 42]. However, to date, the discussions on the roles of these mechanisms in determining failure in the wear process have been inconclusive.

1.3.4 Limits of rigid-plastic models

The rigid-plastic model is best suited to situations where the strains are high. It is easy to apply to real surfaces as the friction coefficient is related to only one surface roughness parameter, compared to the elasto-plastic model which requires two parameters. Furthermore, work has already been carried out on defining an unequivocal method of measuring surface slopes [52, 60, 61] and has been verified for real surfaces and shown to predict friction well for simple boundary lubricated contacts, [52, 62, 60]. It has also been used successfully in predicting wear [31, 29].

However, the disadvantage of a rigid plastic model is that one surface has to be deformed plastically, which will not be the case at low asperity slope. In that case, the elastic contribution to deformation becomes significant and the simplifications inherent in any slipline field model are less realistic.

Torrance [29] has shown by using finite element analysis, that plastic models break down at low asperity slopes as the plastic strains become equal to or smaller than the elastic strains. Torrance et al [8, 63, 64] developed a simple method for calculating the pressure on elasto-plastic asperities, and verified this by finite element analysis. The main contribution of this work has been to extend the existing wave model [2] to smoother surfaces with lower slopes. The authors have shown that when the asperity angle α falls below a critical value, the normal and tangential stresses begin to deviate significantly from those given by slipline field theory. This is shown in figure (1.7), where the average pressures predicted by this model as a function of α are compared to results obtained from finite element analysis and slipline field theory. The effect this has on friction depends on the nature of the boundary film, or third body, separating the surfaces and on its mechanical properties. Basically, higher

friction coefficients are expected for low asperity angles when the boundary film has a constant shear strength.

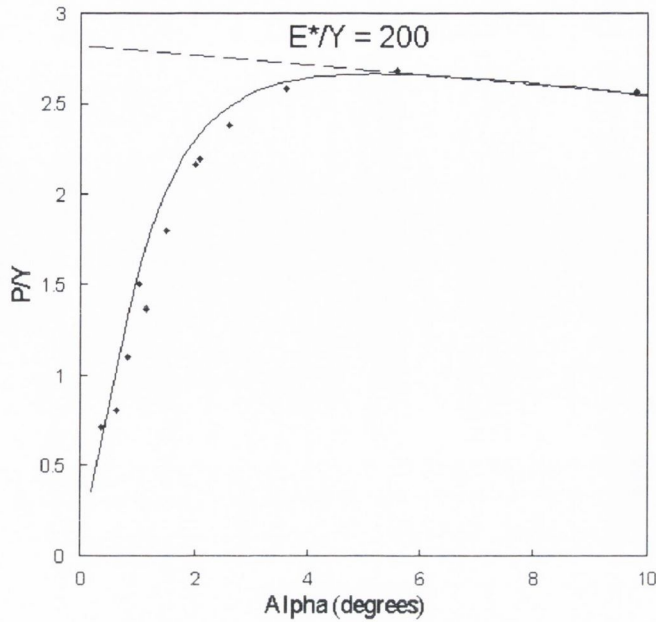


Figure 1.7: Mean pressure p_w on front face of wedge versus α for $E^*/Y = 200$ (The solid line is from the analytical model of Torrance et al [8], the dotted line is from slipline field theory [2] and the points are from finite element analysis [8]).

Bressan et al [53] investigated the effect of elastic distortions when using asperities with cylindrical profiles by finite element analysis in the elasto-plastic range. The authors showed that when the deforming material is less than fully rigid, a portion of the imposed deformation can be accommodated elastically. For materials with strength to modulus ratios characteristic of most engineering materials, this effect is not insignificant, leading to lower friction coefficients than those predicted by the chord model [1] when no friction is considered at the interface (i.e. $f=0$).

1.4 Boundary friction with fatty acids

In this work, stearic acid was chosen as the boundary lubricant for all the experiments, as its properties are well known, and it has been used in many previous studies [65, 66].

1.4.1 Stearic acid as a boundary lubricant

In asperity models, such as those presented in section (1.3), it is assumed that the film formed at the interface between the asperity and the deformed material, will be exceedingly thin so that boundary rather than hydrodynamic lubrication occur. Under these conditions, the load is carried largely by asperity deformation, but thin films or contaminants are present in the load bearing areas [67].

Boundary lubrication describes the process by which friction and wear between surfaces in relative motion are reduced by boundary films when fluid film formation is not possible [68]. Commercially available lubricating oils nearly always contain small quantities of chemical compounds, known as boundary additives, which enhance the boundary lubricating properties of the oil by forming protective thin films. The boundary additives, such as fatty acids (like stearic acid), are either adsorbed (physisorption), or chemically attached to the metal surface (chemical reaction). Effective lubrication will depend on the adsorption of the fatty acid and on its reactivity with the metal substrate to form a metallic soap [65].

1.4.2 Boundary friction

Various theories and models have been developed to explain the forces generated between two moving surfaces under conditions of boundary friction, such as the interfacial shear strength ratio, or Tresca factor f , used in Bowden and Tabor's theory [65, 46]. This is defined as the ratio of the shear strength of the boundary lubricated interface, τ , to the shear yield stress of the deforming

material, k_s , which is assumed to be constant [2],

$$f = \frac{\tau}{k_s} \quad (1.8)$$

where $0 < f < 1$.

The normalised interfacial film strength, f , is therefore a unique property of the lubricant and the material tested. Challen et al [50] estimated the shear strength of the interfacial film in the case of the wave model [2], as shown in figure (1.8) by resolving the forces along the wedge/wave interface as follows,

$$\tau = (F \cdot \cos \alpha - N \cdot \sin \alpha) / ED \quad (1.9)$$

where,

F is the frictional force per unit width,

N is the normal load per unit width,

α is the asperity angle,

ED is the length of the interface.

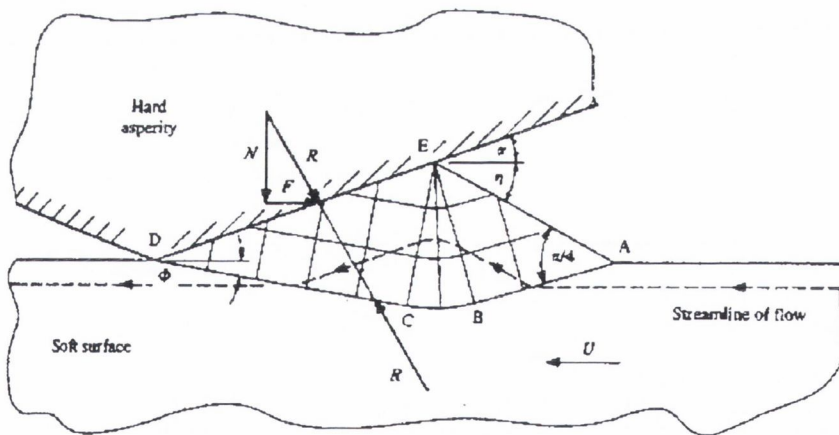


Figure 1.8: Slipline field proposed by Challen and Oxley [2] for the sliding wedge problem

Bowden and Tabor [65, 46] considered that the shear strength of the interface arose from defects in the boundary film covering the contacting surfaces, leading to local micro-welds at the gaps in the film. The value of f was taken to be the fraction of the contact not covered by the boundary film. This implies that the shear strength of the boundary film itself can be ignored.

However, it has become clear that the mechanical properties of fatty acids and soaps are invariably sensitive to the locally generated pressures, a fact not taken into account with the interfacial shear strength ratio f . Briscoe et al [66] showed that boundary films had measurable shear strengths, which could be represented at constant temperature as:

$$\tau = \tau_0 + \mu_0 P \tag{1.10}$$

where,

τ_0 is the true shear strength of the material,

μ_0 is a constant,

P is the contact pressure.

For lubricating fluids at the typical asperity contact pressures found in metals, the second term of equation (1.10) generally dominates so that the shear stress is approximately proportional to the pressure [67]. In such cases Black et al [69] showed that an expression for the friction coefficient could be derived without reference to asperity deformation. This expression allows the interfacial film strength to be specified as follows:

$$\mu = \tan(\alpha + \arctan(\mu_0)) \tag{1.11}$$

One disadvantage is immediately obvious with Black's model: the effect of the material properties are not taken into account. This would suggest that different materials with the same average asperity slope and lubricated with the same oil and under the same conditions, will have the same friction coefficient.

However, in the more general case, the shear strength of the boundary lubricated interface may be a more complex function than the linear expression of equation (1.10). The true shear strength of the material τ_0 in equation (1.10) may be significant, or the interface may not be completely covered by an organic layer, as Bowden and Tabor suggested. If both occur, then the interfacial shear strength of the fraction of the rubbing surface not covered by boundary film will be due to the softer material's shear strength, k_s , while the rest will be due to the shear strength of the boundary film, τ_s [8]. Equation (1.10) thus becomes:

$$\tau = (\mu_0 P + \tau_0)(1 - f') + k_s f' \quad (1.12)$$

where f' is the fraction of surface not covered by the boundary film.

The interfacial shear strength may now be found as follows,

$$f = \frac{(1 - f')P\mu_0}{k_s} + f' \quad (1.13)$$

There is also the possibility that debris or oxide may be trapped in the interface and mix with the organic layer to form a paste.

1.4.3 Limits of boundary lubrication models

As pointed out by Johnson [67], the strength properties of such oxide films are of great practical importance and much less understood. If the oxide takes the form of compacted powder, or a paste mixed with water or grease, such as found on the running surface of railway rails [70], classical boundary lubrication theory may not hold anymore. Beagley [70] investigated the rheological properties of track contaminants often observed at the wheel/rail interface, the resulting films being formed from autumn leaves or flange lubricator grease combined with solid rail debris. It was shown that the boundary lubrication model, which uses a proportional relationship between shear stress

and pressure holds when the rail is free from solid debris. However, when surface interactions are significantly hindered by the presence of trapped debris, some other rheological models must be invoked. The mechanical behaviour of the interface will depend on the amount of contamination, its viscosity and shear strength, on the train speed, and the size and shape of the contacts formed between wheel and rail [70]. The paste at the interface may have both “solid” and “viscous” properties.

While there is some information available on the relevant properties of solid layers when they are formed or applied as boundary or solid lubricants, the mechanical and rheological properties of layers of compacted debris, although they have been observed in practice, have very much less often been studied in detail [13].

In recent years, much progress has been made in the understanding of friction in particular with the introduction of the third body concept [71, 12, 72, 9]. Recent experimental studies [73, 10, 74] with solid lubricant have been associated with theoretical studies, such as the development of granular flow models [75, 76, 77]. These studies constitute a first step in the construction of a rheological model for the solid third body [78].

Chapter 2

Analysis of the methods for constructing a slipline field

2.1 The slipline field theory

In this section, the main points of the slipline field theory are recalled. Further details regarding this theory have been extensively described by several authors [4], [79], [5].

The main assumptions under which the theory applies can be stated as follows:

1. the material is isotropic and homogeneous.
2. the material is rigid-perfectly plastic. This implies firstly that the elastic components of strain are neglected. There is thus no change in the volume of the plastic material during deformation. Secondly the shear flow stress of the material k is constant (no work-hardening).
3. the deformations occur under plane strain conditions.
4. the possible effect of temperature, strain-rate and time are not considered.

The basic theory of plane plastic flow provides the following set of equations involving stress, strain and the yield criterion to describe the behaviour of material in the plastic region:

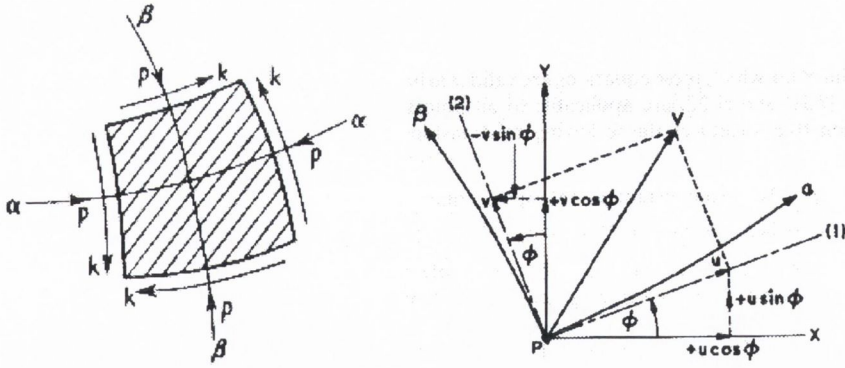
$$\left. \begin{aligned} \frac{1}{4}(\sigma_x - \sigma_y)^2 + \tau_{xy}^2 &= k^2 \\ \frac{\partial \sigma_x}{\partial x} + \frac{\partial \tau_{xy}}{\partial y} &= 0 \\ \frac{\partial \tau_{xy}}{\partial x} + \frac{\partial \sigma_y}{\partial y} &= 0 \end{aligned} \right\} \quad (2.1)$$

$$\left. \begin{aligned} \frac{\partial V_x}{\partial x} + \frac{\partial V_y}{\partial y} &= 0 \\ \frac{2\tau_{xy}}{\sigma_x - \sigma_y} &= \frac{\partial V_x/\partial y + \partial V_y/\partial x}{\partial V_x/\partial x - \partial V_y/\partial y} \end{aligned} \right\} \quad (2.2)$$

where σ_x, σ_y and τ_{xy} are the stress components and V_x and V_y are the velocity components with reference to a Cartesian system of coordinates (x, y) .

Under plane-strain conditions, the two orthogonal families of curves whose directions at every point coincide with those of the maximum shear stress or shear strain rate are known as the sliplines α and β . A slipline field consists of a network of these sets of curves which are drawn to indicate the directions α and β at any point in the plastic region. A slipline field is usually associated with a hodograph, which is a graphical representation of the velocity at each point of the plastic zone. Referred to these sliplines, the state of stress at any point of the plastic region consists of a superposition of a hydrostatic stress, p , on a pure shear stress k , as illustrated in figure (2.1a).

In the slipline field theory, equations (2.1) and (2.2) are transformed to a slipline coordinate system (α, β) to simplify the formulation of the problem. This transformation leads to the derivation of one equivalent set of four equations involving four unknowns. Firstly, the Hencky stress equations equivalent to the stress equilibrium equations (2.1) can be written in their finite difference form, which is the form used in this thesis, as follows:



a: Stresses. Taken from [4] b: Velocities. Taken from [79]

Figure 2.1: State of stress and velocity in the α and β slipline directions

$$\left. \begin{aligned} \Delta p + 2k \Delta \phi &= 0, \quad \text{along an } \alpha \text{ line,} \\ \Delta p - 2k \Delta \phi &= 0, \quad \text{along a } \beta \text{ line.} \end{aligned} \right\} \quad (2.3)$$

where p is the hydrostatic (compressive) stress which acts normal to the sliplines, k is the shear flow stress of the material (assumed constant) and ϕ is the anticlockwise angle of the slipline α measured from a fixed reference axis.

Secondly, the Geiringer velocity equations, equivalent to the velocity compatibility equations (2.2) are written in their finite difference form as:

$$\left. \begin{aligned} \Delta u - v \Delta \phi &= 0, \quad \text{along an } \alpha \text{ line,} \\ \Delta v + u \Delta \phi &= 0, \quad \text{along a } \beta \text{ line.} \end{aligned} \right\} \quad (2.4)$$

where u and v are the velocity components measured in the α and β direction respectively, as shown in figure (2.1b).

Solving a slipline field problem consists of determining the four sets of unknowns p, ϕ, u and v , using the system of four equations (2.3) and (2.4) and the available boundary conditions. The two unknowns p and ϕ are sufficient to completely specify the geometry of the slipline field and the stress conditions. Thus for a given problem, if there are enough stress boundary conditions, the plastic region and the state of stress can be determined without considering

the velocities using the Hencky stress equations (2.3). The velocities u and v can be determined afterwards using the Geiringer velocity equations (2.4). Such a problem is statically determinate.

However, in many plasticity problems the stress boundary conditions are not sufficient to define a unique slipline field and this is usually compensated for by using more velocity conditions. In that case, the Hencky stress equations (2.3) and the Geiringer velocity equations (2.4) have to be solved together using both the stress and velocity boundary conditions. Such a problem is statically indeterminate. The methods for computing a slipline field solution when the boundary conditions are of this mixed nature are presented in section (2.2).

A complete solution consists of a statically admissible stress field (which satisfies the Hencky stress equations and the stress boundary conditions) and a velocity field kinematically admissible relative to the stress field. However, for complete acceptance, a slipline field should be checked to see that the rate of plastic work is always positive and that the stresses in the surrounding non-deformed material are below the yield point. The methods available to check both conditions are presented in section (2.4).

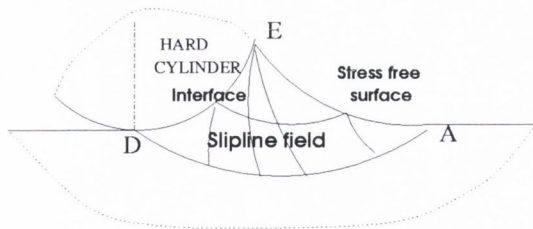
A network of sliplines possesses several geometrical properties which are very useful in finding a slipline field solution. The main geometrical property, given by Hencky's first theorem and used in the present work is recalled in appendix (C).

2.2 Methods available for constructing a slipline field: Choice of an approach for the present problem

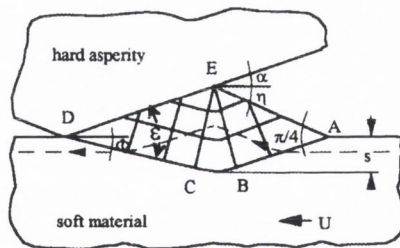
2.2.1 Introduction

The slipline field theory has been developed extensively over the last 50 years and has been successfully used to analyse the deformation and stress fields in many plane strain metal forming processes [4], [5], [80], [79]. However there are still difficulties in computing slipline field solutions, especially for statically indeterminate problems and so far, no systematic procedure suitable for all types of problem has been provided.

The problem of the present work is statically indeterminate. Indeed none of the sliplines have a pre-defined or known shape, nor is the stress free surface shape known as shown in figure (2.2a). This difficulty can be partially overcome by examining the existing solution of the wave model developed by Challen and Oxley [2] (see figure (2.2b)). This well established slipline field solution, which only differs from the present problem in the interface geometry, can provide some guidance in the construction of the possible field. One might expect that the field of the present work will be of a similar shape. However, the wave model presents a straight interface, a straight free surface and the sliplines are straight or circular in the fan. Regarding the curved interface of our problem, one can expect a curved free surface and some curvature in the slipline network. This prevents us proposing a new slipline field using an intuitive procedure, which is usually successful when the new slipline field is expected to have a simple geometry, as when both families of sliplines are straight or when there is a centred fan zone as in Challen and Oxley's field [2].



a: sketch of the possible solution



b: wave model taken from [2]

Figure 2.2: Slipline field proposed by Challen and Oxley [2] for the sliding wedge problem and sketch of a possible solution for the sliding cylinder problem

2.2.2 The trial and error process

For this type of problem where neither the shape of the sliplines nor their hodograph images can be deduced in advance, no specific method exists in the literature; a trial and error process has to be used. This has been schematicized in figure (2.3).

This usually consists of assuming an initial slipline shape. This provides the missing stress boundary conditions. The complete slipline field can then be constructed. The velocity field is then computed using those velocity boundary conditions that are necessary for the purpose. The solution is then tested to see if the remaining velocity boundary conditions are satisfied and if not, the assumptions made to generate the slipline field are modified and the procedure repeated until the agreement is satisfactory. The problem is to find a suitable way of correcting the assumptions made in order to have the problem converge to the solution. A geometrical convergence criterion has thus to be determined.

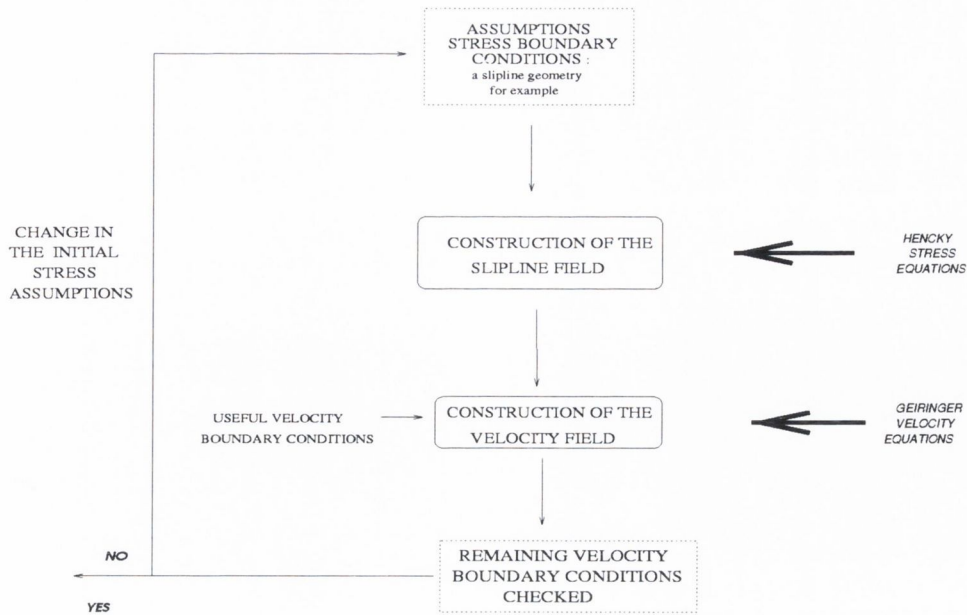


Figure 2.3: Trial and error process

2.2.3 Methods available to assist with the trial and error process

To assist in this trial and error process, three main methods have been developed:

1. Graphical methods: these methods of constructing approximate solutions are based on Prager's graphical procedure for constructing the slipline field network together with a trial and error procedure for finding the shape of the initial slipline [81]. This technique has been applied successfully to many problems [82, 83, 84]. However, as pointed out by Dewhurst and Collins [85], this method does suffer from the obvious shortcoming of requiring a prohibitive amount of time to obtain the solution for a single geometry. Indeed, this method requires significant drafting efforts and seems quite heavy to set up.
2. Numerical methods: These methods of constructing a slipline field are based on the finite difference formulation of the Hencky Stress equations

(2.3) and the Geiringer velocity equations (2.4) and also the geometrical properties of any slipline field. From an assumed slipline, slipline fields are constructed step by step using the detailed procedures given by Hill [4] for the numerical determination of slipline fields and velocity fields for different boundary value problems. Many authors have used these methods [86, 87]. An example of such an approach has been given by Shimmin and Oxley [87] for the problem of plane strain drawing through circular dies. These authors suggested numerical techniques based on Hill's work and adapted to the construction of the slipline field of their problem. An initial slipline was assumed. The slipline field and velocity field were constructed numerically. They then developed optimization techniques, based on a geometrical criterion to successively change the assumed slipline shape so that the resulting hodographs finally converge.

3. Matrix operation method: This method has been proposed by Collins [88] and developed later by Dewhurst and Collins [85]. The developed formulation reduces the problem to one in linear algebra and the problem of finding the initial slipline reduces to a simple matrix inversion. This provides a systematic computational procedure which greatly facilitates the solution of statically indeterminate problems, which are too complex to treat by trial and error procedures either numerically or graphically. This has been used successfully by Petryk [89] for the sliding of a wedge-shaped asperity. This third method is tempting but unfortunately the use of the matrix operator is limited to problems with boundary conditions which lead to linear integral equations. A boundary condition such as the curved boundary present in our problem will result in a non-linear integral equation which cannot be handled by this method.

2.2.4 Conclusion: choice of a method

In this section it has been shown that the statically indeterminate problem of the present work must be solved by a trial and error process. Three main methods have been described which aid the trial and error process. As the problem of the present work cannot be handled by the Matrix operation method, the trial and error process has thus to be solved either graphically or numerically. It was decided to use a numerical method to generate the fields in the same way as Shimmin [87]. It was believed that this would not only decrease the hours of drafting efforts required in graphical methods but would also make modifications easier and make the method more accurate. The basis of this approach is presented in the next section.

2.3 The numerical calculation of slipline field

As previously mentioned, Hill [4] proposed procedures for the numerical determination of the nodal points of a slipline field for different situations encountered in plasticity problems, called the stress boundary value problems. These procedures are based on the Hencky equations and also on the consequent geometrical properties of a slipline field. In this section one of the three stress boundary value problems which repeatedly occurs in the present work is briefly described. It will be called the first stress boundary value problem (or SBVP1). This shows how any slipline field, once all the stress boundary conditions have been assumed, can be constructed and the associated numerical techniques used to generate it are outlined. The description of the other two stress boundary problems (SBVP2 and SBVP3) identified in the present problem can be found in appendix (C).

Hill [4] also proposed procedures for different velocity boundary value problems. The velocity boundary value problem, analogous to the stress boundary value problem of this section is also described here. It will be called the first velocity boundary value problem. The other velocity boundary value problems

encountered in the present problem can be found in appendix (C).

Consider a section of a curvilinear slipline field bounded by the two known sliplines $O_t A_t$ and $O_t B_t$ as shown in figure (2.4). The two sliplines $O_t A_t$ and $O_t B_t$ can be subdivided into an arbitrary number of small arcs n and m respectively. If the elemental section $(O_t, M_{1,0}, M_{0,1}, M_{1,1})$ is considered, the slope $\phi_{1,1}$ associated with the nodal point $M_{1,1}$ of this network as well as its coordinates $x_{1,1}, y_{1,1}$ and its hydrostatic pressure $p_{1,1}$ can be determined from the points $O_t, M_{1,0}$ and $M_{0,1}$ by the following relationships :

$$\left. \begin{aligned} \phi_{1,1} &= \phi_{1,0} + \phi_{0,1} - \phi_{0,0}, \\ p_{1,1} &= p_{1,0} + p_{0,1} - p_{0,0} \\ y_{1,1} - y_{0,1} &= \left(\tan\left(\frac{\phi_{1,1} + \phi_{0,1}}{2}\right) \right) (x_{1,1} - x_{0,1}) \\ y_{1,1} - y_{0,1} &= -\left(\cot\left(\frac{\phi_{1,1} + \phi_{1,0}}{2}\right) \right) (x_{1,1} - x_{1,0}). \end{aligned} \right\} \quad (2.5)$$

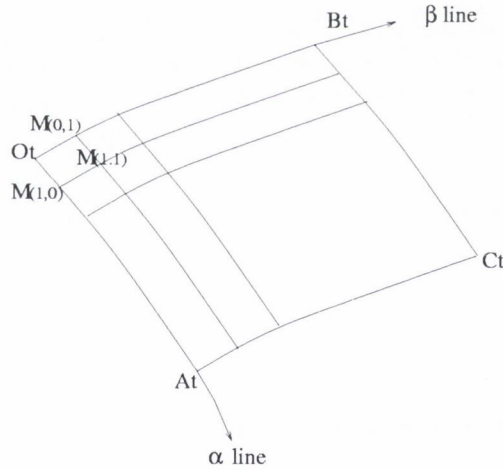


Figure 2.4: Portion of a slipline field subdivided into elemental sections

The procedure can be extended step by step over the whole field up to point C_t .

Now once the slipline field has been generated and if the components of velocity u and v are given along the sliplines $O_t A_t$ and $O_t B_t$, direct application

of the Geiringer equations allows the determination of $u_{1,0}$ and $v_{0,1}$ as a first step using:

$$\left. \begin{aligned} u_{1,1} - u_{0,1} &= \frac{1}{2}(v_{1,1} + v_{0,1})(\phi_{1,1} - \phi_{0,1}) \\ u_{1,1} - u_{1,0} &= -\frac{1}{2}(u_{1,1} + u_{1,0})(\phi_{1,1} - \phi_{1,0}). \end{aligned} \right\} \quad (2.6)$$

u and v can then be derived step by step anywhere in the field by working along the sliplines.

2.4 Requirements for a complete solution

In section (2.1), it has been seen that for complete acceptance, a slipline field should be checked to see that:

- the rate of plastic work is always positive.
- the stresses in the surrounding non-deformed material are below the yield point.

Frequently in the literature, slipline field solutions are proposed, assuming these two conditions without rigorous proof.

However, a simple test to check that the plastic energy dissipation is positive has been suggested by Ford [80]. Basically, it consists of checking that an elemental section of slipline field will deform consistently with the sign of the shear stress applied to its boundaries. Shimmin [90] gave numerical formulations based on these techniques suggested by Ford [80]. They are given in appendix (F) and will be used in the present work.

Concerning the statically admissible extension of a slipline field into all of the non-deforming regions, the stresses must be calculated in the surrounding rigid region and be shown to be below yield. Hill [91] presented a mathematical analysis and proposed a criterion for checking the stress conditions inside wedge-shaped zones, where the tip of the wedge is a point of stress singularity.

However, as pointed out by Johnson [5], this analysis is only true for frictionless tool faces and is thus not directly applicable for the present problem. Petryk [89] developed a method to extend the stress field below the boundary slipline of the slipline field solution for the wedge indentation problem. The tractions applied on this boundary slipline are the stress boundary conditions for the assumed non-deformed region and a new slipline field is constructed in that surrounding region. Through a stress analysis, he proved that the yield condition was never violated for the type of solution considered. Olver et al [92] performed a similar analysis for the problem of the indentation of a rigid die into a rigid-plastic half-space. They obtained the stresses in the plastic region with the slipline field solution and those in the contained plastic region (below the boundary slipline field of the plastic solution) by constructing an approximate slipline field, an extension of the previous one. In this work, it is clear that the surrounding region was expected to be elastoplastic in a real material.

However, the application of these analyses to the problem of the present work is not straightforward. An extension of the slipline field has to be assumed in a suitable manner and a stress analysis must be performed. This has not been performed in the present work. Regarding the time requirements of this project, it was believed that using the results of the developed model to better understand the physics of the process was more useful than to attempt to demonstrate mathematically that the solution is unique.

Conclusion

In this section, it has been shown that solving a slipline field problem consists of determining the four sets of unknowns p , ϕ , u and v , using the system of four sets of equations (2.3) and (2.4) and the available boundary conditions.

It has also been shown that there is no systematic procedure for the solution of the statically indeterminate problem of the present work. A trial and error

process has to be used.

Three main methods have been described to implement the trial and error method. The most attractive is the Matrix operation method developed by Dewhurst and Collins [85]. Unfortunately, the problem of the present work cannot be handled by this method because the presence of a curved boundary leads to non-linear equations. The trial and error process must thus be implemented either graphically or numerically. It was decided to use a numerical method to generate the fields. A description of how this can be done using the procedures given by Hill [4] has been given for a given boundary value problem.

From this analysis, it can be noted that the solution of the present problem is not straightforward. The main problem is to find a suitable way of correcting the assumptions made about the stress boundary conditions to generate a field so that successive hodographs converge. In other words, an initial slipline shape or free surface shape has to be chosen to start the generation of a slipline field. Once the associated velocity field has been generated, the solution has to be tested, thus an error function has to be defined. The initial geometry has then to be corrected in a suitable way so that the hodographs converge. The main difficulty consists in defining a geometrical convergence criterion. How this has been successfully performed in the problem of the present work is described in the next chapter.

Chapter 3

Theoretical analysis:

development of a slipline field for the sliding cylinder problem

3.1 The general slipline field structure and method of construction

3.1.1 General features of the field

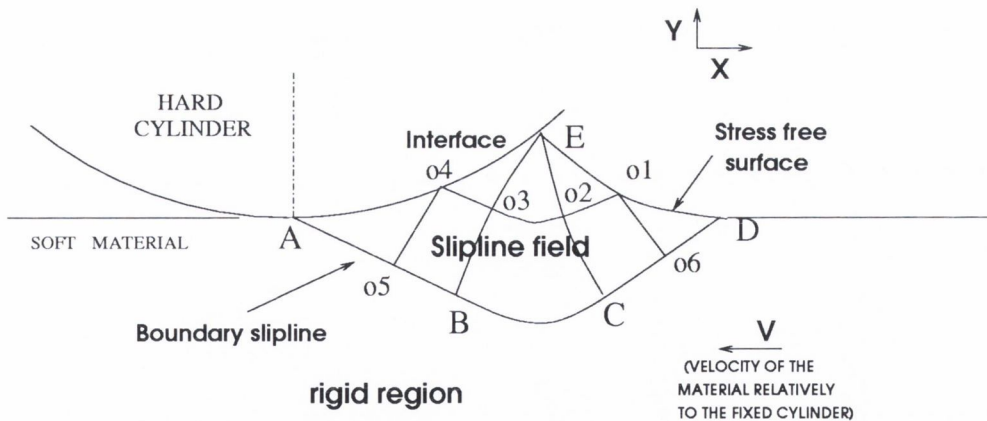


Figure 3.1: Sketch of the slipline field

To start the construction of the field a general form has to be established. As previously mentioned in chapter (2), the well established wave model developed by Challen and Oxley [2], which only differs from the present problem in the interface geometry, provides some guidance in the construction of a possible field. It is expected that the field of the present work will be of similar shape, as shown in the approximate sketch of the solution in figure (3.1). The essential features of the field can be enumerated as follows:

1. The boundary slipline $ABCD$ between the plastic region and the non-deformed material is not a line of velocity discontinuity as was the case in the wedge-shaped asperity model of Challen and Oxley [2]. This can be justified by the fact that the free surface and the interface constitute a streamline of flow and the velocity must remain tangential to it. As no geometrical discontinuity exists at the bottom point of the cylinder A, no velocity discontinuity can thus exist when the material crosses the boundary slipline (AD).
2. The free surface (ED) is tangential at D to the non deformed surface, following 1.
3. An abrupt change in the direction of flow occurs when the material meets the cylinder at E. A rapid change in stress, velocity and strain rate is expected: E is therefore a singularity and there is thus a centred fan at E.
4. The material outside the wave is rigid and moves with constant velocity V.
5. As the process does not involve removal of the deformed material, the straight line joining A and D must be parallel to the velocity V to satisfy conservation of volume.

3.1.2 Boundary Conditions

Stress boundary conditions :

Certain limitations are imposed on the angles at which the sliplines will intersect the boundaries in order that the yield criterion not be violated. They are now stated for the two boundary conditions of the problem.

- The stress boundary conditions at some point M_i of the interface (AE) between the cylinder and the deformed material are shown in figure (3.2a). If the shear stress tangential to the interface at point M is τ , it can be shown that for equilibrium, the slipline α must meet the interface at an angle γ such that:

$$\begin{aligned} k \cos 2\epsilon &= \tau \quad \text{with} \\ \epsilon &= \frac{\pi}{2} - \gamma \end{aligned} \tag{3.1}$$

Under conditions of boundary lubrication, τ is the shear strength of the boundary film and by introduction of the Tresca factor f , which is the ratio of τ , shear strength of the interfacial layer to the shear flow stress of the soft material k , equation (3.1) becomes:

$$\cos 2\epsilon = f \tag{3.2}$$

- The stress boundary conditions at some point M_f of the stress free surface (ED) are shown in figure (3.2). The sliplines must meet the stress-free surface at 45° . This is a special case of the previous stress boundary condition with $\tau = 0$.

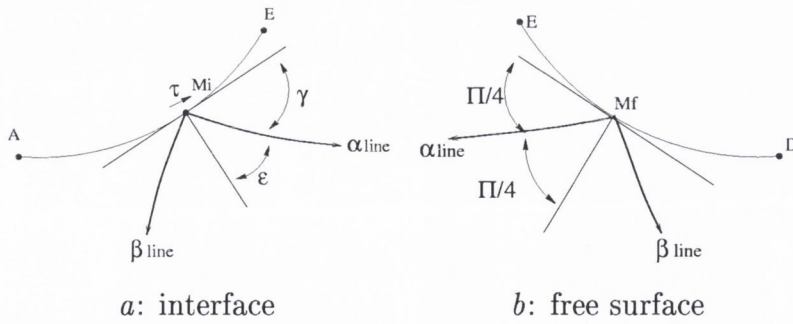


Figure 3.2: Stress boundary conditions at the interface and at the free surface

Velocity boundary conditions : (Refer to figure (3.1))

- All points of the boundary slipline (AD) have the same constant velocity V .
- The velocity vector at any point on the interface (AE) must be tangential to the cylinder.
- The velocity vector at any point on the free surface (ED) must be tangential to the free surface.

3.1.3 Construction of the slipline field solution

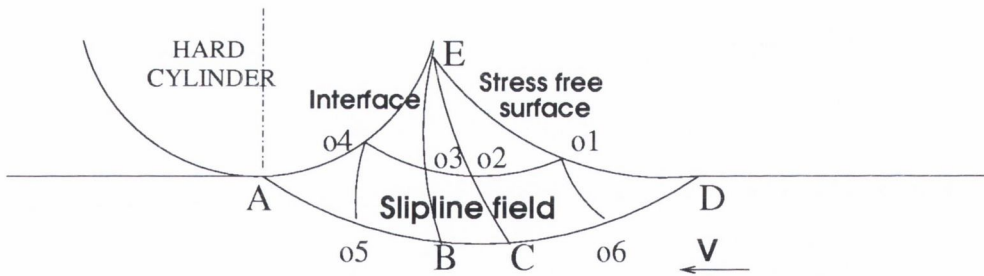


Figure 3.3: Construction of the nodal point of the slipline field

The following description refers to figure (3.3) where the field has been subdivided with only a small number of points to simplify the description of the procedure.

To start the construction of the slipline field, one of the stress boundary conditions defined by Hill [4] must be identified. Initially no sliplines are known and the shape and extent of the free surface (ED) are not defined. To get the field started therefore, the shape of the free surface (E.o1.D) and the position of the point D are assumed. As mentioned in section 3.1.2 the sliplines must meet the stress-free surface (ED) at 45° . This last situation sets up a second stress boundary value problem (SBVP2), as described in appendix (C) allowing the computation of the points o2 and o6. Then a first stress boundary value problem (SBVP1) is identified in the quadrilateral (o1.o2.C.o6) and the field can be extended up to C by working along the α line (o6C) and the β line (o2C). The slipline (Eo2C) being established and E being a singularity, the field can be extended up to o3 as a special case of the SBVP1. This establishes the α line (o2o3) and the field can then be extended up to B using an SBVP1 and by working along the α line (CB) and the β line (o3B). So far the field has been extended to the fan (EBC). The point of the interface o4 is then obtained considering an SBVP3 via an iterative routine, working along the α line (o3o4). Then an SBVP1 leads to the extension of the field up to o5. Finally the field can be extended up to A using an SBVP3 by working along the slipline (o5A). However, the position of the point A is already known. The position of D is then adjusted through an iterative routine so that the overall construction converges to the point A. Details of these calculations are given in section (3.2.2).

3.1.4 Construction of the velocity field

The following description still refers to figure (3.3). Once the slipline field has been generated one of the velocity boundary value problems has to be identified to start the construction of the velocity field. In the present configuration the velocity components are known along the boundary slipline (ABCD). The starting point of the construction is the point o5. As a velocity boundary condition is known along the interface (AE) (the velocity must be tangential

to the surface), the velocity field can be extended up to α_4 using a third velocity boundary value problem working along the β line ($\alpha_4\alpha_5$). Then by working along the α line ($\alpha_4\alpha_3\alpha_2\alpha_1$), successive first velocity boundary value problems can be identified. This establishes the velocity distribution all over the α line ($\alpha_4.\alpha_3.\alpha_2.\alpha_1$). Similar procedures allow the complete computation of the velocity distribution over the whole field. In this construction, the velocity boundary condition along the free surface (the velocity must be tangential to the free surface) is not used. This remaining condition will be used to assess the quality of the solution by comparing the velocities computed along this free surface with the known boundary condition along it. Details of these calculations are given in section (3.2.3).

3.2 Details of the programme

3.2.1 General organisation and flow diagram for the programme

To allow a complete description of a slipline field solution, the following five parameters are needed: the coordinates X , Y of the nodal points defining the field, the local angular rotation ϕ of the α line from the x axis and the velocity components u and v measured in the slipline direction. It was decided to store the computed values of these parameters in five arrays $X_{i,j}$, $Y_{i,j}$, $\phi_{i,j}$, $u_{i,j}$ and $v_{i,j}$ where i and j refer to the α and β lines respectively. The structure of these arrays is shown in figure (3.4).

The inputs of the programme for a given simulation were (see figure (3.4)):

- R , the radius of the hard cylinder
- θ , the angle of the cylinder-deformed material interface. This last parameter sets up the position of E and A and the curve defining the interface.

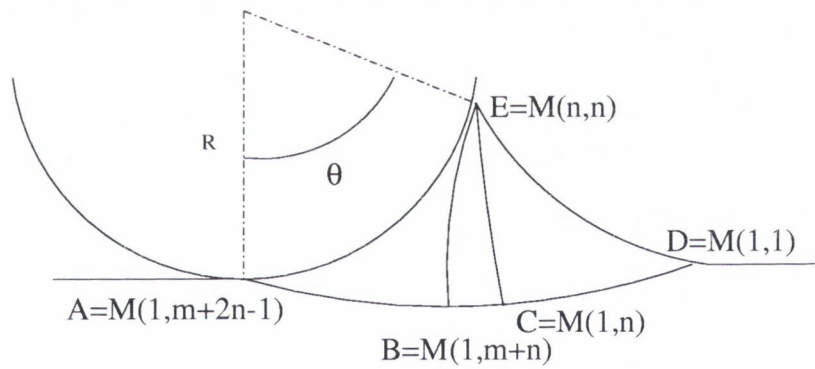
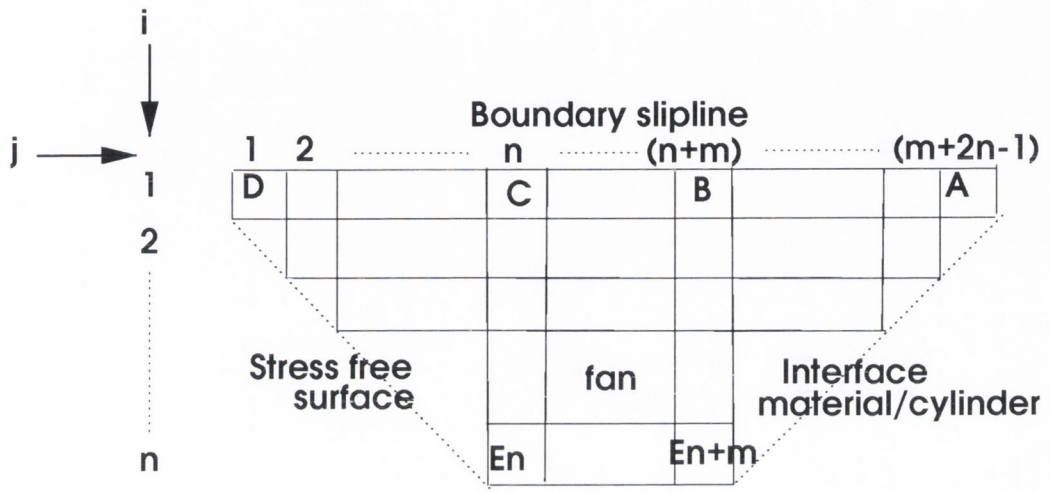


Figure 3.4: Array to store the data

- f , the Tresca factor, which sets up the angle γ such that $\cos 2\gamma = f$, at which the α lines meet the normal to the interface (see section (3.1.2)).
- k , the shear flow stress of the material
- n , number of points to describe numerically the free surface (ED)
- m , with $m + 1$ the number of β lines to describe the fan (EBC)

Some details will now be given concerning the procedure used to solve the problem. All the following explanations refer to the schematic diagram of figure 3.5.

3.2.2 Slipline field computations

Before the main calculation starts, the known boundary conditions have to be set up. Along the interface (AE), referring to figure (3.6), the conditions are:

$$X_{i,m+2n-i} = R \sin(\gamma_i), \quad (3.3)$$

$$Y_{i,m+2n-i} = R - R \cos(\gamma_i), \quad (3.4)$$

$$\phi_{i,m+2n-i} = -\frac{1}{2} \arccos(f) + \arctan\left[\frac{-X_{i,m+2n-i}}{Y_{i,m+2n-i} - R}\right] \quad (3.5)$$

As a first approximation, and for geometrical reasons, a circular arc has been chosen for the free surface. The position of D ($D = M_{1,1}$) on the axis (A, x) is decided. The free surface (ED) is split into n points $M_{i,i}$ which generates n α lines with $i_{max} = n$ at the point E. This provides the missing boundary conditions to start the generation of the slipline field. The boundary conditions along the free surface (ED) referring to figure (3.6), are:

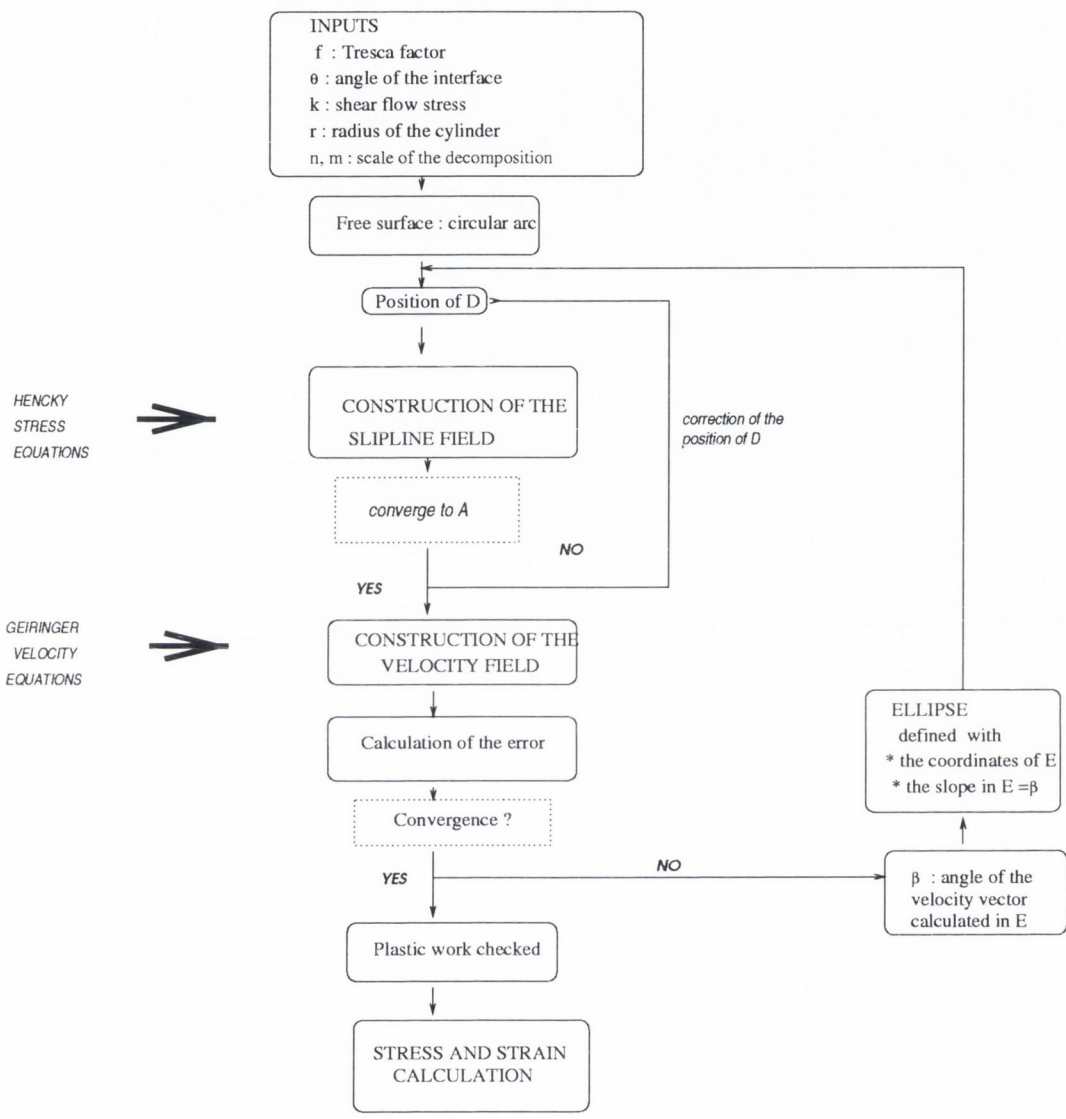


Figure 3.5: Procedure of the construction of a solution

$$X_{i,i} = R_2 \sin \gamma'_i + X_D, \quad (3.6)$$

$$Y_{i,i} = R_2 - R_2 \cos \gamma'_i, \quad (3.7)$$

$$\phi_{i,i} = \frac{\pi}{4} + \arctan\left(\frac{X_D - X_{i,i}}{Y_{i,i} - R_2}\right), \quad \text{with} \quad (3.8)$$

$$\gamma'_i = \frac{(i-1)\theta'}{(n-1)} \quad (3.9)$$

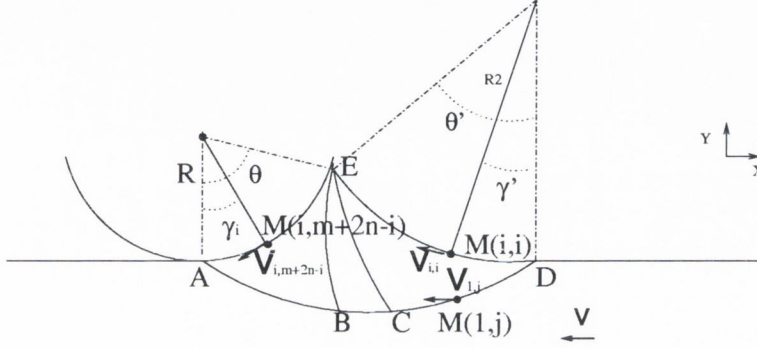


Figure 3.6: Boundary conditions

The fan (ECB) is divided into $(m+1)$ β lines which sets up the slopes at which the β lines meet E:

$$\phi_{n,j} = \phi_{n,n} - (j-n) \frac{(\phi_{n,n} - \phi_{n,n+m})}{m}; \quad \text{for } j = n, n+m \quad (3.10)$$

Once these conditions are set up, the slipline field construction can be performed as explained in section 3.1.3 starting from the n points defining the free surface. The last step of this construction is the calculation of the point A. The construction is repeated adapting the position of D on the (A,x) axis until the procedure converges to A.

3.2.3 Velocity field computations

Before starting the velocity calculations from the generated slipline field and referring to figure (4.3), the velocity boundary conditions along the boundary

slipline are:

$$u_{1,j} = -V \cos \phi_{1,j} \quad (3.11)$$

$$v_{1,j} = V \sin \phi_{1,j}; \quad \text{for } j = 2, m + 2n - 1 \quad (3.12)$$

The velocity boundary conditions along the interface (AE) are that the velocities must be tangential to the interface.

The velocity field construction is started at the nodal points of the interface as explained in section (3.1.4) and is performed step by step until the calculation of the velocities of the nodal points of the free surface is completed.

3.2.4 Optimization

Once the slipline field has been generated and the velocity field computed up to the free surface, the boundary condition expressed in 3.1.2 concerning the direction of the velocity along the free surface has not been used. This last condition is used to assess the error associated with a given computed solution. The local error at each nodal point $M_{i,i}$ of the free surface is computed as follows :

$$error(i) = \beta_{calc}(i) - \beta_{tan}(i) \quad (3.13)$$

where $\beta_{calc}(i)$ is the slope of the velocity vector referred to the (A,x) axis at the nodal point $M_{i,i}$ and $\beta_{tan}(i)$ is the slope of the vector tangent to the free surface referred to the (A, x) axis at the same point $M_{i,i}$. An average error is also defined and is computed as follows :

$$error_{aver} = \sum_{i=2}^n \frac{\beta_{calc}(i) - \beta_{tan}(i)}{n - 1} \quad (3.14)$$

For a wide range of θ and f , it was found that the circular arc is a good approximation of the free surface as small values of $error_{aver}$ were computed

when the parameters n and m were high enough. However, regarding the local error values, systematic significant local errors were observed close to the singularity E. In other words, in that area of the free surface, the deviations between the computed velocity directions and the tangent directions were more important. In order to make the errors converge to zero, it was decided to correct the shape of the free surface by using the slope of the velocity vector computed at the point E. This slope becomes the tangent to the curve at the point E and an ellipse was thus defined as the new free surface to restart the overall construction of the slipline field. This geometrical correction sets up the new boundary conditions along the free surface, which have been formulated in appendix (D).

The procedures used to compute the slipline field and the velocity field are completely identical to the ones described in sections (3.2.2) and (3.2.3). Successive ellipses were corrected this way via an iterative procedure described in the schematic diagram of figure (3.5). The trial and error process was observed to be successful as the errors converge to zero after about 5 corrections. This is shown quantitatively in chapter (4).

3.2.5 Computation of stresses and friction coefficient

The hydrostatic pressure distribution all over the field could not be found until a value of this pressure was found at one point of the plastic region. From a known value of p along any α or β line, the Hencky stress equations (2.3) allow the determination of the hydrostatic pressure everywhere in the slipline field network. This value was found using the stress boundary conditions at the free surface. As seen in section (3.1.2) and in [79], the condition that the yield criterion not be violated along a given point of the stress free surface imposes the condition:

$$p = k \tag{3.15}$$

Starting from any point of the stress-free surface and working along the α lines using the Hencky Stress Equations (2.3), the pressure distribution over the whole plastic region was computed.

Once the stresses at the interface were known, they were integrated to obtain N and F the normal and frictional resultant force per unit width respectively and thus μ the overall resulting friction coefficient of the process could be calculated. Details of these calculations are given in appendix (E).

3.2.6 Checks on plastic work

In chapter (2), it has been seen that for complete acceptance, a slipline field should be checked to see that the rate of plastic work is always positive. To verify that the condition is satisfied, we used the formulations given by Shimmin [90] based on the techniques suggested by Ford [80]. They are expressed in appendix (F). It was checked that it was everywhere positive for the range of θ and f considered.

3.3 Strain analysis

Introduction

The first aim of this model was to predict the shape and extent of the plastic region and to calculate the overall friction coefficient μ associated with the process. The second aim is to determine the plastic strain cycle undergone by the material during the deformation process because it has been shown in chapter (1) that the highly strained layer left behind the asperity after the wave has some relevance to the detachment of particles and hence wear. Data obtained from the previous part of the programme presented in the previous sections were stored for later use by the programme STRAIN. This programme, presented in this section consists of three main tasks:

- To generate the streamlines of flow from the generated slipline field and

velocity field.

- To compute a deformed grid in order to visualize the deformation undergone by the material flowing through the wave.
- To calculate from this deformed grid the precise strain pattern undergone by the material going through the wave.

3.3.1 Deformed grid generation

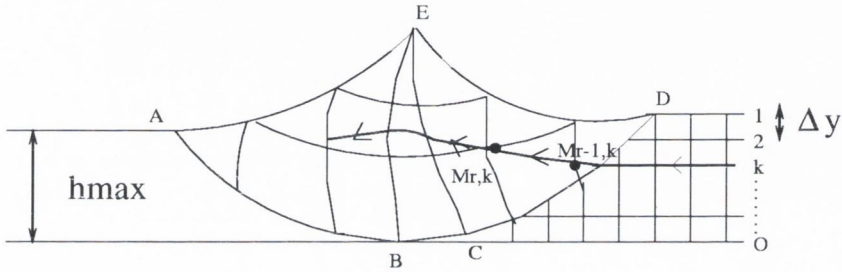


Figure 3.7: Generation of the streamlines

The plastically deformed layer was divided into a number o of equally spaced streamlines as shown in figure (3.7), having initially a spacing of:

$$\Delta y = \frac{h_{max}}{(o - 1)} \quad (3.16)$$

An initially square grid was established by making $\Delta x = \Delta y$ ahead of the plastic region. By taking $V = 1$, since the wave is assumed to be steady state, the transverse lines represent lines of equal time interval, the basic time interval being:

$$\Delta t = \frac{\Delta x}{V} = \Delta x \quad (3.17)$$

The streamlines of flow were first generated using simultaneously the slip-line field and the velocity field in a similar manner to that of Shimmin [87] for

the drawing process. The method is based on the fact that the velocity vector of a material particle must remain tangential to the streamline. As shown in figure (3.7), from $M_{r-1,k}$, which is the $(r-1)^{th}$ point generated on the k^{th} streamline (with $k_{max} = o$), a straight line was drawn using a slope equal to the velocity vector $V_{r-1,k}$. The value of the velocity vector at the point $M'_{r,k}$, the intersection of the straight line with one of the surrounding sliplines was interpolated from the Geiringer Velocity Equations. A new straight line was then constructed using a slope equal to the mean of the velocity directions of $M'_{r,k}$ and $M_{r-1,k}$. An iterative routine was then used to achieve the desired location accuracy for $M_{r,k}$, defining thus the coordinates $X_{s_{r,k}}$ and $Y_{s_{r,k}}$.

Once an intersection point has been found, the time taken for a particle to go from $M_{r-1,k}$ to $M_{r,k}$ was computed using the mean velocity and the distance of the segment $M_{r-1,k}, M_{r,k}$:

$$t_{r,k} = t_{r-1,k} + \frac{1}{2} \left(\frac{1}{V_{r,k}} + \frac{1}{V_{r-1,k}} \right) \Delta s_{r,k} \quad (3.18)$$

$$\Delta s_{r,k} = \sqrt{(X_{s_{r,k}} - X_{s_{r-1,k}})^2 + (Y_{s_{r,k}} - Y_{s_{r-1,k}})^2} \quad (3.19)$$

Following this procedure all over the field for different depths, all the points, intersection of the streamlines with the sliplines were computed and so were their associated relative times.

From the streamlines, the distorted grid was simply derived by interpolating the location of points equally spaced in time along each streamline. Their coordinates $X_{g_{w,k}}$ and $Y_{g_{w,k}}$ and their velocity $V_{w,k}$ were interpolated from the location and velocity of the points defining the streamlines.

3.3.2 Strain calculation

It was decided to compute the evolution of the direct strain ϵ_{xx} and the shear strain γ_{xy} acting parallel to the surface involved in the process. These strains, also called cyclic and ratchetting strains respectively, have been calculated by

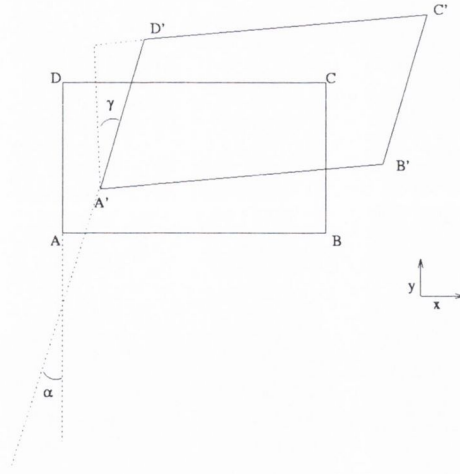


Figure 3.8: Finite strain calculation

Yang and Torrance [15] for the wedge wave model by resolving the increments of maximum shear strain into direct and shear strain components acting parallel to the surface using the hodograph (see chapter (1)). Unfortunately for the present work, the hodograph analysis is prohibitively difficult and the calculations used in the previous work cannot be used. Neither could the direct and shear strain-rates, as calculated by Farmer and Oxley [93] from a distorted grid and the velocity field, be integrated along streamlines because the wave process is a non-coaxial strain path as the principal axes rotate. It was decided then not to use the strain-rate pattern but to analyse the distorted grid by applying the basic definitions of the finite strains as formulated by Ford [80]. The direct and shear finite strains were calculated for a given grid element ($ABCD$), distorted into the parallelogram ($A'B'C'D'$), as stated in equations (3.20) which refer to figure (3.8). The shear strain γ_α was also calculated as in Yang's work [6] by comparing directly the changes in the angles of the grid lines compared with their original directions as stated in equation (3.21) which refers to figure (3.8).

$$\left. \begin{aligned} \frac{A'B'}{AB} - 1 &= \sqrt{(1 + 2\epsilon_{xx})} - 1 \\ \sin(\gamma) * (1 - 4\epsilon_{xx}^2) &= \gamma_{xy} \end{aligned} \right\} \quad (3.20)$$

$$\tan(\alpha) = \gamma_{\alpha} \quad (3.21)$$

Conclusion

In this chapter, details have been presented of how the trial and error process has been successfully implemented to determine the slipline field solution modelling the wave of plastically deformed material pushed ahead of a rigid cylinder.

A circular free surface was chosen to get an approximate solution and successive ellipse corrections made the overall construction converge to a solution which satisfies all the conditions affecting the plastic zone. Furthermore, the rate of plastic energy dissipation has been found to be everywhere positive when using the ellipse solution of the iterative process for the definition of the free surface. The solution proposed in this chapter is thus kinematically admissible and represents at least an upper bound of the complete solution.

To check whether the present solution is unique or not, the stresses must be calculated in the surrounding rigid region and be shown to be below yield. This is not a straightforward analysis as it consists of analysing the stresses in the half space, whose boundary condition is the boundary slipline of the plastic region. As the mathematical analysis used by previous authors, such as [91], [89], [92] is not directly applicable to the present problem, this has not been performed in the present work. Regarding the time requirements of this project, it was believed that using the results of the developed model to better understand the physics of the process was more useful than attempting to demonstrate mathematically that the solution is unique. Thus the solution

presented here has to be considered incomplete until a statically admissible extension of the plastic stress field into rigid regions is proved to exist.

Finally the developed model is a tool which is able to:

- predict the shape and extent of the plastic region and calculate the overall friction coefficient μ associated with the process.
- predict the plastic strain cycle undergone by the material during the deformation process.

These results are presented in the next chapter and compared with the results of previous work.

Chapter 4

Results of the model

4.1 Main features of the solution

4.1.1 The slipline field and velocity field solution

The slipline field (4.2) was obtained with a circular free surface and the input parameters given in figure (4.1). In figure (4.2), the dotted lines represent the sliplines which have some curvature and their intersections are the nodal points calculated by the progame. To simplify the analysis, the usual hodograph drawn in most plasticity problems to represent the velocity field is not used in the present work. The alternative velocity field analysis introduced in chapter 3 and presented here is equivalent to ensuring consistency or convergence of the traditional hodograph. The velocity distribution calculated from the slipline field of figure (4.2) is plotted in figure (4.3) where the arrows represent the velocity vector expressed in the reference frame (X, Y) at each nodal point of the field.

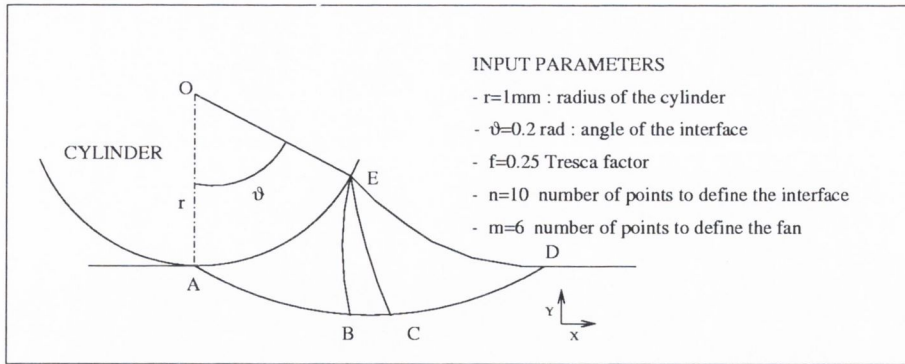


Figure 4.1: Inputs of the simulation

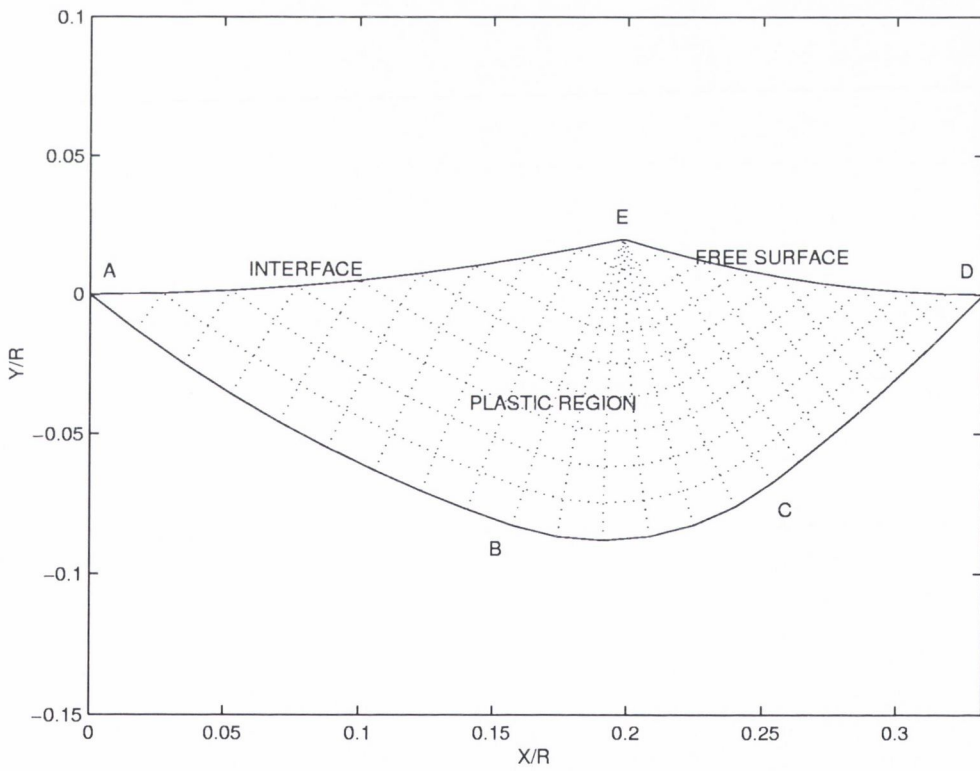


Figure 4.2: Slipline field solution

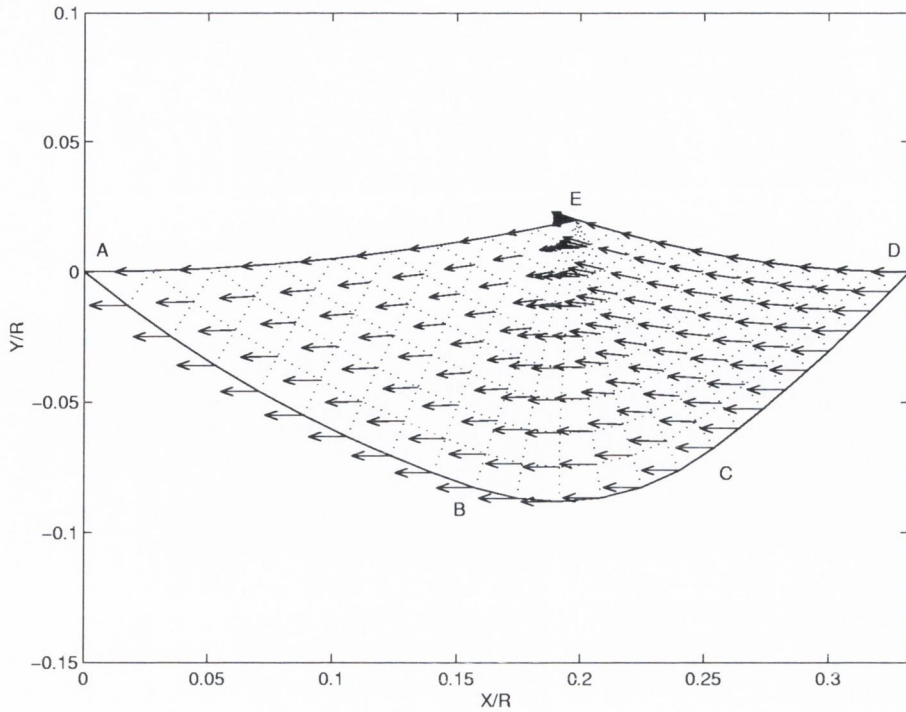


Figure 4.3: Velocity field solution

4.1.2 Optimization

To construct the velocity field, the velocity boundary condition along the free surface is not used. In figure (4.3), it can be seen that the velocity vectors computed along the free surface (ED) are reasonably tangential to it and thus the circular arc is a good approximation to the free surface shape solution. The deviations from this last condition are quantified by the local errors calculated at each nodal point of the free surface as explained in 3. They are plotted in figure (4.4) against the X coordinates of the nodal point (lines with stars). The computed errors are small (less than 0.5°). The associated average error is $error_{aver} = 0.087 \text{ deg}$, which is surprisingly small considering the different underlying approximations used to construct this numerical solution. This would confirm the choice of the circular arc which might be the correct free surface shape of a possible analytical solution of the present problem, or at least very close to it.

To improve the accuracy of the calculations, the first approach is to increase the number of nodal points n and m to define the circular free surface and the fan respectively. Table (4.1) shows how the average local error and the maximum local error vary with the parameters n and m . It can be seen that increasing the number of nodal points leads to a slight decrease of the average error. However, the maximal local error remains constant. It can be argued that for a numerically obtained solution, the errors are very small. However, a proper trial and error process has not yet been performed.

Thus, the previous solution has been numerically optimized by adjusting the shape of the free surface via the iterative procedure explained in chapter 3. In figure (4.4), the full lines represent the evolution of the local errors after successive corrections of the free surface using ellipses. It can be seen that the use of the successive ellipses make the error converge to near zero.

n	10	100	200	500
m	6	100	200	500
$error_{aver}/^\circ$	0.087	0.071	0.07	0.07
maximum $error_{local}/^\circ$	0.25	0.25	0.25	0.25

Table 4.1: Evolution of the errors with the parameters n and m

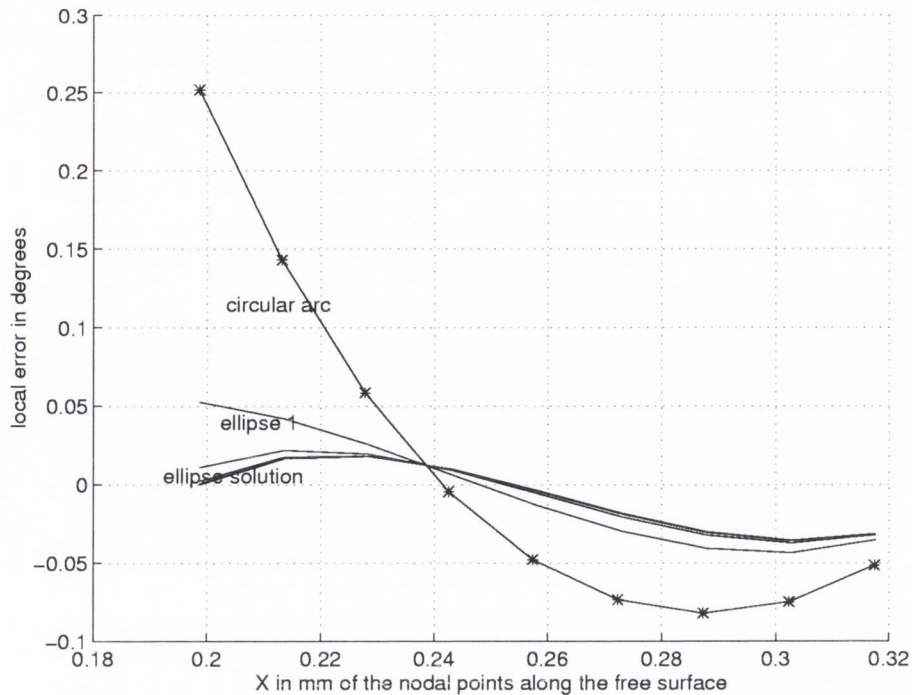


Figure 4.4: Evolution of the local errors after the free surface shape corrections

No significant differences were observed in the friction and strain results whether a circular arc or an ellipse was taken for the free surface. Thus all the following results, when not otherwise specified have been obtained with a circular arc.

4.1.3 Limitations of the model

It has been verified that the developed model is suitable for a wide range of f and θ . However, it was observed that it becomes increasingly more difficult to make the solution converge when f and θ are increased. Figure (4.5) shows the dramatic increase of $(error)_{aver}$ for high values of θ and f . Furthermore the condition concerning the plastic work dissipation is no longer obeyed for high values of f and θ , whether the free surface is a circular arc or an ellipse. This last trend is not surprising as a change of regime is expected when the asperity penetration becomes greater and the lubrication poorer. This establishes the

basis of the limits of application of the model which is more suitable for small values of θ and f . This was also predicted by the chord approximation model of Challen and Oxley [1] who proposed a chip formation model (double chord model) as an alternative to the single chord model which was no longer suitable for high loads and very poor lubrication.

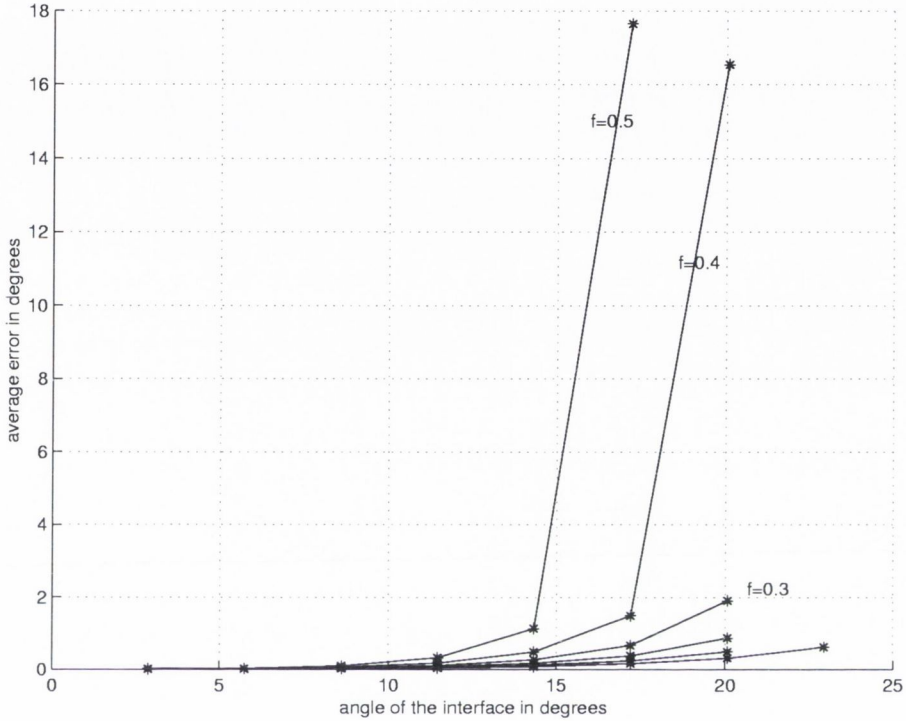


Figure 4.5: Evolution of the average error with θ

4.2 Friction results

4.2.1 Evolution of friction as a function of θ , the angle of the interface and f , the Tresca factor.

For the wedge-shaped asperity model of Challen and Oxley [2], α , the angle of the wedge was an independent variable. Thus it was not related to changes in the normal load N which had only the effect of changing the contact length at

the interface and thus the scale of the plastic region. However for the model developed in the present work and as pointed out by Challen and Oxley [1], the contact length and α , the angle of the chord at the interface, are inter-related. The angle α or the equivalent angle θ used in the present work, are influenced by changes in the normal load as is μ , the friction coefficient. The evolution of the angle θ has been plotted in figure (4.6) as a function of the non dimensional parameter N/kR , where N is the normal load per unit length, k is the shear flow stress of the deformed material and R is the radius of the cylinder, for different values f of the Tresca factor. The evolution of the friction coefficient μ has been analyzed as a function of the non dimensional parameter N/kR .

A friction map has been established in figure (4.7) from the predictions of the developed model. It can be seen that for a given interfacial film strength f , it is predicted that the friction coefficient μ increases with the angle of the interface θ over the entire range of conditions considered. This increase of friction with surface roughness is in agreement with the trends usually observed in experiments (see chapter (1)).

It can be observed also that a decrease in f (i.e., for better lubrication conditions) is predicted to reduce μ . For the highest values of f considered, even a small reduction in f can cause μ to fall rapidly.

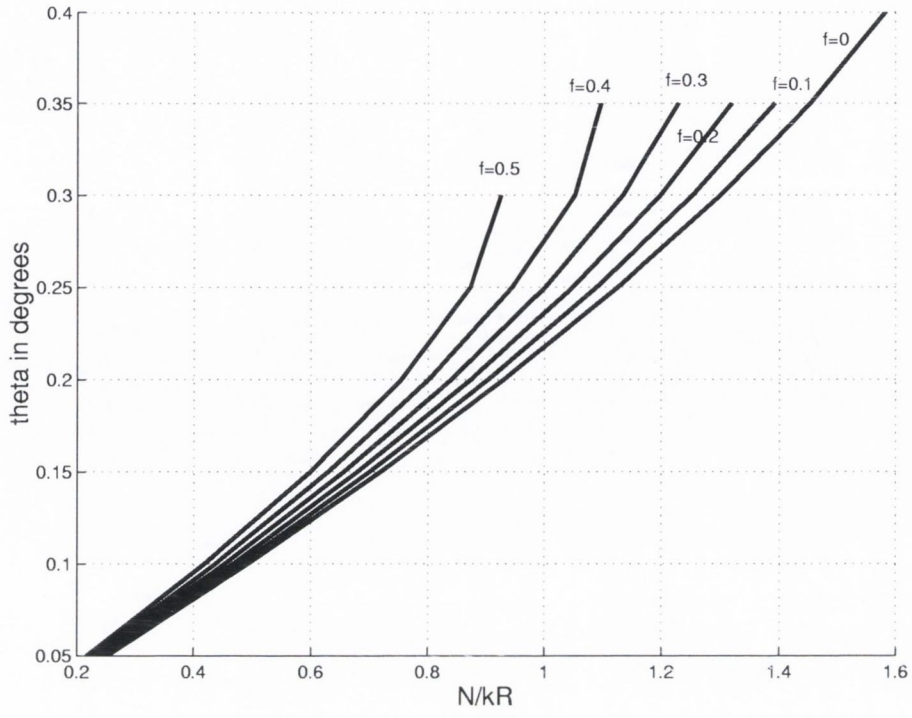


Figure 4.6: Evolution of θ with N/kR for different f

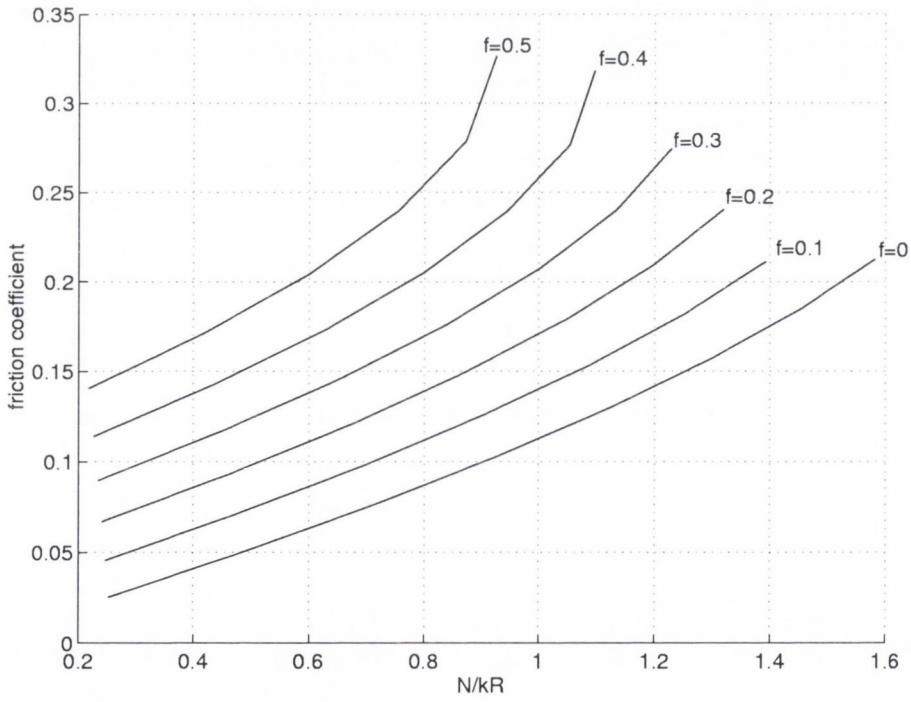
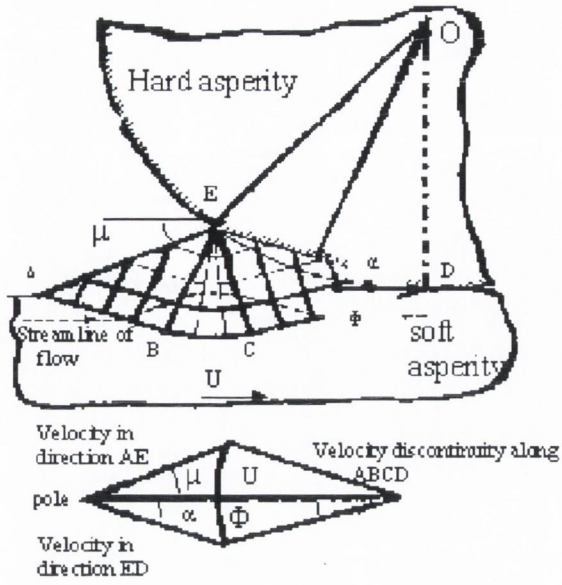


Figure 4.7: Evolution of μ with f and N/kR

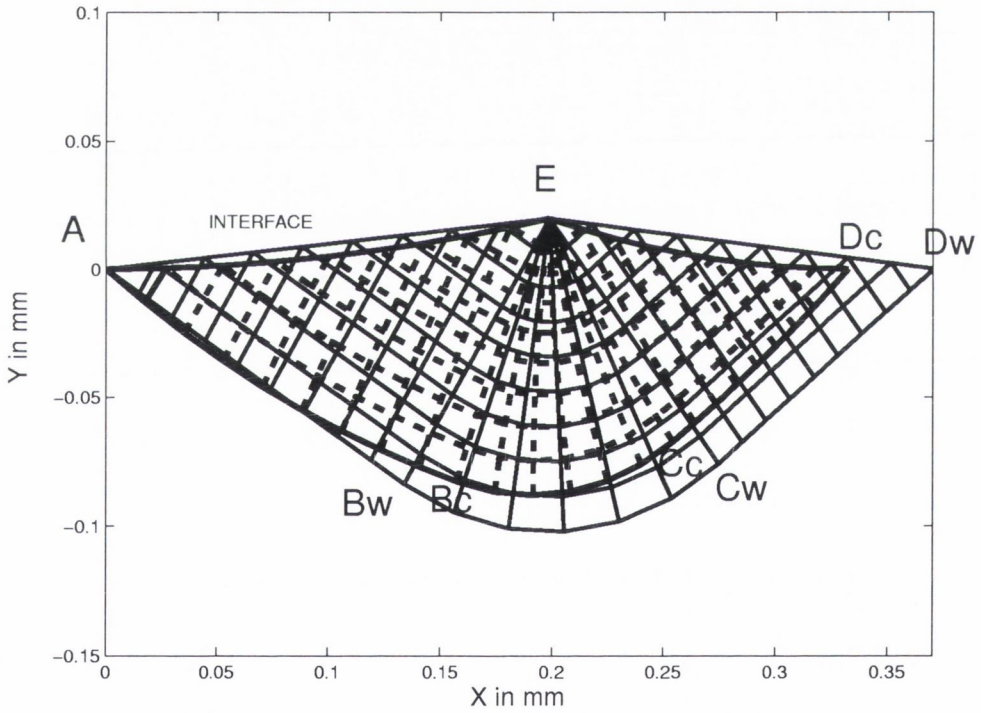
4.2.2 Comparison with the chord approximation model developed by Challen and Oxley [1]

As mentioned before, one attempt to provide a simple slipline field for the configuration under investigation is the chord approximation model suggested by Challen and Oxley [1] as shown in figure (4.8a). In this model, the circular interface between the hard cylinder and the deforming material is approximated by its chord allowing the use of the well established wedge wave model slipline field [2]. In figure (4.8b), both slipline fields calculated with the parameters used in the previous section are plotted. It can be seen that the plastic zone predicted by the numerical model is relatively less extended than as predicted by the chord model (This last field is plotted as (A.Bw.Cw.Dw.E) in figure (4.8b)). This can be simply explained by the fact that the interface of the chord model is straight and that there are some restrictions placed on the geometry of any slipline field such as, for example, the straight slipline or uniform stress state areas imposed for this field; it follows that the chord model has to extend deeper and further ahead of the cylinder to meet the straight free surface at 45° than the numerical model which is curvilinear.

However, these geometrical differences become meaningless when the friction coefficient predictions of the two models are compared for the lowest loads. In figure (4.9), the friction coefficient predictions of the chord model (stars) are plotted against N/kr with the friction coefficient predictions of the numerical model of the present work (full lines). It can be clearly seen that both models are in good qualitative agreement in terms of friction predictions. However, the predictions of the numerical model are always higher than the chord model and this becomes significant for high loads, which can be explained by the geometrical differences pointed out previously. Especially for low loads where the chord closely approximates the arc of the circle at the interface, both models are in excellent agreement.



a: chord model of Challen and Oxley [1].



b: comparison of the two models.

Figure 4.8: Comparison between the wave model and the model developed in the present work.

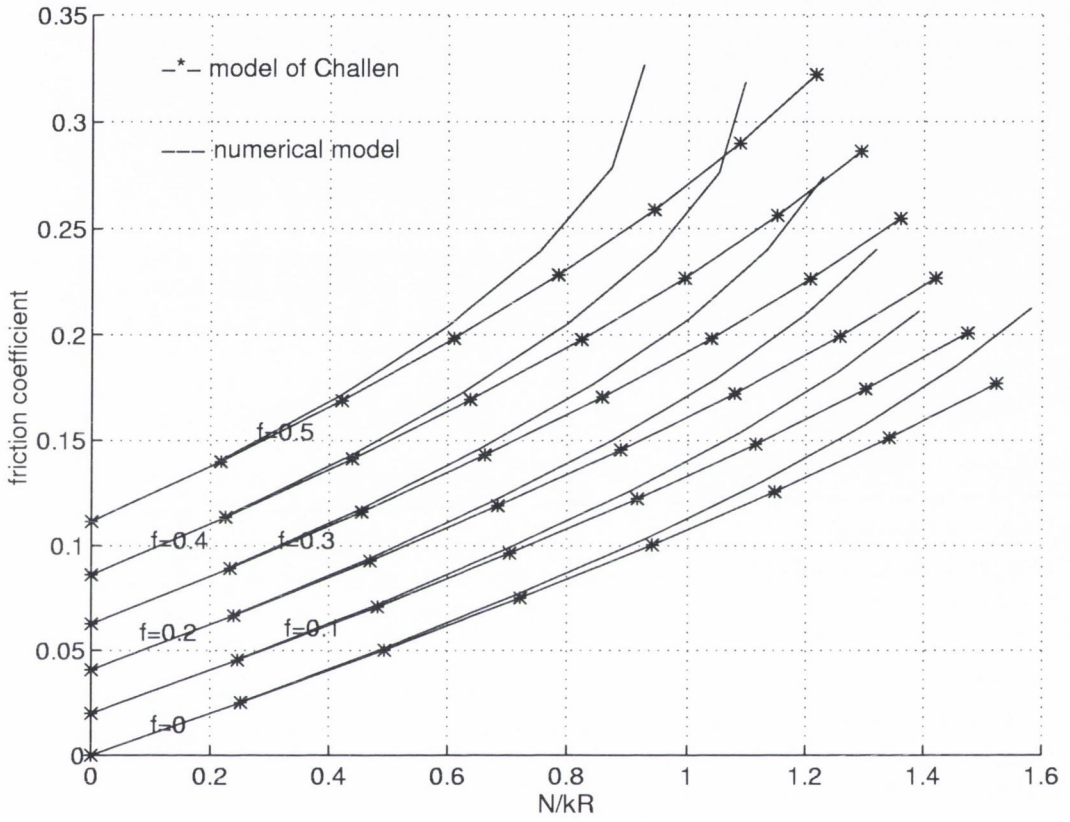


Figure 4.9: Comparison of the friction predictions of the chord model [1] and the model developed in the present work

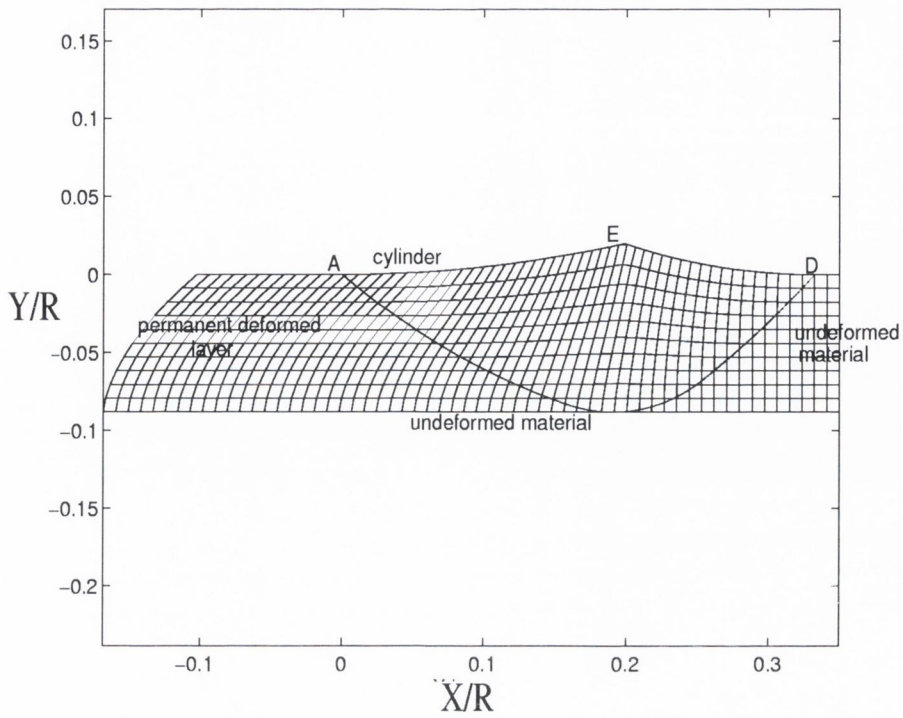
4.3 Strain results

4.3.1 Deformation of a grid

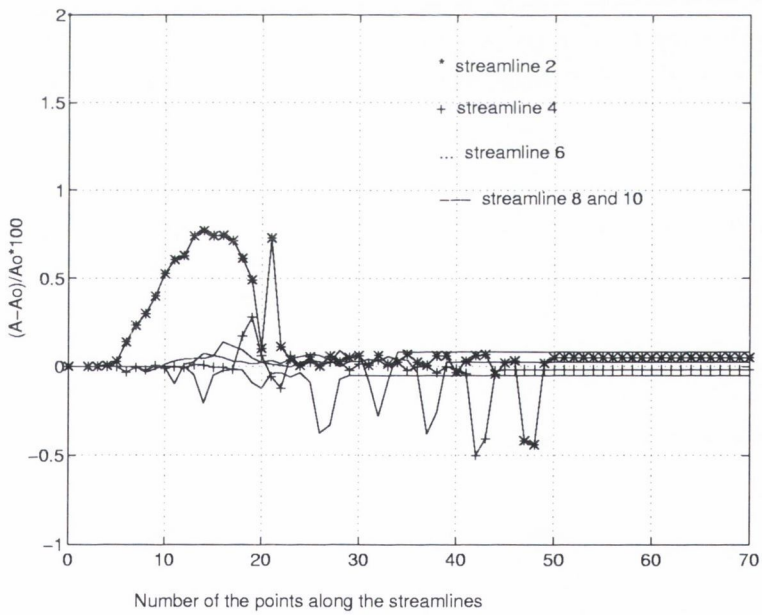
From the velocity field of section 4.1.1, the deformation of a grid has been generated in figure (4.10a). The originally horizontal grid lines are the streamlines of flow and their intersection points with the originally vertical lines represent points of equal time interval along the streamlines.

The accuracy of this distorted grid depends on the number of sliplines and thus on the parameters n and m . One way to assess this accuracy is to compute the evolution of the grid element areas during the deformation process. Under two-dimensional plane strain conditions, these areas must remain reasonably constant to have the constant volume conditions satisfied. In figure (4.10b), the evolution of the area A of the grid elements compared to the initial grid element area A_o has been plotted along the streamlines for different depths. The deviations from the initial grid area are quite low whatever the depth with a maximum of 1%. This means that the method used so far is reasonably accurate because the constant volume condition in plane strain is satisfied as closely as the finite difference technique allows.

Observation of the grid shows that the type of plastic flow is shear relative to the non-deformed material. The incremental shearing of the material can be followed along the streamlines and appears to depend on depth. This last feature is not predicted by the single chord approximation model of Challen and Oxley [1]. The velocity field analysis of their chord model leads to a homogeneously deformed layer and the shearing represents an average within the deformed layer. The model obtained in the present work seems to offer more detailed information concerning the deformation pattern. The analysis and calculation of section (4.3.2) will give a quantitative estimate of the strain cycle undergone by the material and shed light on the depth-dependent highly strained layer often observed beneath the surface.



a: distorted grid



b: evolution of $\frac{(A-A_o)}{A_o} * 100$

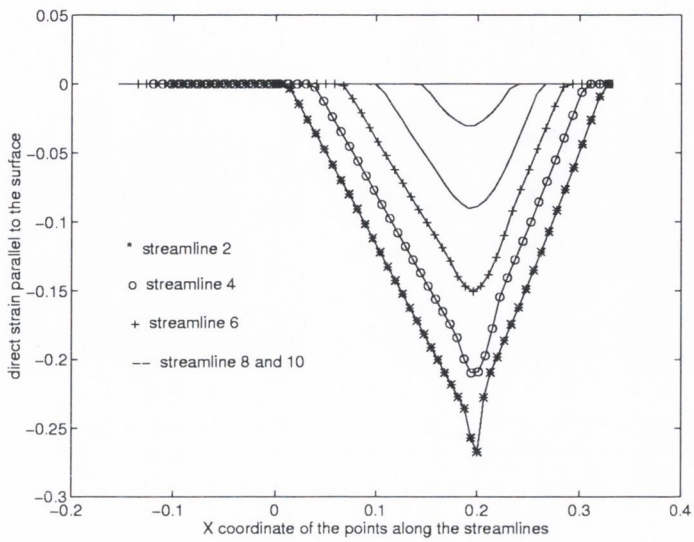
Figure 4.10: Deformation of an initially square grid. $n=100$; $m=100$; $o=100$ and deviations from the constant volume condition

4.3.2 Strain calculation

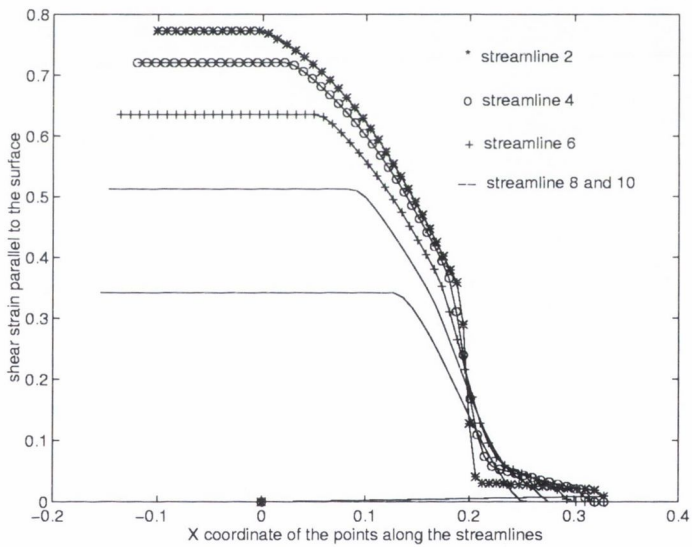
Figures (4.11a) and (4.11b) show how the direct and ratchetting strains ϵ_{xx} and γ_{xy} are predicted to vary along a selection of streamlines of the distorted grid of figure (4.10a). The strain cycle is not fully reversing; the direct strain cycle ϵ_{xx} fully reverses but the shear strain cycle γ_{xy} does not reverse at all. There is a shear strain increment $\Delta\gamma_{xy}$. The direct strain cycle ϵ_{xx} , though fully reversing, was not directly observable on the distorted grid. However it must be considered as it might be of some relevance in the failure of the surface as was described in chapter (1).

Figure (4.12a) shows how these strain cycles compare with the predictions of the chord model [1] for the same conditions. As previously observed on the distorted grid of section (4.3.1), the main difference is that the strains calculated from our model vary with depth, being higher than the predictions of the chord model near the surface, and falling to zero at the boundary of the field. This is reflected also in the shear strains left in the surface once the wave has passed as shown in figure (4.12b) .

Furthermore, the rigid-plastic boundary of the chord model [1] is a line of velocity discontinuity. Thus, as stated by Kopalinsky [7], a direct consequence of this is that their model predicts an infinite strain rate and hence a sudden increase in strain at the bottom of the plastic region. This is not realistic in terms of material behaviour. This problem is avoided by the field we have proposed here.

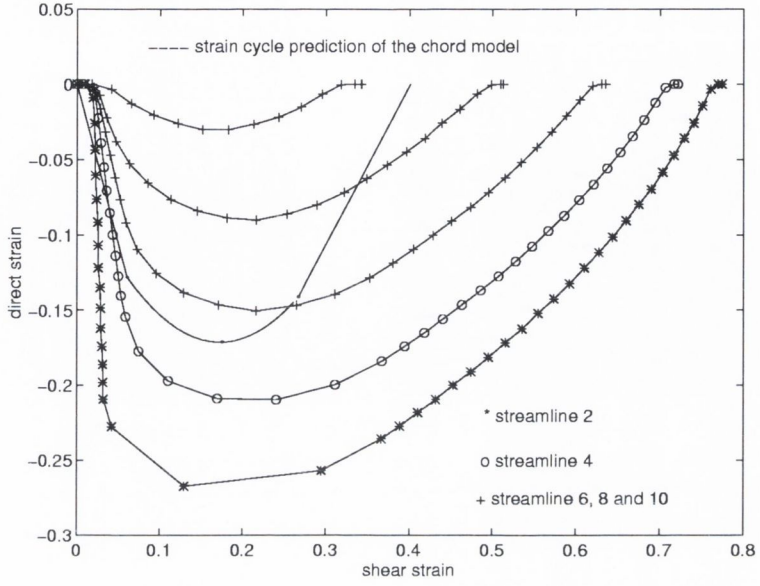


a: ϵ_{xx}

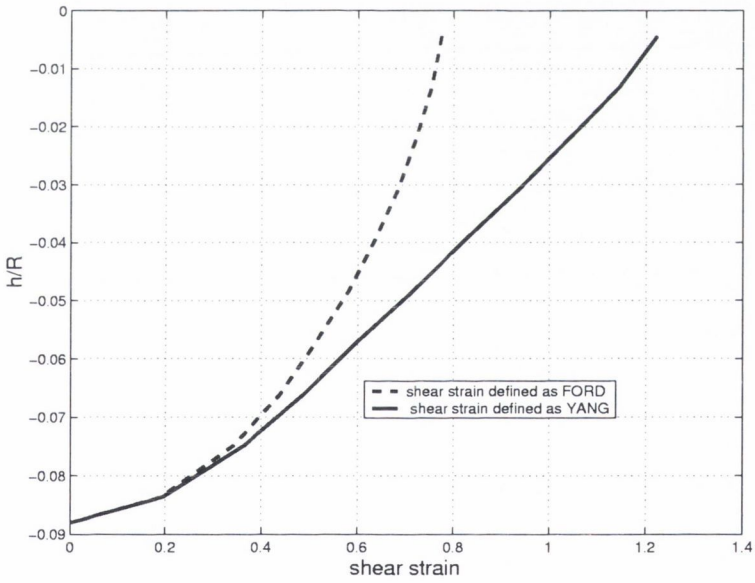


b: γ_{xy}

Figure 4.11: Strain results- $n = 100$, $m = 100$, $o = 10$ — $f = 0.25$, $\theta = 0.2\text{rad}$.



a: ϵ_{xx} versus γ_{xy}



b: $\Delta\gamma_{xy}$, [80] and γ_{α} , [6] versus the depth

Figure 4.12: Strain results- $n = 100$, $m = 100$, $o = 10$ — $f = 0.25$, $\theta = 0.2\text{rad}$.

4.3.3 Comparison with finite element analysis

One potential defect of the slipline field theory is that it takes no account of elasticity. It is often argued that elastic effects cannot be neglected, especially for the cylinder/plane configuration and the simplifications inherent in any slipline field solution are less realistic. To investigate this further, some elastoplastic finite element models have been constructed using commercial software (ANSYS 5.4) to represent a hard cylinder indenting and sliding over an aluminium alloy for various loads N/kR . No friction was considered at the interface (i.e. $f = 0$). The basic finite element model and conditions for the different simulations are described in appendix (J). The deformation pattern obtained for a simulation ($N/kR = 1.6$, $f = 0$) is plotted in figure (4.13).

As predicted by our numerical model, the deformation pattern shows the presence of a plastically deformed wave pushed ahead of the cylinder in the soft material. It would confirm the presence of a strained layer at and beneath the surface of the softer material. However, the finite element simulation of figure (4.13) shows the presence of a trailing wave behind the center line of the cylinder. This trailing wave does not exist in our slipline field model, where the last point in contact between the cylinder and the soft material is on the center line of the cylinder.

In figure (4.15), the friction predictions of the finite element models (circles) are compared to the predictions of our numerical model (line). It can be seen that the friction coefficients are predicted to increase with load as in our numerical model but are lower for the load range considered. These results confirm the finite element analysis results of Bressan et al [53] for an elastoplastic wave pushed ahead of a cylinder. The authors found also lower values of friction coefficients than slipline field theory in the elasto-plastic range and a friction free interface.

In order to investigate the influence of the trailing interface and elastic effects, some elasto-plastic finite element models with a cut cylinder have been

developed to create a geometrical discontinuity and in this way to remove the trailing interface. The basic model is presented in appendix (J) and a simulation is shown in figure (4.14) ($N/kR = 1.3, f = 0$).

In figure (4.15), the friction predictions of these finite element models (full diamonds) are compared to the predictions of our numerical model (line). It can be seen that friction coefficients are higher than for the full cylinder configuration, once the trailing wave is removed and elastic effects are decreased. However, friction coefficients are still lower than slipline field theory.

← Motion of the cylinder

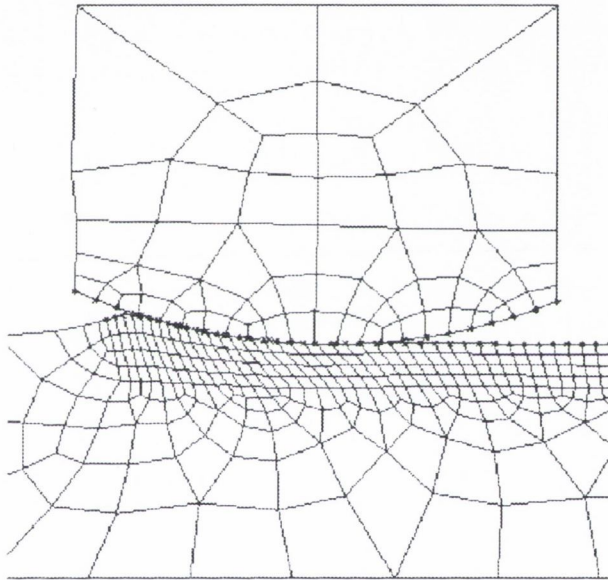


Figure 4.13: Deformation pattern obtained by finite element analysis with a full cylinder - $N/kR = 1.6, f = 0$

← Motion of the cylinder

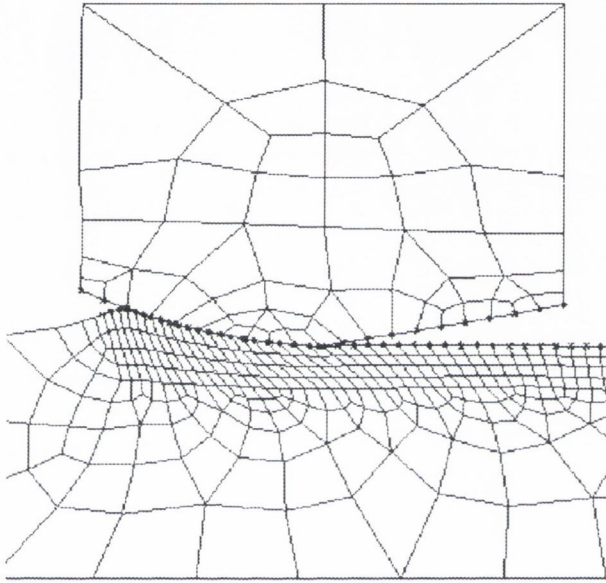


Figure 4.14: Deformation pattern obtained by finite element analysis with a cut cylinder - $N/kR = 1.3$, $f = 0$

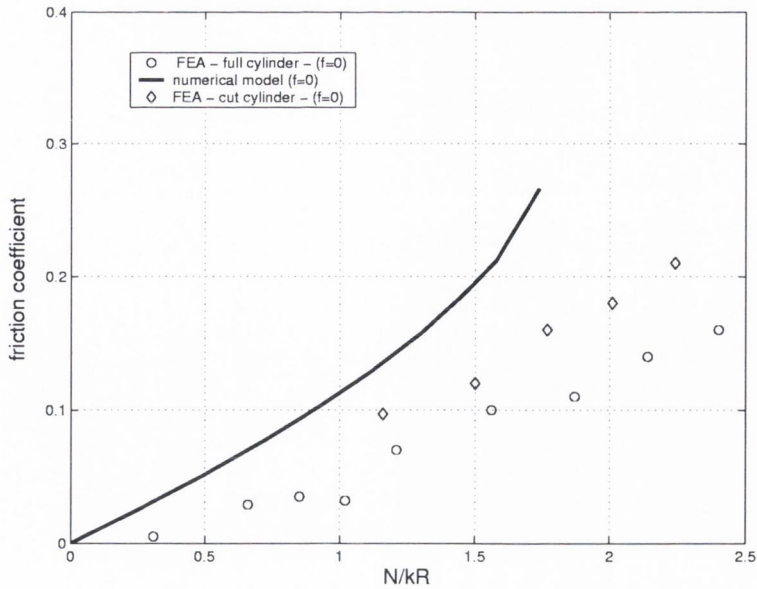


Figure 4.15: Comparison between the friction predictions of the finite element analysis our numerical model

Conclusion

In this chapter, the results of the numerical slipline field developed to model the plastic wave pushed ahead of a hard cylindrical slider have been presented. The main results can be summarized as:

- The friction predictions are in good agreement with the chord approximation model proposed by Challen and Oxley [1] in the loading conditions considered. However, for the highest loads, friction is predicted to be higher. Therefore, both models can be used to compute the friction coefficient μ for given f and θ at lower values of f and θ .
- The strain pattern calculated by the model presented differs from the predictions of the chord model [1]. The main difference is that the strains vary with depth, being higher than the predictions of the chord model near the surface, and falling to zero at the boundary of the field. Thus our numerical model offers more refined information concerning the de-

formation pattern. Appendix (G) shows a series of maps, that give the evolution of the strain pattern for a wide range of conditions.

- The model is not quantitatively suitable to predict friction and deformation of a material when elasticity is significant. Elastoplastic finite element analysis shows the presence of a trailing wave, which has the effect of decreasing the friction and deformation associated with the process. However, when the trailing edge of the cylinder is removed, elastic effects are decreased. Friction coefficients rise but are still lower than predicted by our numerical model.

These results are expected because for a real material and for low loads, the elastic contribution to deformation becomes significant and the simplifications inherent in any slipline field solution less realistic.

- The complete simulation (slipline field and velocity field calculations, friction and strain calculations) presented in this chapter ($\theta = 0.2rad$, $f = 0.25$, $n = 100$, $m = 100$), took approximately 2 minutes on 350MHz Pentium PC with 64 Mb RAM.

Chapter 5

Experimental methods

The first part of the experimental investigation consists of testing the predictions of slipline field theory when a rigid cylinder slides across a soft surface. Details of the experiments and the equipment involved are given in this chapter.

The second part of the experimental work consists of investigating the influence of detached particles accumulated around the contact when a rigid cylinder slides across a soft surface. To do so, a joint project has been carried out between our team and the Laboratoire de Mecanique des Contacts, I.N.S.A. de Lyon, France. This French team is specialized in the analysis of solid lubrication or solid third body and has experimental expertise in the dynamic observation of solid particle flows and rheology as an aid to friction interpretation. For the present work, the technique of visualization through a transparent tool, developed in the L.M.C. has been used. Details concerning the visualisation technique and the tests performed for the present investigation are also presented in this chapter.

5.1 Experimental investigation of a hard cylinder in C.B.N. sliding across two non-ferrous metals

5.1.1 Objectives

The objectives of the first part of the experimental work were to:

1. use a single cylindrical asperity indenting a soft surface with different loads per unit width N or equivalent non-dimensional parameters N/kR and obtain the friction coefficient μ .
2. use a single cylindrical asperity, whose trailing edge has been removed, indenting a soft surface with different loads per unit width N and obtain the friction coefficient μ .
3. collect the detached particles for further examination.
4. approximate plane-strain conditions.

5.1.2 Experimental set-up

MATERIAL AND GEOMETRY

Materials tested

The materials selected for these tests were :

- aluminium alloy, spec. 2011.
- hard-drawn copper, spec. BS2874 C101(99% pure copper)

The material properties are shown in figure (5.1). These two non-ferrous materials were chosen because they have differing ductilities and different ratio (E/σ_y), which quantifies the degree of elasticity of the materials.

Furthermore, copper presents almost no strain-hardening as shown by the compression test presented in appendix (L). This means that copper is expected to have a behaviour close to ideal plasticity for high strain.

The test pieces were bar-shaped, as shown in figure (5.2), with a diameter of approximately 30 mm.

	Hardness	k s (MPa)	σ_y (MPa)	E (GPa)	Reduction in Area	ϵ_f	E/ σ_y
ALUMINIUM ALLOY	123 Hv	232	402	80	16%	0.17	199
COPPER	95 Hv	179	310	95	78%	1.51	306
C.B.N.				550			

Notes: ϵ_f obtained from $\epsilon_f = -\ln[(100-R.A.)/100]$

$\sigma_y = 9.81Hv/3$

Figure 5.1: Material properties



Figure 5.2: Bar of tested material

Tools

Two sets of tests S_1 and S_2 were performed with two different tools. A two-dimensional view of these tools in C.B.N. (Cubic Boron Nitride) is shown in figures (5.3a), (5.4a) and the resulting contact geometries are shown in figures (5.3b), (5.4b). These tests can be described as follows:

1. The first set of tests S_1 was performed with a full cylinder of radius of 1.57 mm, as shown in figure (5.3).
2. The second set of tests S_2 was performed with a cut cylinder, as shown in figure (5.4). It can be observed that the leading side of the cylinder has been partly removed. In other words, the lowest point in contact between the tool and the workpiece will not be on the centre line of the cylinder. The reason is that the cut cylinder has been obtained by grinding an initial cylinder and the lack of accuracy in the grinding operation caused the leading side of the cylinder to be partly removed. In order to account for this configuration, the chord model [1] has already been developed by Busquet and Torrance [3]. Equations for this developed model are given in appendix (B).

The tools were 3.15mm in width.

It should be noted that a sort of very thin aluminium or copper coating was observed on the C.B.N. tools just after their first use even after cleaning with acetone. Two distinct cylinders were used for the tests S_{1al} and S_{1co} for aluminium and copper respectively in order to reduce possible modifications of the physical-chemistry at the interface (due to a mixture copper/aluminium) and thus the Tresca factor f .

However, as the grinding operation to obtain the cut cylinder was not repeatable with a high accuracy and as we wanted to compare the results between the two materials, the same cut cylinder was used for the tests S_{2al} and S_{2co} for aluminium and copper respectively.

For a given material and for a given set of tests, the same tool was used for all the friction measurements, since no significant wear of the C.B.N. was observed. Between each test, the C.B.N. tool was cleaned with acetone and then put in a new position on the metal bar for the next test.

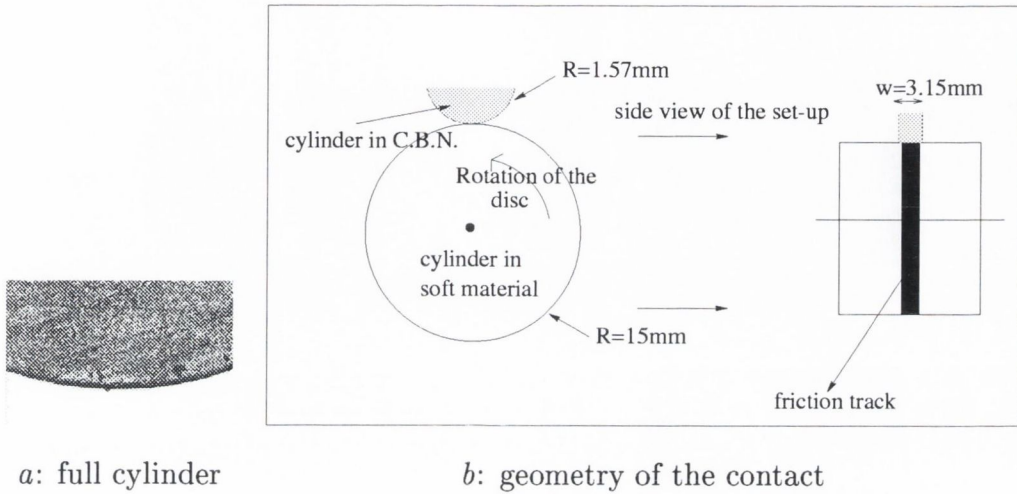


Figure 5.3: S1 set

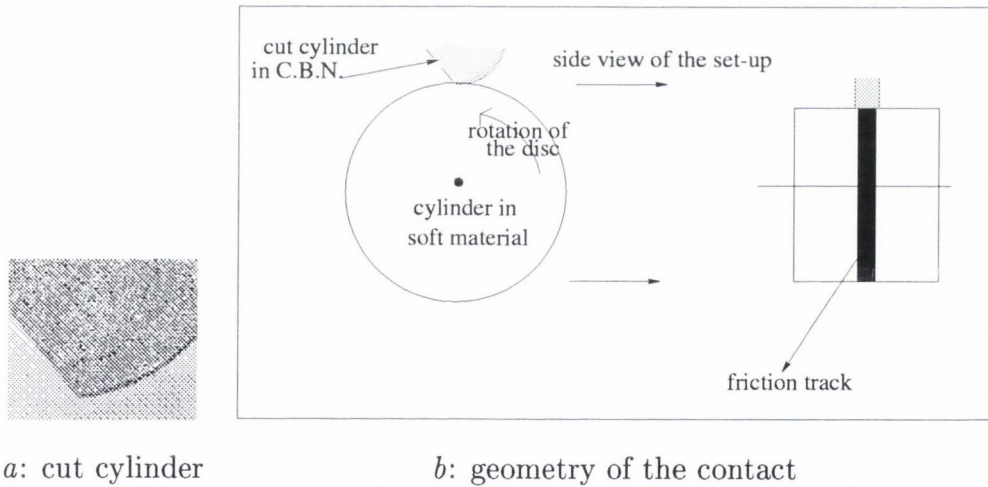


Figure 5.4: S2 set

SET-UP

The set-up, developed in previous work [15, 16, 6], is shown schematically in figure (5.5). The C.B.N. tool (wedge or cylinder) was mounted in the loading arm and was pressed against the periphery of the softer metal bar rotating on a lathe, by tightening the loading bolt. One end of the soft metal bar was held in the lathe chuck and the other end was supported on a running centre.

The tool, its holder and the loading set-up were mounted on a 3 axis Kistler 8257B dynamometer fixed to the saddle of the lathe. The signal was fed through two Kistler 5011 Charge amplifiers, connected to a chart recorder and a personal computer with the DASH 300 software package so that normal and frictional forces could be controlled and recorded during the tests.

Lubrication was provided by 1% stearic acid in white medicinal oil (refer to chapter (1)). This was fed onto the surface of the bar through a sponge (quantity: < 2.5ml).

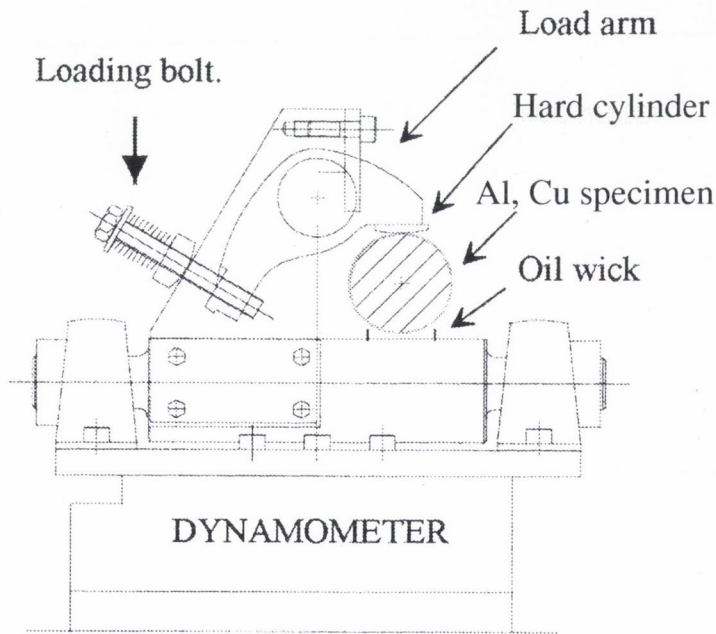


Figure 5.5: Schematics of the set-up used

5.1.3 Experimental procedure

Before a test, the position of the hard asperity relative to the test piece was carefully adjusted. This was to ensure that the lowest line of the cylinder was positioned to contact the bar at its highest point. The lathe was set rotating at 35rev/min, the minimum velocity that the lathe could achieve.

After the chart recorder and Dash 300 were set for operation, the loading bolt was tightened to apply the test load. The normal and tangential forces measured by the dynamometer were processed and determined by the deflections of the pens of the chart recorder which gave the value of the normal load. In order that the normal load remains constant during the selected running time, the loading bolt had to be adjusted from time to time in accordance with the readings of the chart recorder. When the time was finished, the loading bolt was released and the normal load reduced to zero while the test-piece was still running. Tests ran between 1 and 2 minutes.

After some of the tests, the tool was carefully dismantled and directly observed with an optical microscope. The detached particles accumulated around the contact area during a test could then be directly observed on the tool. These particle conglomerates were then deposited on a filter paper, cleaned and preserved for further observation with electron microscopy.

5.1.4 Test conditions and parameters involved

A series of tests was carried out to fulfil the experimental objectives. The main variable parameter was the normal load per unit width N applied to the surface. The test results gave the friction coefficient μ .

The values of the lubrication parameter f given for each material were determined from the results of tests performed with C.B.N. wedges of various angles α , under the same lubrication conditions as for the cylinder tests. This method was chosen because, as has already been mentioned in chapter (1), several authors [50, 51, 15, 16] checked that Challen and Oxley's wave model

for a wedge shaped asperity [2] successfully predicted measured friction coefficients when a hard wedge slides on some non-ferrous materials. The results of these tests are presented in appendix (H).

A value of $f = 0.05$ was determined this way for both materials.

5.2 The visualisation investigation

5.2.1 Principles of the visualisation technique

Friction coefficient interpretations have been mostly experimentally performed through static postmortem observations of the friction tracks and/or the sub-surface microstructural changes in the two contacting bodies. When two bodies slide relatively to each other, the velocity discontinuity induces damage in these first bodies, leading to the detachment of particles. These particles constitute an interface or third body. If they are trapped inside the contact, they will contribute to some extent to the velocity accommodation and thus to frictional energy dissipation. Friction will depend on the respective contribution of the velocity accommodation sites and processes : third body shearing? detachment of particles from the first bodies?..... If the main site of velocity accommodation is the third body, friction will depend directly on the flows and rheology of particles inside the contact area [12, 9]. The visualisation technique through a transparent tool allows a dynamic observation of these particle flows and rheology [94], [73]. It assists the understanding and reconstitution of the life of a contact, reducing the role of the imagination in friction interpretation. For example, Descartes [95], [10] used this technique to study solid lubrication with a MoSx coating. The author developed a method of understanding the tribological behavior of the MoSx, based on third body flows and rheology and their consequences on friction. The visualisation technique associated with static observations on both visualisation and blind tests allowed the dynamic reconstitution of the tribological behaviour of the MoSx and allowed

the identification of the significant parameters, mechanisms or scales influencing friction. Such an approach has been undertaken in the present work to investigate the relative contribution of large scale deformation of the wearing surface (aluminium alloy) and of the third body flows (detached particles of aluminium alloy) on friction.

Some conceptual tools are needed to describe the dynamic observations made during the visualisation test of the present work. The particle flows which can be activated in the contact are of different origin and can be schematised in figure (5.6). They will be used in the following descriptions and can be defined as follows:

1. Q_s : the source flow. This flow is associated with the detachment of particles and constitutes a “natural” source of third body.
2. Q_i : the internal flow. This flow corresponds to the particles trapped inside the contact and which flow between the two first bodies.
3. Q_r : the recirculation flow. It is constituted by the particles which are driven by one of the first bodies outside of the contact area and are then drawn back into the contact area.
4. Q_w : the wear. These particles are ejected from the contact and do not participate again in the velocity accommodation between the contacting bodies.

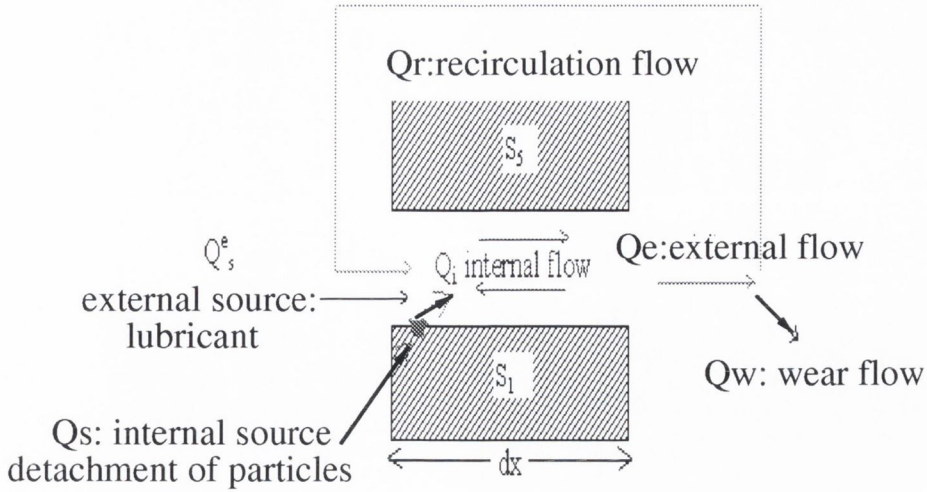


Figure 5.6: Tribological circuit. Taken from [9]

5.2.2 Objectives for the present work

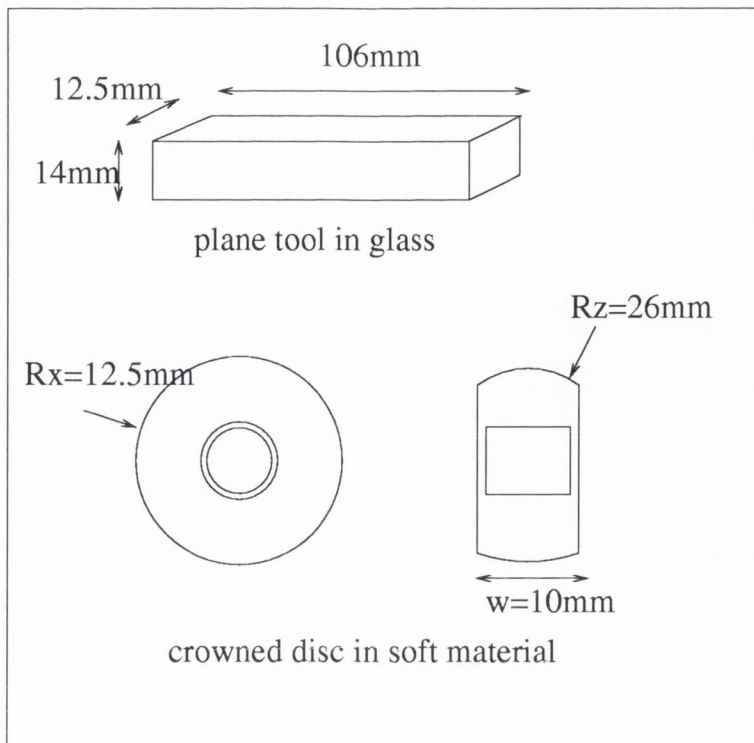
The objectives of the second part of the experimental work were to:

1. use a transparent tool wearing the soft surface, and visualise the detached particle flows at the interface through the transparent tool.
2. preserve the tool and test sample for further examination and obtain a static view of the associated dynamic observations previously made.

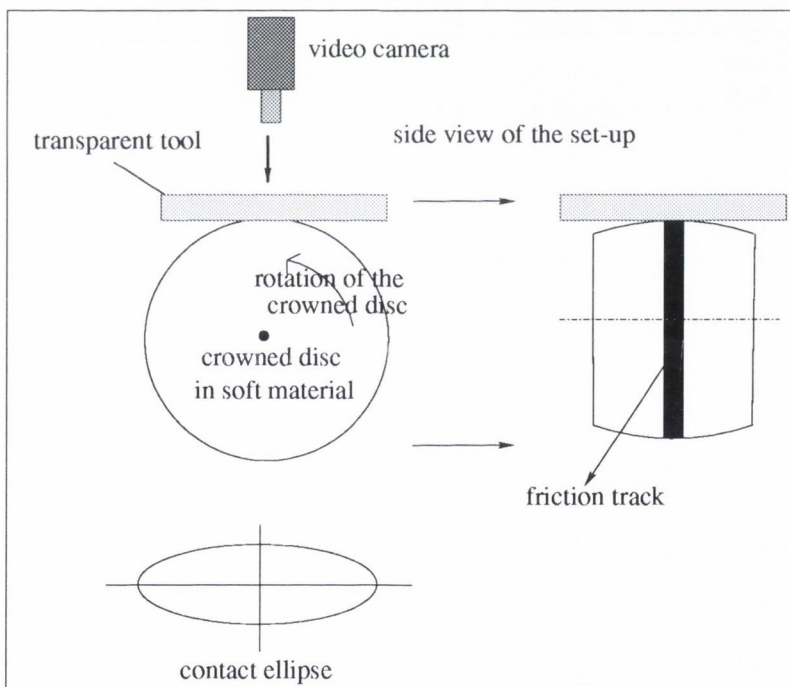
5.2.3 Experimental set-up

MATERIALS AND GEOMETRY

The materials were the same metals as in section (5.1.2). The test pieces were shaped as crowned discs, as shown in figure (5.7). This specimen shape leads to an elliptical contact area as shown in figure (5.7b). For geometrical and optical reasons, these conditions give good pictures of the contact. The tools used were made of glass ($E=63\text{GPa}$, $\sigma_y = 500\text{MPa}$).



a: geometry of the contacting bodies



b: geometry of the contact for the visualisation tests

Figure 5.7: Geometry of the contact for the visualisation tests

EXPERIMENTAL APPARATUS

The test rig used in these tests, called PEDEBA and developed in the L.M.C. is shown in figures (5.8a) and (5.8b) and is schematised in figure (5.9). This set-up is divided into two subsets:

1. the horizontal subset with the transparent tool. It is linked to a servo hydraulic jack. This can impose a controlled tangential displacement over time. For the present tests, the transparent tool was held fixed.
2. the vertical subset with the crowned disc. It is linked to a hydraulic jack that imposes the normal load between the two test pieces. A small motor was attached the disc to rotate it [Its characteristics: D.C. 50W at 60rev/min (output from 82.5/1 reduction gearbox), max torque 3.5Nm]. A dynamometer gives the values of normal and tangential loads.

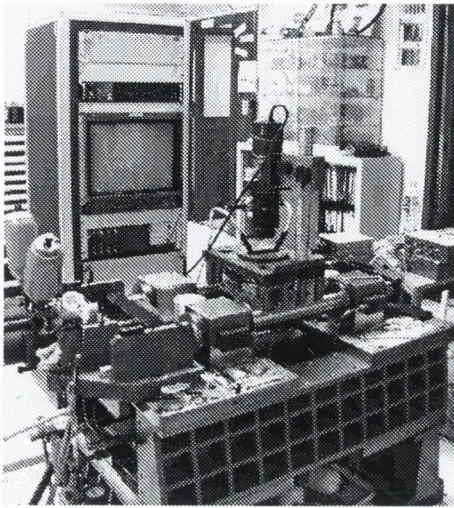
The test rig is very stiff. Basically, the set-up allows the plane transparent tool in glass, held fixed to be loaded against the periphery of a rotating crowned disc in aluminium alloy or copper.

Sensors allow tangential and normal forces and also normal displacements to be measured during the test.

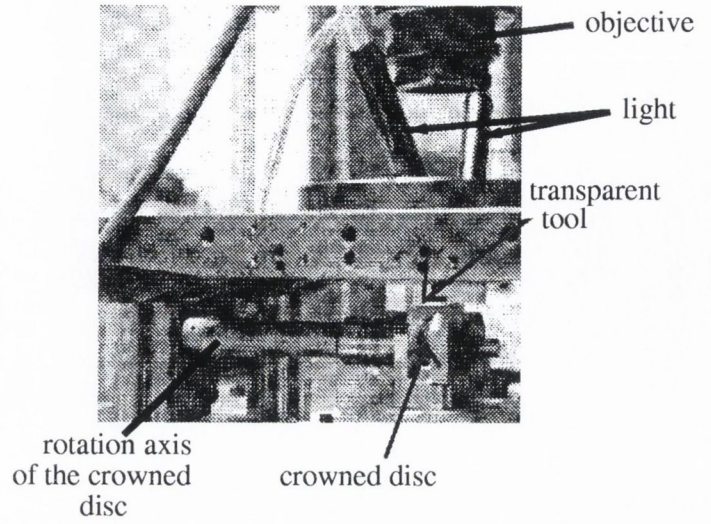
The visualisation equipment is composed of:

1. a variable magnification objective
2. a video camera
3. a video recorder
4. a monitor

To give an idea of the magnification obtained, the friction track can be visualised full screen on the monitor.



a: general view



b: transparent tool and crowned disc

Figure 5.8: Photographs of the PEDEBA rig.

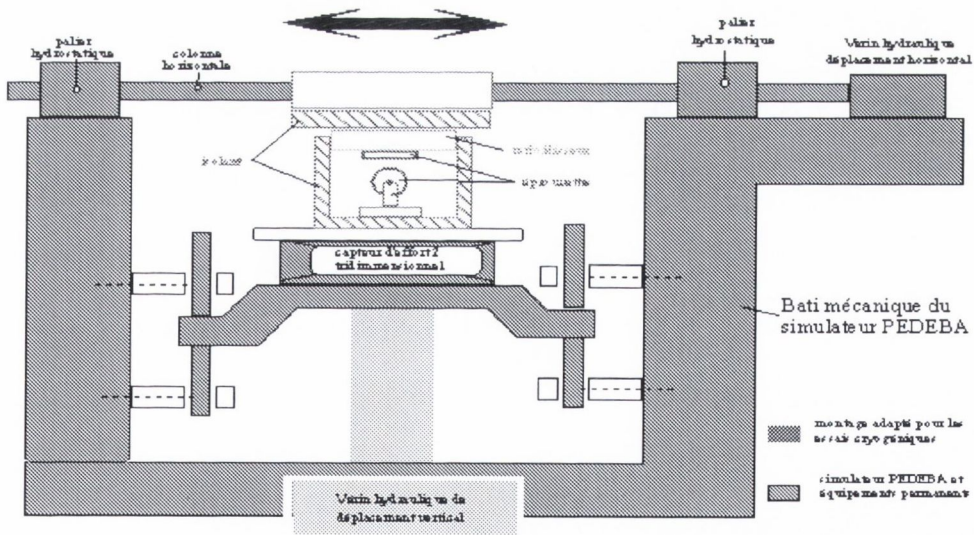


Figure 5.9: PEDEBA rig. Taken from [10]

5.2.4 Experimental procedure

Before each test, the disc was polished down to a value of $Ra = 0.1\mu\text{m}$ and cleaned with acetate. Lubrication was provided by 1% stearic acid in white medicinal oil as in the tests of section (5.1). The oil was deposited on the surface of the crowned disc with a cotton bud (volume of lubricant $< 2\mu\text{l}$). The disc was then mounted on the rig. The normal load was applied statically. The initial static hertzian contact area was elliptical. The video camera was focused onto the contact area, which could be seen directly on the television during the test. The crowned disc was then set in rotation. During the test, the normal load was controlled and both normal and frictional loads were registered. For each test, a video was taped for further analysis. At the end of a test, rotation was stopped and the set-up was then unloaded.

After each test, the transparent tool and the crowned disc were carefully dismantled and kept uncleaned for further observations with optical and electron microscopy.

The general test procedure is sketched in figures (5.10) and (5.11).

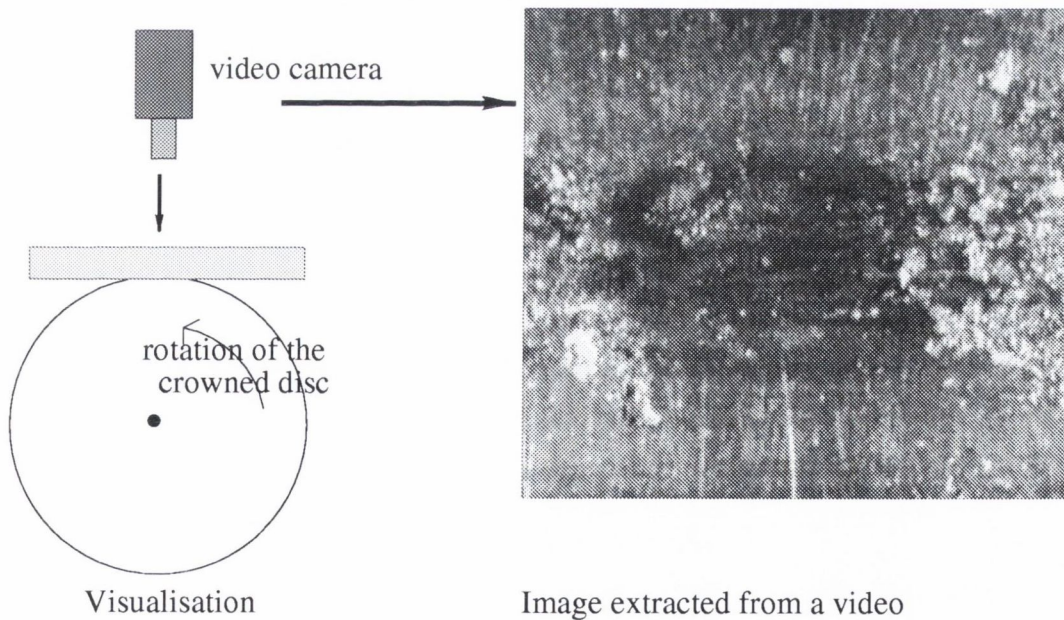


Figure 5.10: Dynamic observations

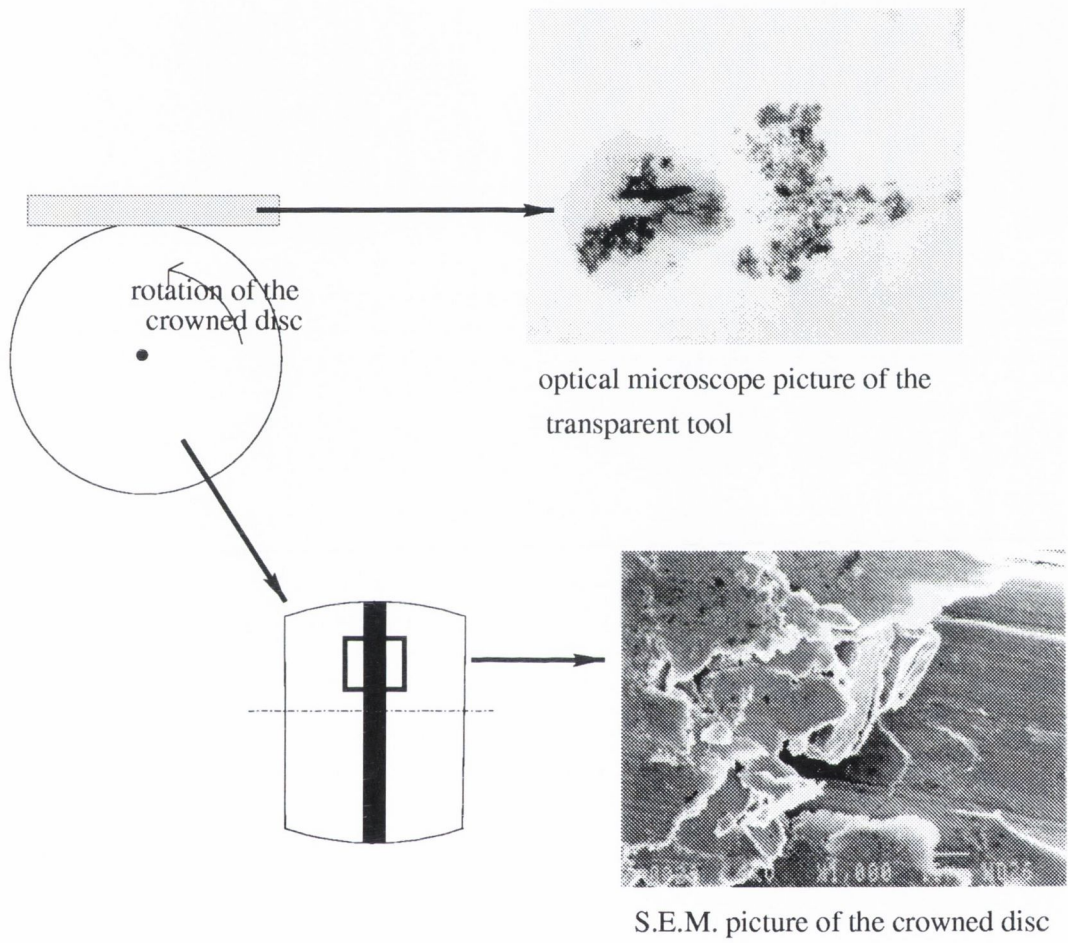


Figure 5.11: Static post-mortem observations

5.2.5 Test conditions

A series of tests was carried out to fulfil the visualisation objectives. In this thesis, one test for each material has been selected. Figure (5.12) presents the conditions for these two visualisation tests.

The applied load was low (see figure (5.12)), this limitation being imposed by the mechanical properties of the glass ($\sigma_y = 500MPa$). Above these loads, glass was often observed to crack.

The initial roughness of $0.5\mu m$ of the disc led to the formation of a thick lubricant layer and no particles were created under these conditions. For this reason, the disc was polished down to a value of $0.1\mu m$.

	GEOMETRY	MATERIALS	LOADING CONDITIONS	LUBRIFICATION	SLIDING VELOCITY in m/s	Ra in μm
VISUALISATION TESTS	plane	Glass	W=25N	(boundary lubrication) with 1% stearic acid in white oil (applied on the disc with a cotton bud)	0.01	<0.1
	ellipsoide Rx=12.5mm Rz=25mm	aluminium alloy or Copper	Pmax(Hertz) =286 MPa Pmax(Hertz) =300 MPa			

Figure 5.12: Test conditions

Chapter 6

Experimental results

This chapter presents the results of the two parts of the experimental investigation:

1. In a first part, the friction tests with the use of a full cylinder and a cut cylinder are described for both materials. The observations of detached particles accumulated around the contact area are presented. The friction results are compared with our numerical model.

The tests performed with a full cylinder will be called blind tests (because what happens at the interface can not be seen) in order to distinguish them from the visualisation tests.

2. The aim of the second part of the experimental investigation is to investigate the behaviour of the detached particles accumulated around the contact area for the full cylinder tests or blind tests.

In this section, the results of the visualisation tests are presented for both materials: the dynamic observations of the particle flows at the interface are correlated to the static observations of the friction track after the test. These results are used to determine whether the detached particles are trapped inside the contact area and flow at the interface for the blind tests.

6.1 Friction results and observations when a hard cylinder in C.B.N. slides across two non-ferrous metals

Details concerning friction measurements and experimental data are given in appendix (K).

6.1.1 Full cylinder tests: S_1

General observations during the tests. Observations of the tool

In the load range of these tests, wear rates were clearly observed to increase with load for both materials. For the highest loads, it was thus more easily observable that a significant number of particles accumulated, especially in front of the tool but also at the sides and even slightly behind it. It should be noted that the presence of the lubricating sponge, (see chapter (5)), limited this particle accumulation to some extent, acting as a filter.

Figures (6.1) and (6.2) show how the detached particles lie on the cylinder after a test on aluminium and copper respectively. For both figures, the entry of the contact is on the left. Even if it is possible that some particles have been driven into the contact area during the unloading procedure, due to progressive decrease of contact pressure, it seems probable that particles are present inside the contact area.

The detached particles observed in figures (6.1) and (6.2) have been checked to be aluminium and copper respectively by x-ray analysis. However, for copper, oxides were found too.

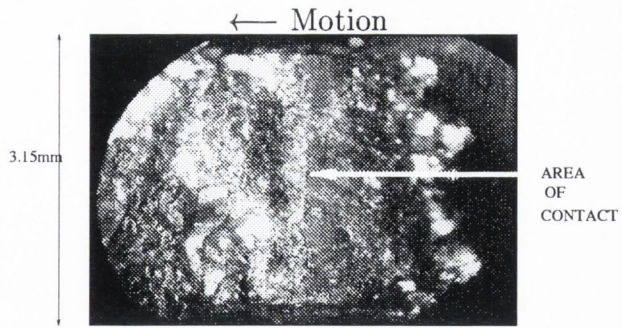


Figure 6.1: Detached particle accumulation for the full cylinder experiment for aluminium - Top view of the cylinder - $N/kR=0.5$ - Width of the tool=3.15mm

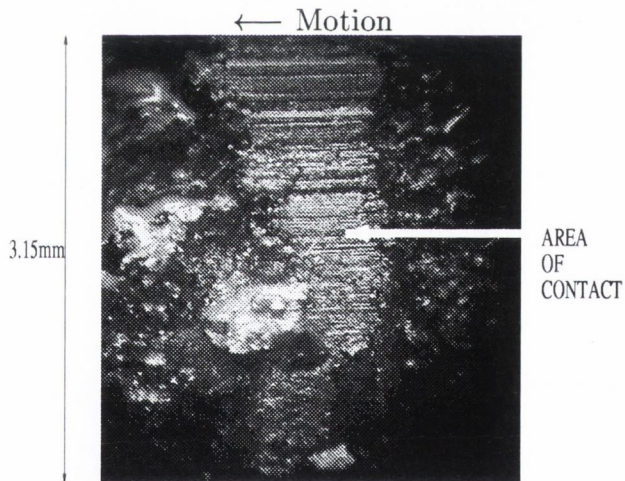


Figure 6.2: Detached particle accumulation for the full cylinder experiment for copper - Top view of the tool - $N/kR=0.5$ - Width of the tool=3.15mm

Friction results

The friction results of the sets S_{1al} and S_{1co} , where a full cylinder in C.B.N. slides across aluminium and copper, are presented in figures (6.3) and (6.4) respectively. The circles represent the measured friction coefficients. The stars represent the predictions of the plastic model developed in the present work, while the full lines represent the predictions of the chord model [1]. For both models, a value of $f = 0.05$ has been taken (the determination of f has been described in appendix (H)). It can be seen that for both materials the experimental values are higher than those predicted by both models.

For aluminium, (see figure (6.3)), increasing load does not imply increasing μ as predicted by slipline field theory. The measured friction coefficients are roughly constant over the load range of the tests, with $\mu = 0.1$.

However, for copper (see figure (6.4)), the measured friction coefficients do show some increase with load. In figure (6.4), the dotted lines represent the predictions of the plastic model developed in the present work for $f = 0.3$. It can be seen that measured friction coefficients fit the predictions of the model reasonably well when the boundary conditions of the interface are changed.

Large scatter in the experimental results for a given load can be observed for both materials. This can be explained firstly by the practical difficulty of positioning the cylinder so that it contacts the bar at its highest point and some differences in alignment are possible between two different tests. This could also be due to the presence of a fairly thick layer of particles at the interface between the cylinder and the soft material, as was observed in previous section. The features and behaviour of the layer might change from one test to another (slight change in lubricant volume, nature of the paste inside the contact area ...), which probably changes the test conditions. Finally, this could be explained also by the scatter observed, for a given test, in the measured frictional and normal forces, as shown in appendix (K).

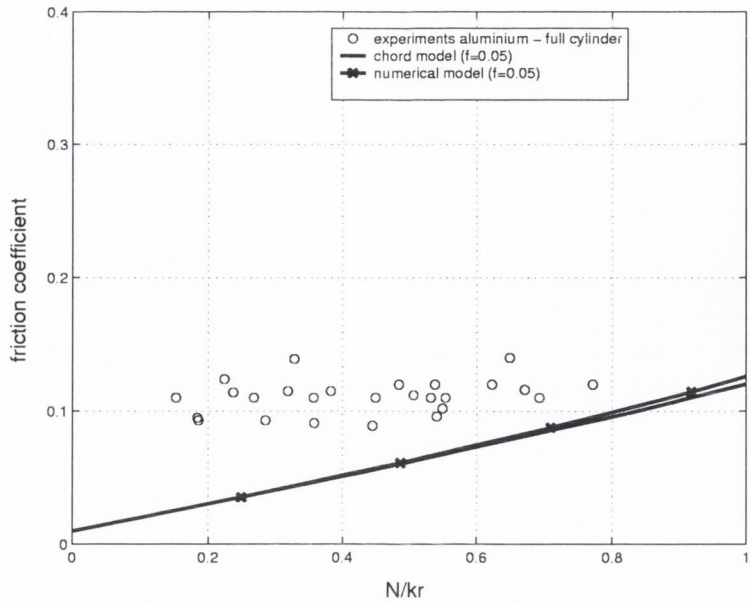


Figure 6.3: Experiments with full cylinders. Aluminium

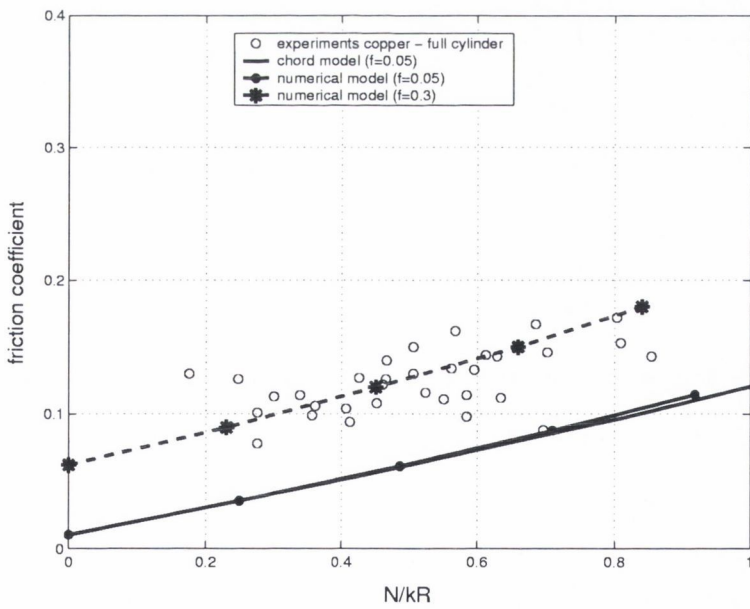


Figure 6.4: Experiments with full cylinders. Copper

6.1.2 Cut cylinder tests: S_2

General observations during the tests- Observations of the tool

Over the load range of these tests, wear rates were observed to be much higher than found in the tests with the full cylinders for the same sliding distance. They also clearly increase with load. Figures (6.5) and (6.6) show the detached particle organisation on the tool after tests on aluminium and copper respectively. For both pictures, the entry of the contact is on the left. These pictures show that particles are also present inside the contact area. However, it can be observed that there is much less accumulation of particles at the exit of the contact (right of both pictures) than with the full cylinder, which is a consequence of the removal of the trailing edge.

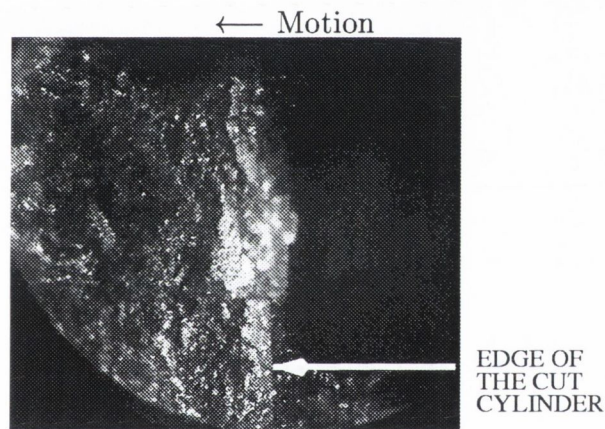


Figure 6.5: Detached particle accumulation for the cut cylinder experiments on aluminium - Top view of the tool - $N/kR=0.25$ - width of the tool=3.15mm

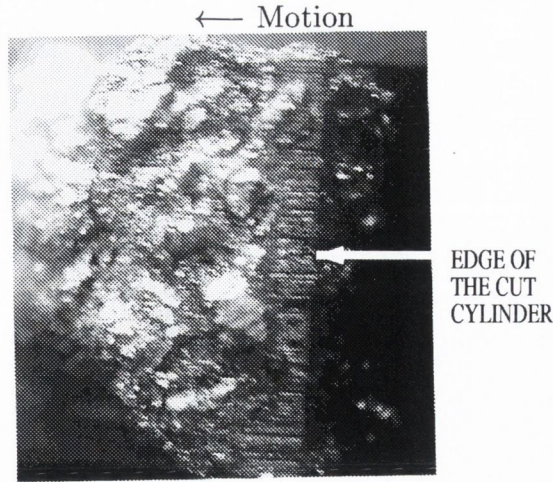


Figure 6.6: Detached particle accumulation for the cut cylinder experiments on copper—Top view of the tool— $N/kR=0.52$ - Width of the tool=3.15mm

Friction results

The friction results of sets S_{2al} and S_{2co} , where a cut cylinder in C.B.N. slides across aluminium and copper respectively, are presented in figures (6.7) and (6.8) for the two materials. The triangles represent the measured friction coefficients, while the dotted lines represent the predictions of the developed chord model [3] (equations in appendix (B)) for $f = 0.05$. For each graph, the value chosen for β_c , the angle between the leading edge and the center line of the cylinder, is the one which best fits the experimental data.

It can be seen that the friction coefficients are generally higher than with the full cylinder (see section (6.1.1)) and that they increase with load as predicted by the developed chord model. The deviations from the developed chord model observed for the highest loads were associated with a change of deformation regime. Under these loading conditions, continuous removal of material, or rough cutting was observed. However, under less severe conditions, measured friction coefficients for aluminium fit the developed chord model predictions well.

There is still large scatter in the experimental results for a given load and

for both materials, probably because of the presence of a layer of particles at the interface, whose features and behaviour might change from one test to another. This could be explained also by the scatter observed, for a given test, in the measured frictional and normal forces, as shown in appendix (K). However, friction coefficients follow the trend of slipline field theory.

As mentioned in chapter (5), the same tool was used for both materials. Nevertheless, the angle β_c which best fits the data is 8.5° for aluminium and 5° for copper. Unfortunately, the lack of accuracy in grinding this tool and the practical difficulties of accurately measuring β_c on the tool did not allow an accurate independent determination of the actual β_c . The different angles obtained can be explained to some extent by the rotation of the tool around its pivot with progressive wear of the test-piece (set-up described in chapter (5)). Copper and aluminium have different wear rates; thus the resulting average β_c might differ.

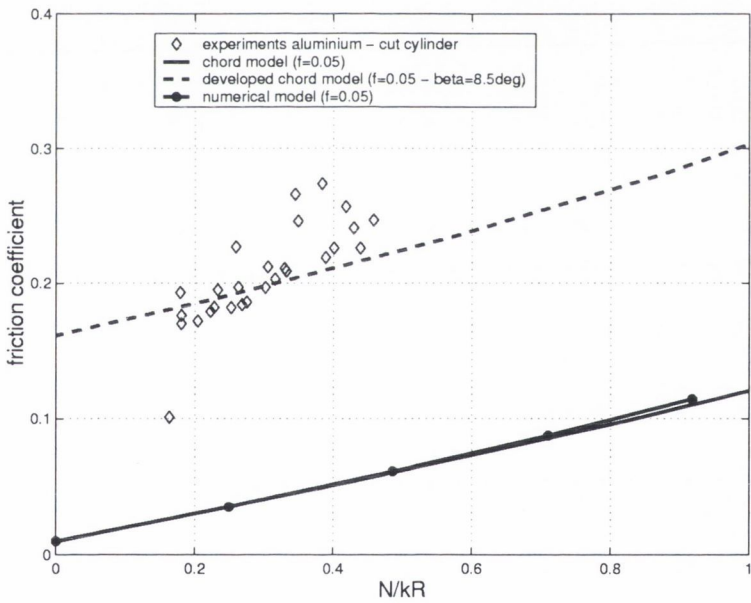


Figure 6.7: Experiments with a cut cylinder: Aluminium

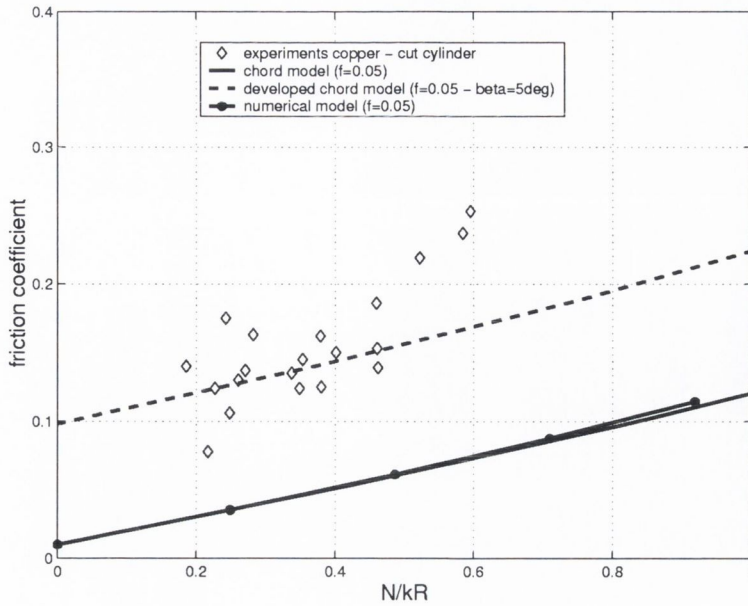


Figure 6.8: Experiments with a cut cylinder: Copper

6.2 Results of the visualisation investigation

6.2.1 Introduction: objectives and method

The aim of the visualisation investigation was to investigate the behaviour of the detached particles when a cylinder in C.B.N. slides across the two non-ferrous materials tested, and especially to answer the following questions:

- Are the particles trapped in the contact?
- Do they participate in the velocity accommodation between the cylinder and the soft material?

The method used to achieve these objectives consists of:

1. Using a transparent tool wearing the soft surface and visualising the detached particle flows at the interface through the transparent tool.
2. Preserving the tool and the test sample for further examination and obtaining a static view of the surfaces at the end of the test.

3. Starting from static observations of the samples involved in the blind tests when a full cylinder slides across the soft surface and reconstituting what happens dynamically at the interface.

The visualisation tests are used as an aid in the reconstitution of the activated flows of detached particles involved in the blind tests. However some care has to be taken in the correlation with the blind tests because, as described in chapter (5), the contacts are different. The obvious differences can be stated as follows:

1. The geometry and the loading conditions.
2. The material (glass instead of C.B.N.).
3. The physical-chemistry (The triplet aluminium (or copper)/glass/stearic acid instead of the triplet aluminium (or copper)/glass/stearic acid).

Glass has mechanical, thermo-mechanical and physico-chemical properties different from C.B.N. This could modify the behaviour in friction. This is the reason why no friction results are presented for the visualisation tests.

4. The surface preparation.

All these parameters influence the contact life and the differences have to be accounted for. For example, the mechanisms involved in the detachment of particles are not necessarily the same for the two sets of tests.

In the following sections, the visualisation analysis is described for both materials. Some additional blind tests (tests with a C.B.N. cylinder) were performed on the initial test rig and attention has been focussed on observation of detached particles collected on the tool and compared with the visualisation tests.

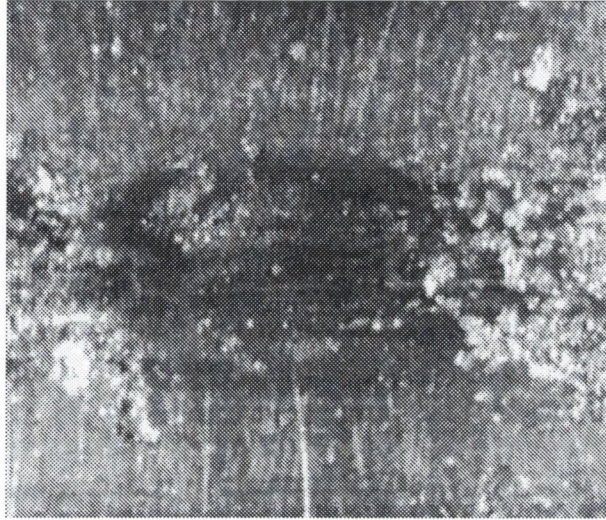
6.2.2 Results for aluminium

RESULTS OF THE VISUALISATION TESTS: CORRELATION BETWEEN DYNAMIC AND STATIC OBSERVATIONS

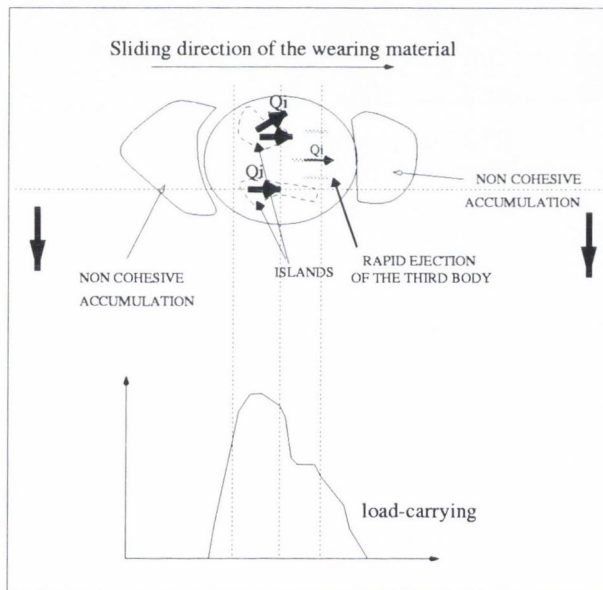
Dynamic observations

Figure (6.9a) shows a picture taken from the video in the last stages of the test on aluminium. The conditions for this test have been given in chapter (5). Here, only the end of the test is described because the dynamic observations made during the last cycles of the test will be directly associated with what remains statically on the specimen after the test. Once enough aluminium particles have been created, the contact reaches a sort of steady state: the contact area remains constant and the particle flows are regular. The activated flows of detached particles involved in figure (6.9a) have been sketched in figure (6.9b). Basically, there is a mass of non cohesive particles which accumulates at the entry of the contact area, which is on the left of the two figures. These particles are provided by the recirculation flow, or Q_r , which is made up of the particles which are driven by the rotating crowned disc outside of the contact area and are then drawn back into the contact area (see chapter (1)). Then, the particles are driven periodically into the contact area as cohesive groups, or load-carrying islands. These flows constitute the internal flow, or Q_i , which corresponds to the particles trapped inside the contact and which flow between the two first bodies and carry the load. This mixture of solid particles and lubricant seems to have the rheological behavior of a “very viscous paste”. Lateral or longitudinal internal flows of particles can be observed, as shown in figure (6.9b) with the direction of the arrows Q_i .

← Motion



a: At 96% of the test duration



b: schematics of the activated flows

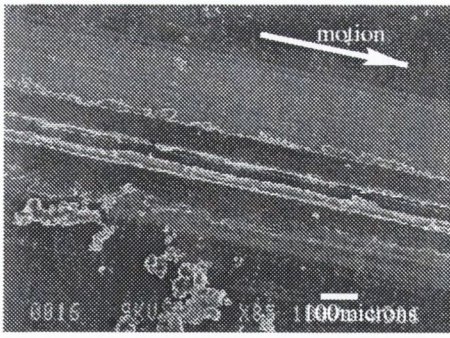
Figure 6.9: Image extracted from a video- Visualisation test on aluminium-
N=25N- Average width of the friction track $\simeq 0.7\text{mm}$ - velocity $\simeq 10\text{rev/min}$.

Post-mortem static observations

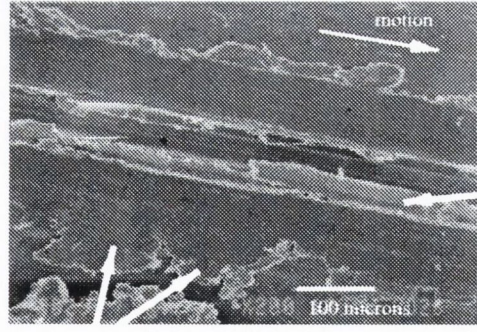
Figures (6.10a) and (6.10b) are SEM pictures of the friction track on the crowned disc in aluminum after the visualisation test. The instantaneous surfaces observed dynamically in the previous section can be seen on this friction track. Longitudinal smooth areas (or platelets) can be associated with longitudinal internal flows (which correspond to the longitudinal flows of the islands in figure (6.9b)). The smooth laterally oriented areas (or flakes) can be associated with the lateral internal flows.

Observations at higher magnification in figure (6.10c) show that the third body is sheared along different planes. This has been sketched in figure (6.10d). This is also called the S3M3 mechanism, with S3, or site 3 for third body and M3, or mechanism 3 for shearing (see appendix (I) and references [96], [9]). This suggests that the third body separates completely the two first bodies and that the source flow (which corresponds to the detachment of particles) is much reduced once a sufficient quantity has been created to ensure the velocity accommodation. The recirculation flow, as has been observed dynamically would be the main activated flow in the contact under these conditions.

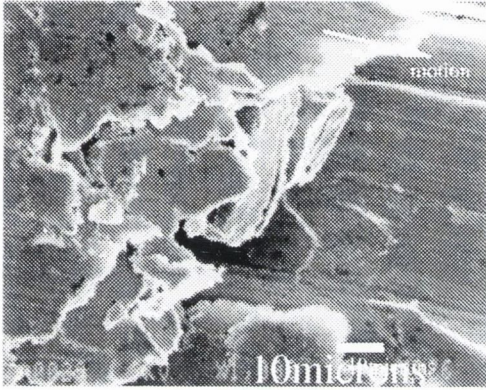
Figures (6.11a) and (6.11b) show how the detached particles lie on the transparent tool after the test. There is a long smooth particle in figure (6.11b), which is the static view of a longitudinal flow observed on the video just before the test stops. This is probably a "layer" of an S3M3 type mechanism which remains on the glass. This is clearly quite cohesive and will probably lead to one long surface on the disc track shown on the pictures (6.10a) and (6.10b), once driven into the contact.



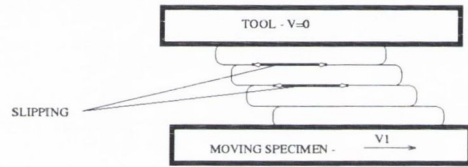
a:



b:

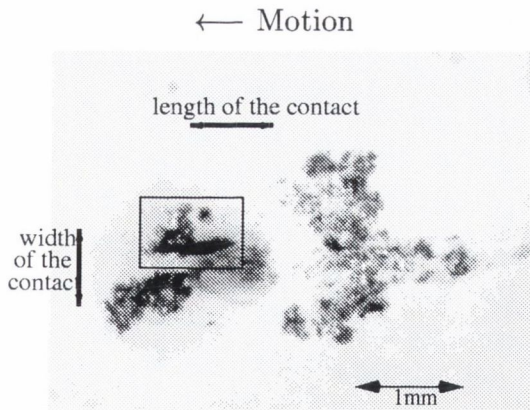


c:

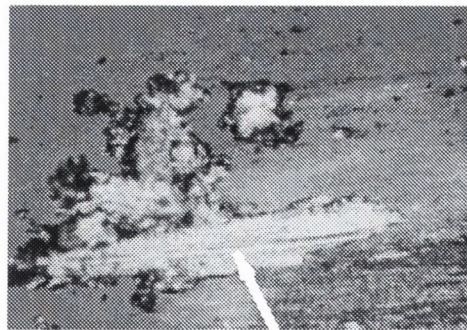


d: S3M3 type of velocity accommodations

Figure 6.10: SEM images of the friction track of the crowned disc after the visualisation test on aluminium (see test conditions in figure (5.12))



a:



b:

Figure 6.11: Optical microscope images of the transparent tool after the visualisation test on aluminium - (a) overview of the contact - (b) zoom of (a)

CORRELATION BETWEEN THE VISUALISATION TEST AND THE BLIND TESTS FOR ALUMINIUM

Figures (6.12a) and (6.12b) show the detached particle organisation on the tool after the blind test (b) and the visualisation test (a) respectively. For both pictures, the entry of the contact is on the left. There is a similar organisation in front of and behind the contact of non cohesive particles.

Figures (6.13b) and (6.13c) show a conglomerate of particles collected after the blind test on the cylinder close to the contact area. Figure (6.13a) shows the friction track after the visualisation test. The comparison of the particle morphology and organisation suggests a similar S3M3 mechanism in the two types of test. However, as shown in figures (6.13b and c), the conglomerates collected after the blind test are quite thick and have almost the same width as the contact area. For the blind test configuration, it is probable that the main direction of particle flow is the sliding direction. Lateral flows, as were observed in the visualisation test probably do not occur here. This can be explained by the fact that, in the blind test, material is constrained in plane strain flow, thus limiting particle side leakage, whereas the contact in the visualisation test is more open and lateral particle flows are possible.

6.2.3 Results for copper

RESULTS OF THE VISUALISATION TESTS: CORRELATION BETWEEN DYNAMIC AND STATIC OBSERVATIONS

Dynamic observations

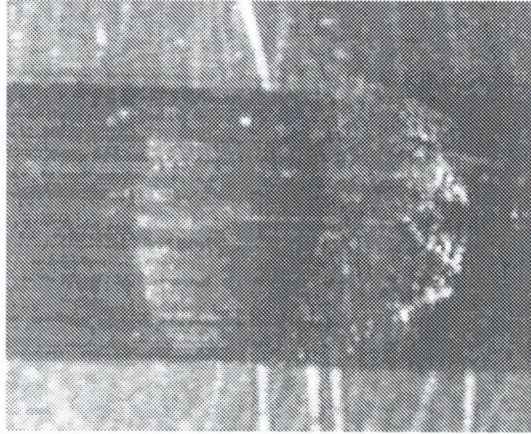
Figure (6.14a) shows a picture taken from the video at 50% of the test duration on copper. The conditions for this test have been given in chapter (5). No quality pictures describing the last stages of the test are available because of visualisation problems (brightness of copper, small number of particles involved, set-up not perfectly stiff for this test, ...). However, the particle flows described here do not evolve much during the last stages of the test and can thus be associated with static observations performed after the test.

As for aluminium, once enough copper particles have been created during the test, the contact reaches a sort of steady state: the particle flows are regular. The activated flows of detached particles involved in figure (6.14a) have been sketched in figure (6.14b). Basically, a regular delocalisation of the load-carrying is observed. As a first step, there is a small number of cohesive particles which accumulates at the entry of the contact. This area grows slowly up to a given quantity of particles, at which point it seems to carry all the load. This load-carrying area then moves forward to the center of the contact and then to the exit. Instantaneous long, thin surfaces are periodically observed in the contact area. This hour-glass process then starts again at the entry of the contact. Most of the observed flows are composed of individual non-cohesive particles or very thin lines of particles. Large cohesive islands, observed in the test on aluminium have not been observed here. Copper may be more reactive with stearic acid than aluminium, leading to metallic soap formation and less auto-adhesion between its particles [65].

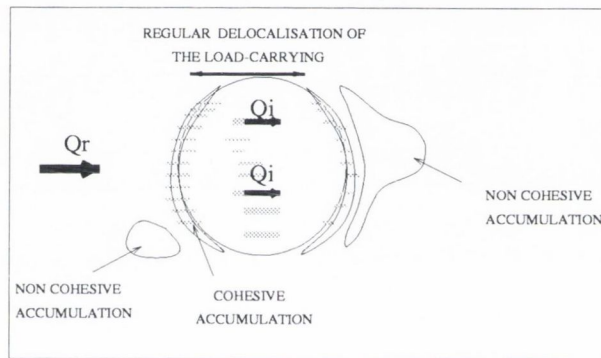
It should be noted that the set-up was not perfectly stiff for this test (we realised that one part of the specimen holder was free to move during this test); this could have led to a reduction in the contact pressure, and increase

in contact vibration. This could explain to some extent why there are fewer particles created for copper than for aluminium.

← Motion



a: movie copper



b: schematics of the activated flows

Figure 6.14: Image extracted from a video- Visualisation test on copper-
 $N \approx 25\text{N}$ around- Average width of the friction track $\sim 1.5\text{mm}$ - velocity
 $\sim 10\text{rev/min}$

Static post-mortem observations

Figures (6.15a), (6.15b), (6.16a) and (6.16b) are SEM pictures of the friction track on the crowned disc in copper after the visualisation test. The instantaneous long thin surfaces observed dynamically in the previous section can be observed at different magnification.

Observations at very high magnification in figure (6.16b) show that the particles created are very small ($< 10\mu\text{m}$). Figures (6.15b) and (6.16a) show that these individual particles can eventually form more cohesive planes under a S3M3 mechanism, as was sketched in figure (6.10d).

Figure (6.17) shows how the detached particles lie on the transparent tool after the test. There are long thin particle lines, which are the static view of the longitudinal flows observed on the video during the test.

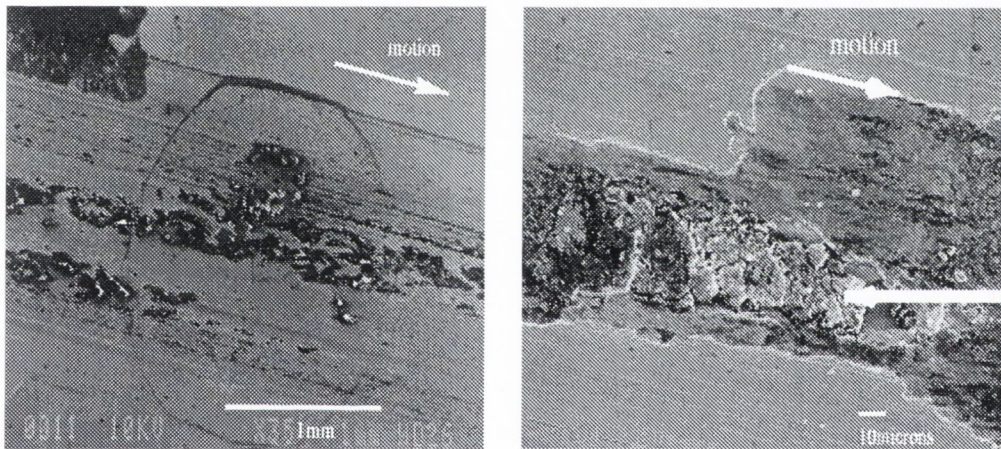


Figure 6.15: SEM images of the friction track of the crowned disc after the visualisation test on copper

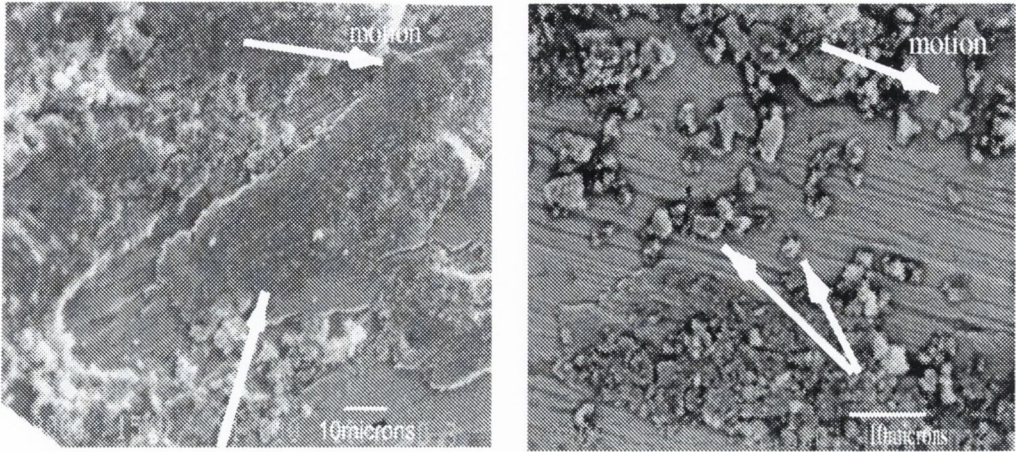


Figure 6.16: SEM images of the friction track of the crowned disc after the visualisation test on copper

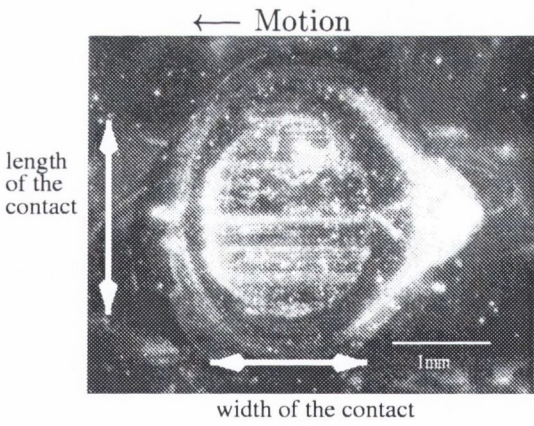


Figure 6.17: Optical microscope image of the transparent tool - copper

CORRELATION BETWEEN THE VISUALISATION TEST AND THE BLIND TESTS FOR COPPER

Figures (6.18a) and (6.18b) show the detached particle organisation on the tool after the visualisation test (a) and after the blind test (b) respectively. For both pictures, the entry of the contact is on the left. There is a similar organisation in front of and behind the contact of non cohesive particles.

Figures (6.19c) and (6.19d) show a conglomerate of particles collected after the blind test on the cylinder close to the contact area. Figures (6.19a) and (6.19b) show the friction track after the visualisation test. A comparison of the particle morphology and organisation suggests a similar S3M3 mechanism in the two types of test. However, figure (6.19d) shows that, even if the conglomerate is compacted and forms an homogeneous layer, it can be observed that the layer is composed of very thin longitudinal layers, which appear to be less cohesive than the layer found with aluminium. This last feature is consistent with the observations of the visualisation, where no real cohesion between the particles was observed. As for aluminium, velocity accommodation sites are more localised in the visualisation test than in the blind test, where material is constrained to plane strain flow.

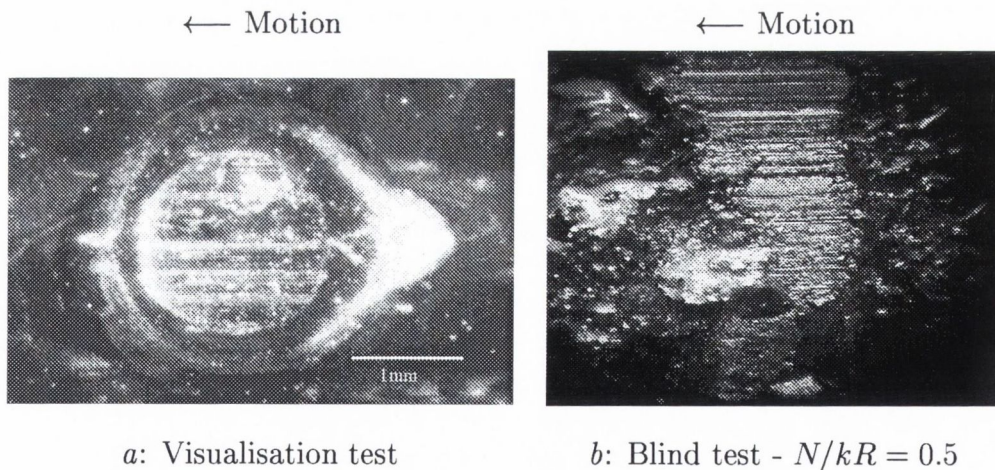
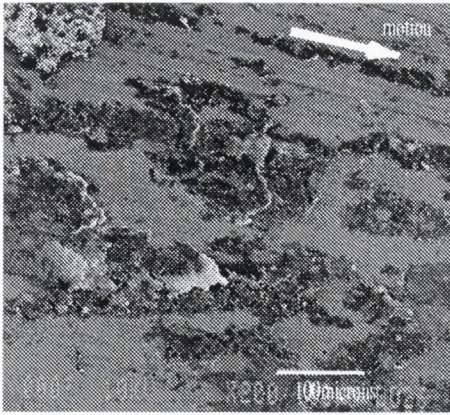
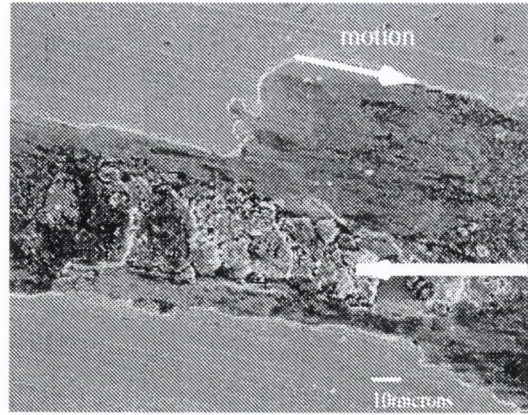


Figure 6.18: Detached particle organisation on the cylinder after the blind test and on the transparent tool after the visualisation test for copper



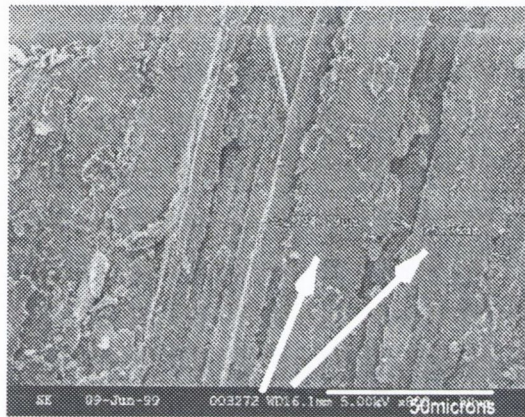
a: visualisation test



b: visualisation test



c: blind test - $N/kr=0.43$



d: blind test - $N/kr=0.43$

Figure 6.19: S3M3 sites for the visualisation test and for the blind test (full cylinder)—Copper

6.3 Conclusions

6.3.1 Friction results

The friction results obtained in section (6.1) show that:

- Measured friction coefficients are higher than the predictions of our numerical model when a cylinder in C.B.N. slides across the two non-ferrous metals under investigation.

- For aluminium, measured friction coefficients are roughly constant, which is not consistent with slipline field predictions, where friction is supposed to increase with load.
- The behaviour of copper, however, is closer to a rigid perfectly plastic behaviour. The friction results exhibit some increase with load. By changing the value of the Tresca factor at the interface, these results follow the trends of slipline field theory well.
- When the trailing edge of the cylinder is relieved, measured friction coefficients for both materials follow the predictions of slipline field theory well.

6.3.2 Visualisation results

The tests with a full cylinder have been correlated to the visualisation tests. Some similarities in the static observations (particle organisation, conglomerate morphology, ...) provide some experimental evidence that identical mechanisms of velocity accommodation operate in both tests and for both materials. The particle conglomerates observed in the blind tests, probably participate at least partly in velocity accommodation by carrying load and by being sheared along planes.

This suggests that for both materials:

- A significant layer of a mixture of solid particles and lubricant is trapped inside the contact area. The distribution of this paste all over the contact area might modify the overall geometry of the contact, and thus the pressure distribution on the wearing material.
- This mixture solid particles/lubricant flows in the contact area. The position and the size of the contact areas might thus evolve during the contact life, as does the pressure distribution.

Chapter 7

Discussion

7.1 Friction

7.1.1 Introduction

In chapter (6), two non-ferrous metals, with different modulus to strength ratio (E/σ_y) have been tested against the predictions of our numerical model.

For the full cylinder configuration, significant deviations from theory have been observed for both materials, which however exhibit a different behaviour.

For the cut cylinder configuration, measured friction coefficients for both materials were found to follow slipline field theory more closely.

Furthermore, the visualisation investigation provided some experimental evidence that a significant layer of a mixture of solid particles and lubricant is trapped in the contact for the two materials and flows in the contact area.

This section is composed of three parts:

- In a first part, the influence of elastic effects on friction for the full and cut cylinder configurations is investigated. Firstly, the main results of the finite element analysis are recalled. Secondly, the predictions of the elasto-plastic model of Torrance et al [8, 63, 64], which accounts

approximately for elasticity when a wedge shape asperity slides across a softer surface are compared to our numerical model too.

- In a second part, the influence on friction of a third body layer at the interface, as observed in the experiments is discussed for the full cylinder and cut cylinder configuration. The consequences of these effects on the two parameters θ and f which are the inputs of our numerical model are analysed.
- Finally, our experimental results for the full cylinder and cut cylinder configuration and for the two tested materials are discussed in terms of these effects.

7.1.2 Influence of elastic effects

Finite element analysis

Finite element analysis (see chapter (4)) shows that for the full cylinder configuration, elastic effects induce the formation of a trailing wave behind the center line of the cylinder in the soft surface. When no friction is considered at the interface (i.e. $f = 0$ as in finite element analysis), friction coefficients are predicted to increase with load as predicted by our numerical model but to be lower.

When a cut cylinder is considered, finite element analysis shows that the trailing wave is removed and elastic effects are thus decreased. When no friction is considered at the interface, friction coefficients are closer to our numerical model.

Comparison of our numerical model with the elasto-plastic model of Torrance et al [8, 63, 64]

By using finite element analysis, Torrance et al [31, 29, 8] have estimated that for typical engineering materials for which the ratio of modulus to strength lies in the range of $100 < E/\sigma_y < 400$ and for topographies within which the effective surface slopes α are in the range 1° - 5° , the wave model [2] breaks down. Torrance et al [8, 63, 64] proposed an elasto-plastic model, which is the extension of the wave model [2] to smoother surfaces with lower slopes. The authors showed that when elastic effects are considered in conjunction with a Tresca factor for a wedge shaped asperity, the normal and tangential stresses begin to deviate significantly from those given by slipline field theory for the lowest angles.

Using this model in conjunction with a Tresca factor f , the friction coefficient is defined as follows:

$$\mu = \tan(\alpha + \theta_f) \quad (7.1)$$

where,

$$\theta_f = \arctan\left(f \frac{k_s}{P}\right) \quad (7.2)$$

where P is the mean contact pressure on the front face of the wedge calculated by the model.

In figure (7.1), The friction predictions of this model (dashed lines) are compared to our numerical model (stars) for two values of the Tresca factor f using copper ($E/\sigma_y = 300$). It can be seen that there is a load range, which depends on the Tresca factor and on the mechanical properties of the deforming material, where predicted friction coefficients are roughly constant. They tend to rise very steeply as the load falls further and approaches zero.

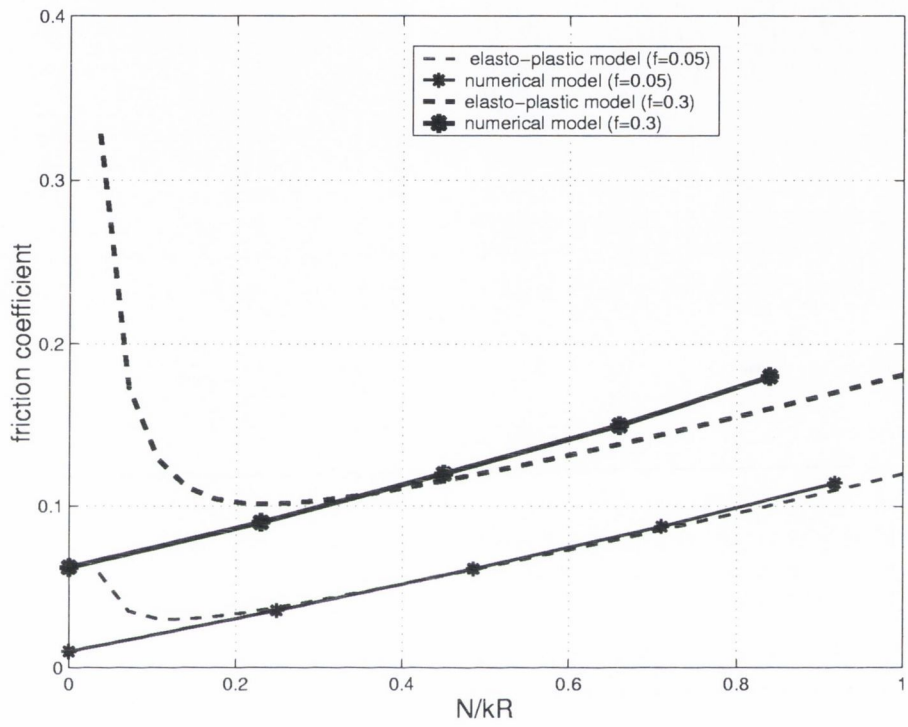


Figure 7.1: Comparison between the friction predictions of the elasto-plastic model of Torrance et al [8] and our numerical model- $E/\sigma_y = 300$

7.1.3 Influence of a third body layer at the interface

The visualisation investigation provided evidence that a mixture of solid particles and lubricant flow at the interface between the full cylinder and the soft material.

In our numerical model, friction is assumed to be controlled by two parameters:

1. The surface roughness parameter, which is for a single cylindrical asperity, the angle of the interface θ or the angle of the chord α , with $\theta = 2\alpha$.
2. The lubrication parameter or Tresca factor f , which represents the shear strength of the interface.

The aim of this section is to analyse the consequences of a third body layer trapped in the contact on the parameters, which control theory.

Influences on the angle of the interface θ or the equivalent chord angle of the interface α ($\theta = 2\alpha$)

It has been shown that the layers of particles trapped in the contact participate at least partly in velocity accommodation by carrying load and being sheared along planes. The distribution of this paste all around and inside the contact area may modify the overall geometry of the contact. The presence of this layer may increase the contact area well beyond the predictions of the slipline field model, which will substantially reduce the real contact pressure.

These effects can be sketched in terms of the chord angle of the interface α . Figure (7.2a) shows the contact geometry as assumed in the slipline field model. Figure (7.2b) shows how elastic effects affect α . α_1 is lower than α due to the presence of the trailing wave behind the center line of the cylinder, as was shown by finite element analysis in section (7.1.2). Figure (7.2c) shows how both the layer of third body and elastic effects may change the initial geometry

of the contact, with $\alpha_2 < \alpha_1 < \alpha$. Consequently, even at the highest loads used in our tests, the contact stresses may be too low to provoke very much plastic deformation in the first bodies, and at all loads, the main dissipative mechanism might be shear in the third body.

For the cut cylinder configuration, elastic effects are much reduced and the trailing wave does not exist, as was shown by finite element analysis. Even if a layer of third body is trapped, this might lead to a slight decrease of the parameter α , but not as significantly as for the full cylinder. The region of contact between the cut cylinder and the deformed material is concentrated to the leading side of the cut cylinder, inducing high contact pressure close to the geometrical discontinuity. The removal of the trailing side of the cylinder probably creates a clearance angle for the particles to escape. For a wedge-shaped asperity, the same features as for the cut cylinder configuration probably occur too.

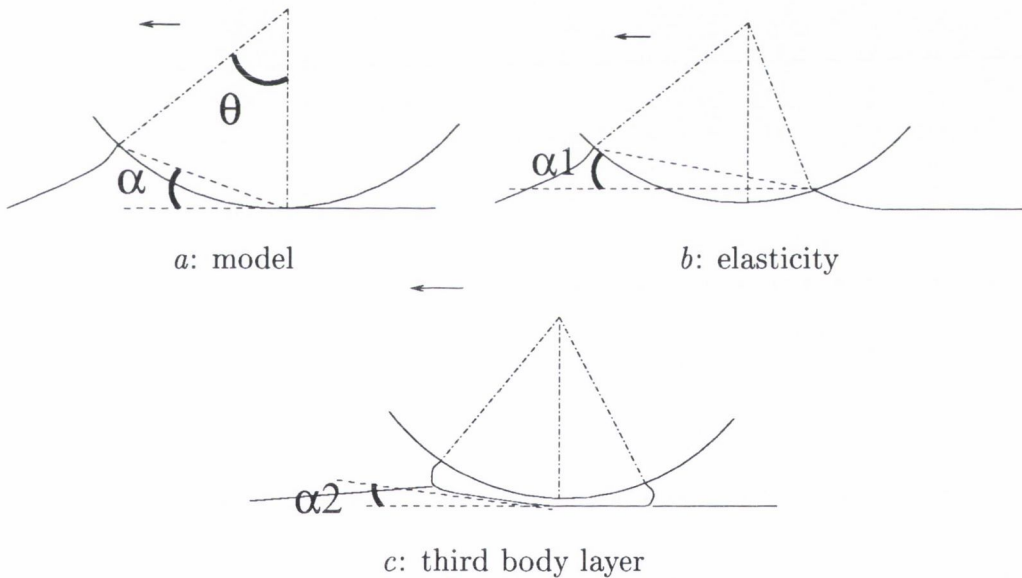


Figure 7.2: Influence of elasticity and a third body layer on the parameter α

Influence on the lubrication parameter f

In the slipline field model, the Tresca factor f , which is the strength of the interface τ as a fraction of the flow stress of the deforming material k , has been assessed through wedge shaped asperity experiments (see appendix (H)). A value of $f = 0.05$ has been determined for both materials and used to analyse the results with a full and a cut cylinder. We thus assumed that the boundary film formed at the interface between the wedge and the deforming material is of similar physical and chemical nature as in the cylinder configuration and that the shearing of this interfacial layer is equivalent, in terms of boundary conditions for the deforming material, to a constant shear stress. Although $f = 0.05$ might be characteristic of the shear strength of the interfacial layer for the cut cylinder configuration, this value might not be characteristic any more for the full cylinder configuration. The full cylinder configuration favours the entrapment of a fairly thick layer composed of a mixture of detached particles and lubricant, whereas in the cut cylinder configuration, these effects are limited by factors of geometry and pressure distribution.

A paste formed by detached particles and lubricant, as was observed in the experiments will have rheological properties which depend mainly on [67, 70] :

1. the amount of third body involved (thickness of the layer)
2. the relative solid/fluid content of the resulting paste
3. the distribution all over the contact
4. its rheology: viscosity or shear strength
5. the contact shape.

It is thus possible that the strength of the interface is different for the full cylinder configuration from that for the cut cylinder and wedge configurations.

7.1.4 Interpretation of our experimental results

The case of the full cylinder

Figures (7.3) and (7.4) recall the friction results obtained in the experiments S_1 with a full cylinder (circles on each graph) and compared with the friction predictions of our numerical model (stars for each graph) for aluminium and copper respectively.

The elasticity of both materials can be quantified non-dimensionnally by the ratio of elastic modulus E to yield strength σ_y , with ($E/\sigma_y = 200$) for aluminium, and ($E/\sigma_y = 300$) for copper. In our experiments, the asperity loads (N/kR) lie within the range 0.2-0.8, which values correspond to initial values of effective chord angle α , with $2\alpha = \theta$, within the range 1° - 6° . Elastic effects are expected to be more important for aluminium than for copper. This is consistent with the experimental results, where friction coefficients measured for aluminium deviate from the trends predicted by slipline field theory, whereas results for copper are closer.

The presence of a third body layer might imply a decrease of the effective chord angle (α) for a given load (N/kR). In our tests, the asperity loads (N/kR) lie within the range 0.2-0.8. However, the range of effective asperity angles might have been actually lower than predicted by slipline field theory and within the range predicted by Torrance [29], where friction levels out as was shown in figure (7.1). Elastic effects and the third body layer can explain both that for both materials, friction coefficients are higher than our numerical model predictions.

Furthermore, the value of $f = 0.05$ for the Tresca factor, as assessed through wedge experiments is probably not characteristic of the shear strength of the interface for this configuration. Taking $f = 0.25$ and $f = 0.3$ for aluminium and copper respectively, leads to a reasonable agreement between the friction coefficients measured for both materials and the predictions of the model of Torrance et al [8] as shown in figures (7.3) and (7.4).

For the highest loads, this latter model is equivalent to the slipline field solution. For lowest loads, there is a load range, which depends on the mechanical properties of both materials and on the nature of the boundary film, where friction is predicted to be constant and finally to level out as load approaches zero. The differences in behaviour between aluminium ($E/\sigma_y = 200$) and copper ($E/\sigma_y = 300$) in the experiments can be explained by elastic effects. The load range of the tests corresponds to an elasto-plastic behaviour for aluminium and a rigid-plastic one for copper, as shown in figure (7.4) by the agreement between our numerical model, for $f = 0.3$ and the friction results for copper.

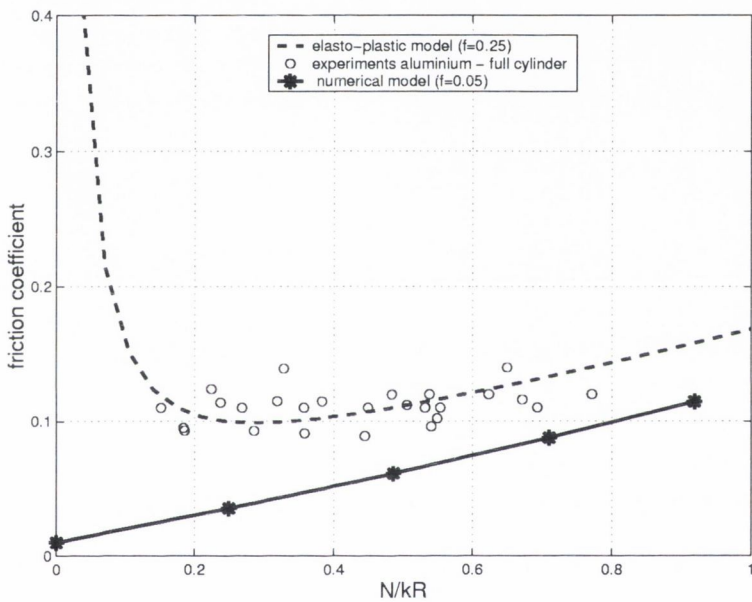


Figure 7.3: Experimental results and the predictions of the elasto-plastic model of Torrance et al [8] - Aluminium

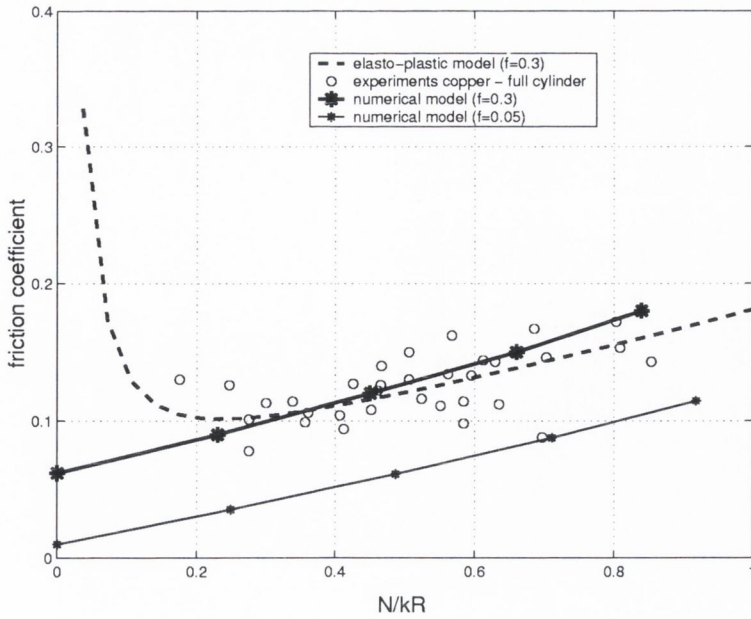


Figure 7.4: Experimental results and the predictions of the elasto-plastic model of Torrance et al [8] - Copper

The case of the cut cylinder

A better accordance between slipline field theory and experiments with a cut cylinder is predicted by finite element analysis. If the trailing wave is removed, the plastic deformation is concentrated in a smaller zone and elastic effects become less important. A second reason why theory predicts well μ for this configuration is that the entrapment of a third body layer is much reduced. Furthermore, the paste of particles and lubricant which flows at the interface is probably of similar nature as for the wedge configuration. The value of $f = 0.05$ assessed for both materials is characteristic of the shear strength of the interface for this configuration.

7.2 Prediction of Strains

7.2.1 Introduction

In chapter (4), our numerical model has been shown to offer more refined information concerning the deformation pattern, left behind the cylinder in the soft surface than the chord model of Challen and Oxley [1]. The main difference is that the strains vary with depth, being higher than the predictions of the chord model near the surface, and falling to zero at the boundary of the deformation field.

Figure (7.5) shows a typical distorted grid predicted by our model. Figure (7.6) gives a quantitative estimate of the strain cycle undergone by the material for different streamlines (or depth) and shows how it compares with the predictions of the chord model [1] for the same conditions.

The aim of this section is to compare the strains predicted by our model to the strains measured in model asperity experiments.

The strain pattern predicted by our model is also compared to the morphology of detached particles, collected after wedge experiments.

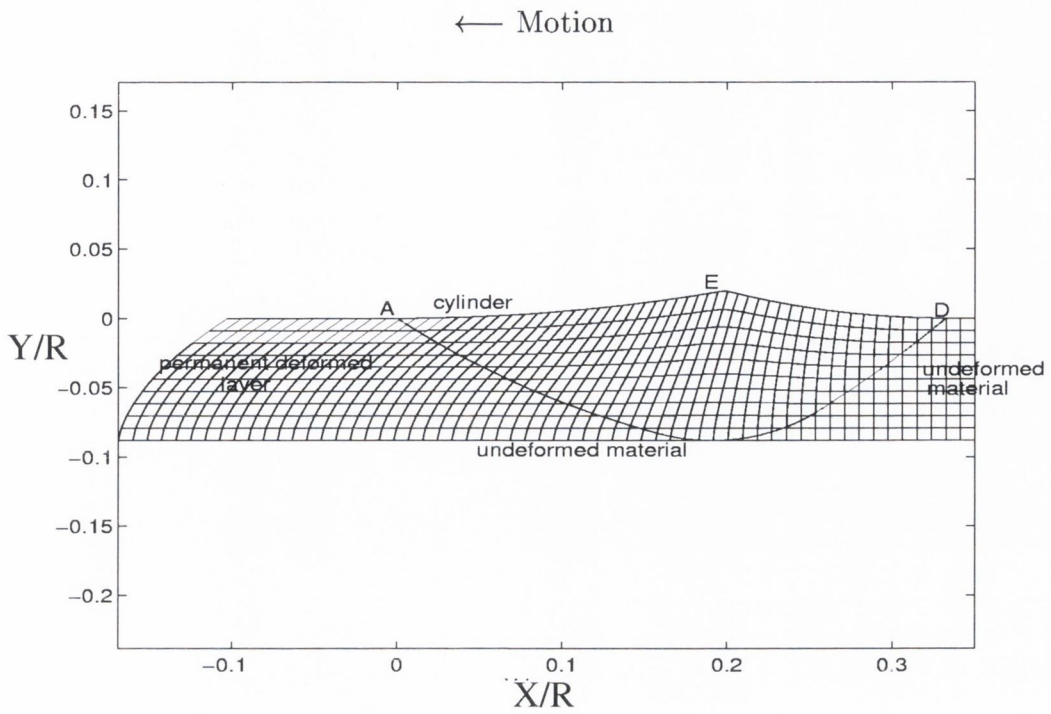


Figure 7.5: Distorted grid predicted - Conditions: $\theta = 0.2rad$, $f = 0.25$

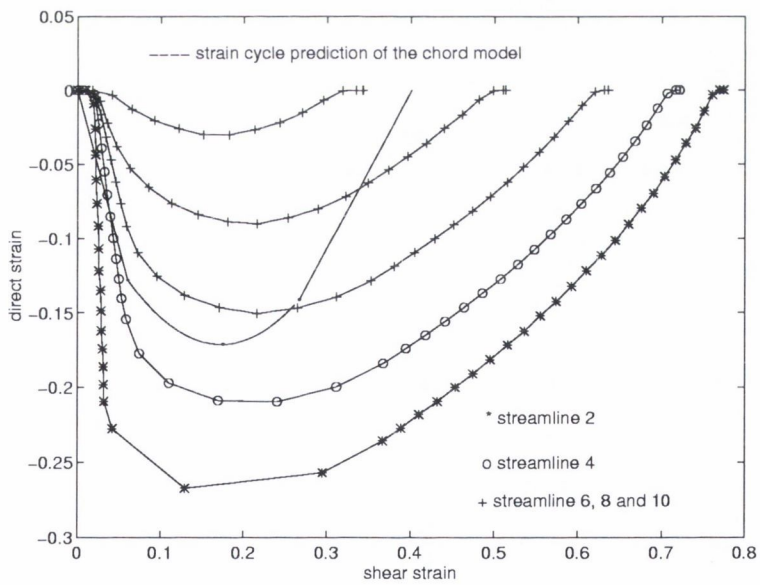


Figure 7.6: ϵ_{xx} versus γ_{xy} - full line: chord model[1] - Conditions: $\theta = 0.2rad$, $f = 0.25$

7.2.2 Comparison with strain patterns observed in previous work

Comparison with the strain patterns obtained after wedge shape model asperity experiments

It is interesting that the strain pattern obtained with our model is much closer than the chord model to what was observed by Kopalinsky [7] and also by Yang [6] in experiments where the plastic strains left by model wedge-shaped asperities were measured by visioplastic methods. Figure (7.7) shows an example of such a highly strained layer taken from a test in which a wedge of attack angle 10° was rubbed against a 5083 aluminium alloy (taken from Yang [6]). Kopalinsky argued that the higher strains near the surface were a consequence of work hardening, which may be true with a perfectly sharp wedge-shaped asperity. However Yang observed that the tip of the wedge used rapidly became rounded, so that it could be better described as cylindrical.

Using our numerical model presented here for equivalent conditions with a cylindrical slider ($\theta = 20^\circ$, $f = 0.25$, $k_s = 236MPa$), we find that the obtained distorted grid plotted in figure (7.8), is close to that observed by Yang [6]. The maximum shear strain $\gamma_{\alpha MAX}$ left at the surface, (see definitions in chapter (3)) measured by Yang [6] was approximately $\gamma_{\alpha MAX} = 12$. Figure (7.9) shows how our numerical model predicts the variations of the shear strain γ_α with depth for this case. It can be seen that a maximum shear strain of 11 is predicted near the surface, which is close to the one observed in Yang's experiment.

It should be noted that the grid obtained by Yang [6] was obtained after 95 passes approximately of the asperity over the same track. Our model predicts this strain pattern after one pass of the asperity. The rigid-plastic theory (see chapter (1)) assumes that no wear takes place until the deformed layer has suffered sufficient damage throughout its volume for failure to occur and for material to be removed. This a direct consequence of the fact that the wave model or the chord model [2, 1] predicts an homogeneously deformed

layer. There is a difference between theory and observations, which is that the layer removed from the surface for each pass seems much thinner than the thickness of the deformed layer [6, 97]. Our numerical results provide an explanation for this and suggest that wear would proceed continuously, with material becoming steadily more deformed as it approaches the wearing surface.

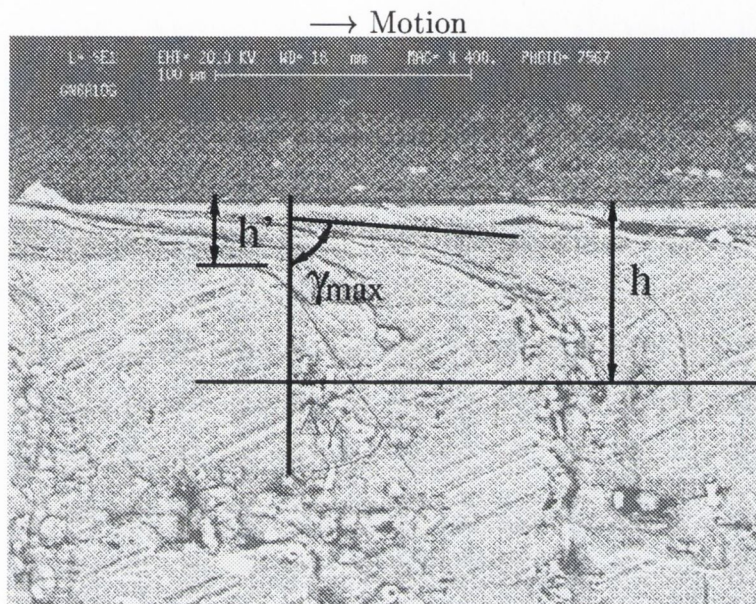


Figure 7.7: S.E.M. image taken from [6]. Grid size: $100\mu\text{m}$

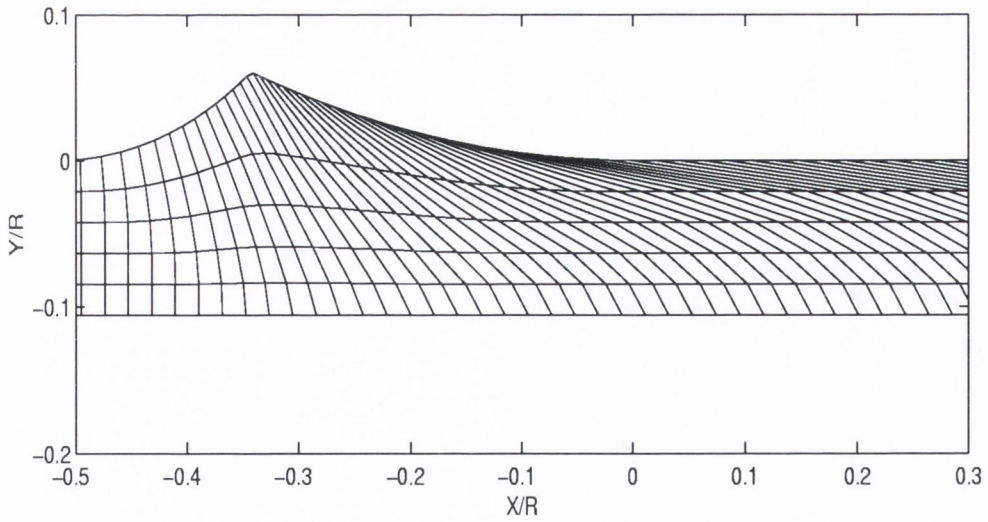


Figure 7.8: Grid obtained by our model. $\theta = 20^\circ$, $f = 0.25$, $k_s = 236\text{MPa}$.

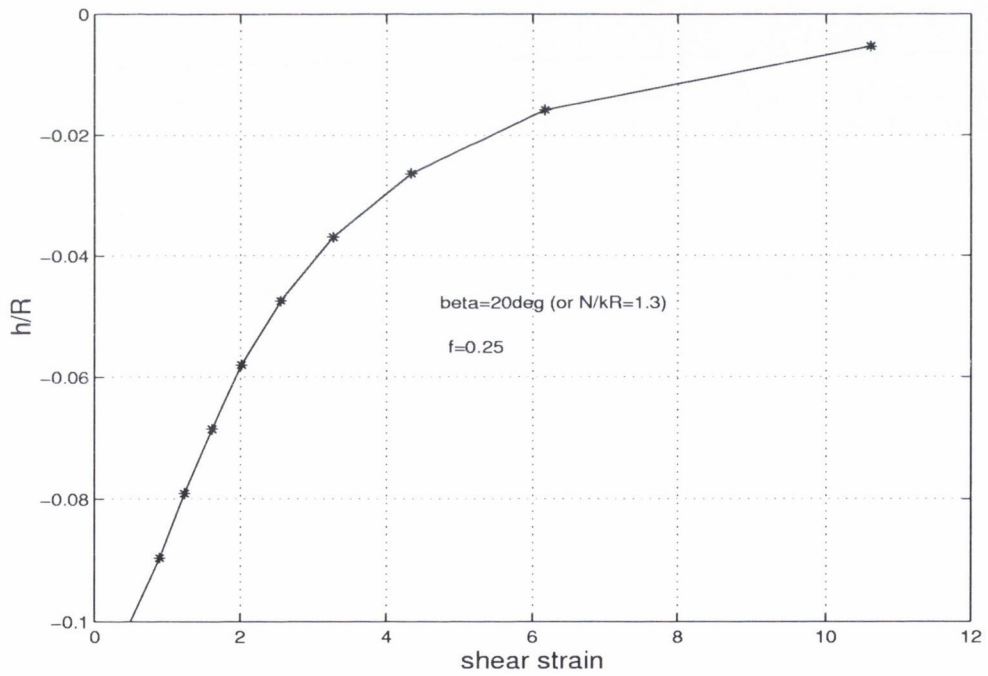


Figure 7.9: Variation of γ_α with depth predicted by our model. $\theta = 20^\circ$, $f = 0.25$, $k_s = 236\text{MPa}$

Comparison with the strain patterns obtained after cylinder shape model asperity experiments

Very recently [11], the strain pattern left by a cylinder in C.B.N. on the 2011 aluminium alloy tested in this work has been observed by viscoplastic methods. In these experiments, the set-up, the cylindrical tool and the lubrication conditions were identical to those described in chapter (5).

Figure (7.2.2) presents a cross section normal to the friction track and parallel to the direction of motion, obtained for $N/kR = 0.7$ approximately. As for the wedge experiments [7, 6], the specimen presents a highly strained layer near the surface which gradually decreases to zero at the bottom of the deformed layer. Figure (7.2.2) shows how the shear strain (γ_α) measured approximately on this grid varies with depth (stars on the graph). Using our numerical model for identical loading conditions and for a Tresca factor within the range $f = 0.2 - 0.5$ to account for a third body layer (see section (7.1.4)), we find that the high shear strains observed near the surface of the specimen can be quantitatively predicted for $f = 0.4$.

It should be noted that this experimental grid has been obtained after one pass of the asperity. Even if further experiments need to be performed under more controlled lubrication conditions to confirm this correlation between our numerical model and experiments, this suggests that slipline field theory can predict quantitatively the high shear strains near the surface for high loads.

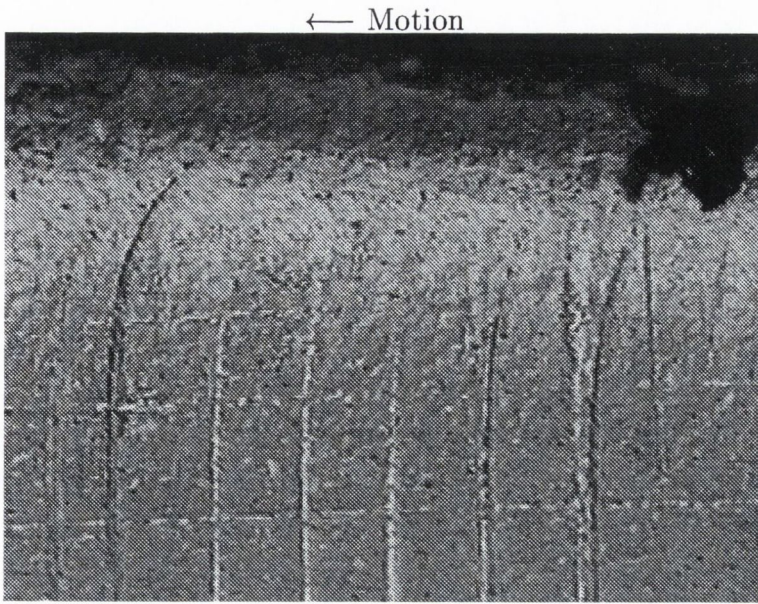


Figure 7.10: Grid taken from [11], $N/kR = 0.7$, $f = 0.2-0.5$, grid size = $100\mu\text{m}$

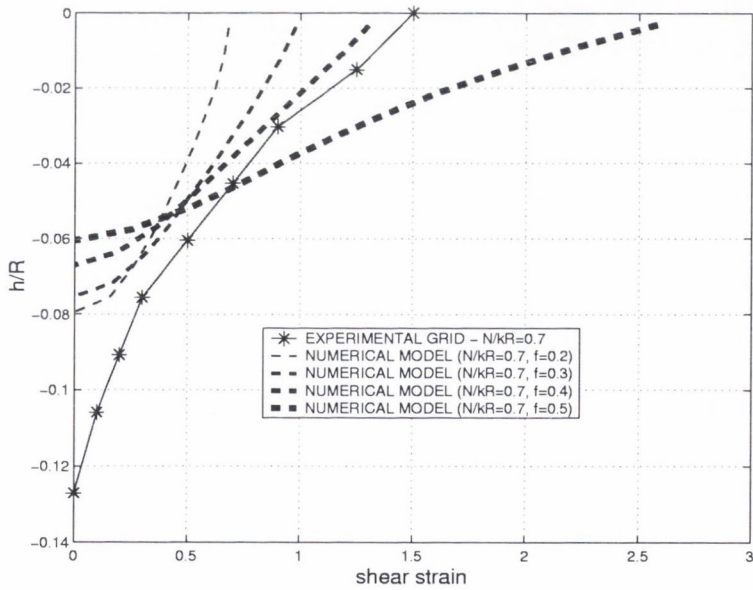


Figure 7.11: Comparison of γ_α as a function of h/R measured from the grid and calculated from the numerical model for different values of f

7.2.3 Comparison with the morphology of wear debris collected after wedge experiments

By careful metallography, Torrance and Zhou [57] observed the cracks and the wear particles produced by sliding a wedge over an aluminium alloy ($k_s = 170\text{MPa}$). At higher angles of attack some flaky wear particles were observed, whereas at lower attack angles the particles were block-like and resembled irregular pyramids. They explained the two distinct particle shapes by a change in the elastic stress field to the rear of the contact. However, an alternative explanation can be proposed. The two conditions studied in their work correspond to a cylindrical slider with $\theta = 5\text{ deg}$ and one with $\theta = 16\text{ deg}$, f being 0.275 in both cases. Figure (7.12) shows how the shear strain γ_α varies with depth in each case. With $\theta = 16\text{ deg}$, intense shear occurs near the surface, which will favour the shear cracking of a thin surface layer to give flaky particles much thinner than the overall thickness of surface deformation. With $\theta = 5\text{ deg}$, shear is more uniform, which will favour the formation of thicker particles as was observed. These findings may have some importance on the mechanism of wear particle detachment in ductile metals.

It should be noted that this correlation only holds if the size, morphology and the composition of the debris collected are not significantly different from those of the particles when detached from the first bodies, as was the case in our full cylinder experiments.

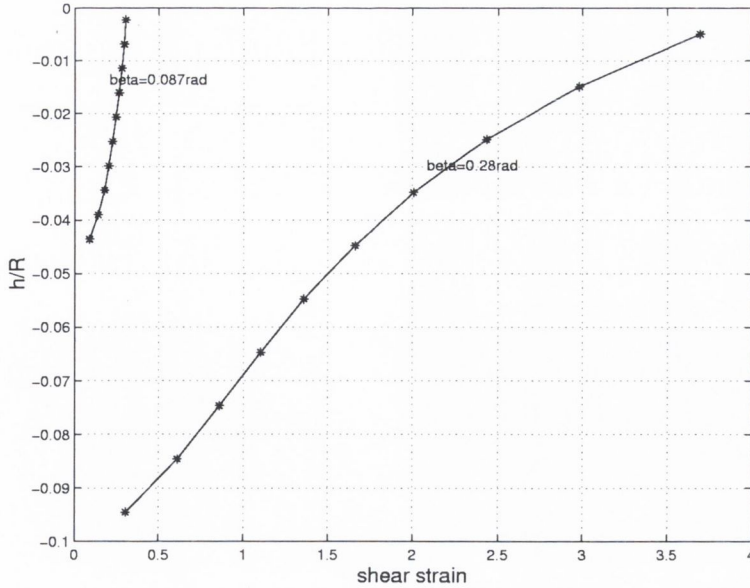


Figure 7.12: Evolution of γ_θ for $\alpha = 2.5$ deg, ($\theta = 0.087$ rad) and $\alpha = 8$ deg, ($\theta = 0.28$ rad) for $f = 0.275$.

7.3 conclusions

7.3.1 Friction

The case of the full cylinder

Elastic effects induce the formation of a trailing wave, which will favour the entrapment of detached particles at the interface and give higher friction coefficients than predicted by our model for the lowest loads. For the highest loads, slipline field theory can predict friction.

The presence of a third body layer may induce an increase of the contact area, and thus a decrease of the contact pressure on the wearing material. A second effect is that the shear strength of the interface is strongly dependent of the nature and rheology of the mixture of detached particles/lubricant formed at the interface.

Slipline field theory predicts friction well above a given load N/kR , which value depends on the degree of elasticity E/σ_y of the material and on the Tresca

factor f . Below this load, elastic effects can not be neglected in predicting friction.

The case of the cut cylinder

For the cut cylinder configuration, elastic effects are reduced, due to the removal of the trailing wave. Furthermore, the Tresca factor can be measured independently through wedge shape experiments.

Thus for this configuration, the conditions of our tests approximate closely the assumptions of our numerical model. Slipline field theory predicts friction coefficients well.

7.3.2 Strains

The main conclusions concerning the strain predictions are:

- The strain pattern calculated by our numerical model is much closer than the chord model of Challen and Oxley [1] to the strained layers observed by several authors in experiments with model asperity experiments, and this without referring to strain-hardening or elasticity. Though the comparison is based only on a few experiments, some quantitative correlation have been found between the high strains near the surface measured in experiments and those predicted by our numerical model.
- Furthermore, the morphology of the debris produced during wedge experiments have been explained to some extent by our model. This means that our model is a new quantitative tool for investigating the mechanism of wear particle detachment in ductile metals.

Chapter 8

Conclusions

8.1 The present investigation

The present investigation assumes that the rigid-plastic approximation has the possibility to predict wear for engineering contacts.

Both theoretical and experimental approaches have been carried out to investigate the sliding cylinder problem.

Theoretical investigation

A new rigid-plastic asperity contact model is proposed, which models the wave of plastically deformed material pushed ahead of a rigid cylinder. The slipline field proposed is a potential rigid-perfectly plastic solution for the sliding cylinder problem. The solution has been shown to be kinematically admissible but has to be considered incomplete until a statically admissible extension of the plastic stress field into rigid regions is proved to exist. However, the model proposed is suitable for small values of surface roughness parameter θ and lubrication parameter f . For high values of θ and f , the model is not valid any more as a change of regime is expected when the asperity penetration becomes greater and the lubrication poorer.

This model is able to predict the friction coefficient and the strains as-

sociated with the process. In friction, our model has been shown to be in good agreement with the chord approximation model of Challen and Oxley [1]. The main advantage of the new model proposed here lies in strain pattern predictions. The main difference is that the strains predicted by our model vary with depth, being higher than the predictions of the chord model near the surface, and falling to zero at the boundary of the deformed layer. Thus this new model offers more refined information concerning the strain pattern, being closer to the strained layers observed usually in experiments than the existing quantitative models.

This highly strained layer observed near the surface has been already predicted by finite element analysis [29] for the wedge configuration and in the present work for the cylinder configuration. However, finite element analysis has the disadvantage of requiring far more computer time.

Experimental investigation

The friction and strain predictions of our numerical model have been tested against the results of scaled-up model asperity experiments. The main conclusions are recalled now:

Friction coefficients

- Scaled-up model asperity experiments, where a full cylinder in C.B.N. slides across the surface of two non-ferrous metals have been performed. Significant deviations from our numerical model have been observed. Elasto-plastic finite element analysis has been performed, which predicts deviations for a real material from slipline field theory due to the presence of elastic distortions. These elastic effects induce the formation of a trailing wave at the rear of the contact, which will furthermore favour the entrapment of detached particles. The presence of a third body layer at the interface between the cylinder and the deformed material

has been established in our tests. This may induce an increase of the contact area, and thus a decrease of the contact pressure on the wearing material. A second effect is that the shear strength of the interface is strongly dependent of the nature and rheology of the mixture of detached particles/lubricant formed at the interface.

Both elastic effects and the presence of a third body layer influence friction. Slipline field theory predicts friction satisfactorily above a given load (N/kR), whose value depends on the degree of elasticity (E/σ_y) of the deforming material and on the Tresca factor f . Below this limiting load which has been observed to be different for the two materials tested, elastic effects cannot be neglected to predict friction.

- To decrease the influence of both elastic effects and the third body layer, additional experiments have been performed with the use of a cut cylinder, whose trailing side has been removed. For this configuration, elastic effects and the influence of detached particles have been shown to be reduced considerably and the conditions of our experiments approximated thus more closely the assumptions of our numerical model. Slipline field theory predicts friction satisfactorily for the two tested materials.

Strains

The main conclusions concerning the strain predictions are:

- The strain pattern calculated by our numerical model is much closer than the chord model of Challen and Oxley [1] to the strained layers observed by several authors in experiments with model asperity experiments, and this without referring to strain-hardening or elasticity. Though the comparison is based only on a few experiments, some quantitative correlation have been found between the high strains near the surface measured in experiments and those predicted by our numerical model.

- Furthermore, the morphology of the debris produced during wedge experiments have been explained to some extent by our model. This indicates that our model is a new quantitative tool to investigate the mechanism of wear particle detachment in ductile metals.

8.2 Perspectives

The new model proposed in the present investigation is a quantitative tool which allows friction but especially strains to be predicted for a wide range of surface roughness (θ) or load (N/kR) and of lubrication conditions f . Some maps providing the strains for a wide range of these two parameters have been given in this thesis.

Further scaled-up model asperity experiments need to be performed to confirm the ability of this model to predict quantitatively friction and plastic strains induced in a soft metal within each pass of a rigid cylinder under defined conditions.

In order to decrease elastic effects, which cannot be neglected for the lowest loads, the use of a cut cylinder has been shown to be successful. Further experiments should be performed with this tool to allow the conditions of the tests to be close to the assumptions of the theoretical model.

In this work, a third body approach has been necessary to interpret our experimental results. It is clear that the entrapment of particles was not desired in our tests because it leads to a more complex situation, where third body effects cannot be neglected. In order to focuss on the debris detachment mechanism and not on velocity accommodation mechanisms, solutions must be investigated to reduce as much as possible the entrapment of compacted debris for this configuration.

In terms of wear predictions, the rigid-plastic theory assumed so far that no wear had taken place until the deformed layer has suffered sufficient damage throughout its volume for failure to occur and to be removed. This a direct

consequence of the fact that the wave model or the chord model [2, 1] predicts a homogeneously deformed layer. There is a difference between theory and observations, which is that the layer removed from the surface for each pass seems much thinner than the thickness of the deformed layer [6, 97]. Observations and analysis also show that wear is a continuous procedure rather than a discontinuous one [6, 97]. The model proposed here allows the existing wear theory to be developed, by integrating into wear calculations the strain cycle which depends on the depth. Further experiments need to be performed to attempt to establish correlation between the thickness of the debris produced and the depth of the highly strained layer predicted at the surface.

Finally, it is clear that any conclusions made on the ability of the theory to calculate the friction coefficient and the strains may not be meaningful because a single cylinder used in experiments cannot represent completely a real surface. The extension of the single asperity test for use on a real engineering surface needs to be investigated too.

Bibliography

- [1] J. M. Challen and P. L. B. Oxley. Slipline fields for explaining the mechanics of polishing and related processes. *Int. J. Mech. Sci.*, 26(6–8):403–418, 1983.
- [2] J. M. Challen and P. L. B. Oxley. An explanation of the different regimes of friction and wear using asperity deformation models. *Wear*, 53:229–243, 1979.
- [3] M. Busquet and A. A. Torrance. Investigation of surface deformation and friction when a hard cylindrical asperity slides over a soft smooth surface. In *Proc. 25th. Leeds-Lyon Symposium on Tribology*, pages 101–109, 1999.
- [4] R. Hill. *The Mathematical Theory of Plasticity*. Oxford University Press, 1950.
- [5] W. Johnson, R. Sowerby, and R.D. Venter. *Plane Strain Slipline Fields for Metal Deformation Processes*. Pergamon Press, 1982.
- [6] Y. Yang. *The prediction of the wear rates of ductile materials through their surface strains*. PhD thesis, Trinity College, University of Dublin, September 1997.
- [7] E. M. Kopalinsky. Investigation of surface deformation when a hard wedge slides over a soft surface. *Trans. ASME J. Tribology*, 114:100–106, 1992.
- [8] A.A. Torrance, J. Galligan, and G. Liraut. A model of the friction of a smooth hard surface sliding over a softer one. *Wear*, 212:213–220, 1997.

- [9] Y. Berthier. Maurice Godet's third body approach. In *Proc. 22nd Leeds-Lyon Symposium on Tribology*, pages 21–30, 1996.
- [10] S. Descartes. *Lubrification solide à partir d'un revêtement de MoSx : Conséquences de la rhéologie et des débits de troisième corps sur le frottement*. PhD thesis, I.N.S.A., Lyon, France, October 1997.
- [11] M. Gagachian. Visioplastic measurements of asperity strains. Final year project report, Department of Mechanical and Manufacturing Engineering, Trinity College, Dublin, Ireland, March 2000.
- [12] M. Godet. Third-bodies in tribology. *Wear*, 136:29–45, 1990.
- [13] J. A. Williams. *Engineering Tribology*. Oxford Science Publications, 1994.
- [14] B. S. Hockenhull, E. M. Kopalinsky, and P. L. B. Oxley. An investigation of the role of low cycle fatigue in producing surface damage in sliding metallic friction. *Wear*, 148:135–146, 1991.
- [15] Y. Yang and A.A. Torrance. Wear by plastic ratchetting: an experimental investigation. *Wear*, 196:147–155, 1996.
- [16] Y. Yang, A.A. Torrance, and P.L.B. Oxley. Modelling mechanical wear processes in metallic sliding friction. *J. Phys. D: Appl. Phys.*, 29:600–608, 1996.
- [17] D. Tabor. Junction growth in metallic friction. volume 251, pages 378–393, 1959.
- [18] D. A. Rigney and J. E. Hammerberg. Unlubricated sliding behavior of metals. *Materials Research Society. MRS Bulletin*, 23(6):32–36, 1998.
- [19] I. Saunders and J. Nutting. Deformation of metals to high strains using combination of torsion and compression. *Metal Sci.*, 18:571–575, 1984.

- [20] S. Nourbakhsh and J. Nutting. Structure and properties of quenched and aged cu-2Be after deformation to large strains. *Metal Sci.*, 16:323–331, 1982.
- [21] A. A. Torrance and A. Cameron. Surface transformation in scuffing. *Wear*, 28:299–311, 1974.
- [22] A.P. Voskamp. Material response to rolling contact loading. *Trans. A.S.M.E. J. Tribology*, 107:359–366, 1985.
- [23] A. P. Voskamp. Crystallographic preferred orientation induced by cyclic rolling contact loading. In *Proc. 8th. ICOTOM Kallend S. and Gottstein G., Eds. Metallurgical Soc.*, pages 919–924, 1988.
- [24] H. J. Christ, C. Sommer, H. Mughrabi, A. P. Voskamp, J. M. Beswick, and F. Hengerer. Fatigue behaviour of three variants of the roller bearing steel SAE 52100. *Fatigue Frac. Engng. Mater. Struct.*, 15(9):855–870, 1992.
- [25] J. Morgan, R. J. Stokes, and A. A. Deformation in heavily loaded rolling contacts. In *Proc. 8th. Leeds-Lyon Symposium on Tribology*, pages 184–191, 1982.
- [26] J. H. Dautzenberg and J. H. Zaat. Quantitative determination of deformation by sliding wear. *Wear*, 23:9–19, 1973.
- [27] D. A. Rigney, L. H. Chen, M. G. S. Naylor, and A. R. Rosenfield. Wear processes in sliding systems. *Wear*, 100:195–219, 1984.
- [28] A. A. Torrance. Debris detachment in plastic contact. In *Proc. 18th. Leeds-Lyon Symposium on Tribology*, pages 49–55, 1992.
- [29] A. A. Torrance. The influence of surface deformation on mechanical wear. *wear*, 200:45–54, 1996.

- [30] J. M. Challen, P. L. B. Oxley, and B. S. Hockenhull. Prediction of Archard's wear coefficient for metallic sliding friction assuming a low cycle fatigue wear mechanism. *Wear*, 111:275–288, 1986.
- [31] P. Lacey and A. A. Torrance. The calculation of wear coefficients for plastic contacts. *Wear*, 145:367–383, 1991.
- [32] J. E. Merwin and K.L. Johnson. An analysis of plastic deformation in rolling contact. *Proc. I. Mech. E.*, 177:676–685, 1963.
- [33] K. L. Johnson and J. A. Jefferis. Plastic flow and residual stresses in rolling and sliding contact. In *Proc. I. Mech. Eng. Symposium on fatigue in rolling contact*, pages 54–65, 1964.
- [34] A. Kapoor, K. L. Johnson, and J. A. Williams. A model for the mild ratchetting wear of metals. *Wear*, 200:38–44, 1996.
- [35] A. W. Crook. Simulated gear-tooth contacts: some experiments upon their lubrication and sub-surface deformations. *Proceedings IMechE*, 171:187, 1957.
- [36] V. Bhargava, G. T. Hahn, and C. A. Rubin. An elastic-plastic finite element model of rolling contact. part 1: single contact. part 2: multiple contact. *Trans. ASME J. Appl. Mech.*, 52:66–82, 1985.
- [37] A. D. Hearle and K. L. Johnson. Cumulative plastic flow in rolling and sliding contact. *Trans. ASME J. Appl. Mech.*, 54:1–7, 1987.
- [38] A. F. Bower and K. L. Johnson. The influence of strain hardening on cumulative plastic deformation in rolling and sliding line contact. *J. Mech. Phys. Solids*, 37(4):471–493, 1989.
- [39] T. Akagaki and K. Kato. Plastic flow process of surface layers in flow wear under boundary lubricated conditions. *Wear*, 117:179–196, 1987.

- [40] T. Akagaki and K. Kato. Wear mode diagram in lubricated sliding friction of carbon steel. *Wear*, 129:303–317, 1989.
- [41] A. Kapoor and K. L. Johnson. Plastic ratchetting as a mechanism of metallic wear. *Proc. Roy. Soc. Londn Symposium on Tribology*, 445:367–381, 1994.
- [42] A. Kapoor, J. A. Williams, and K. L. Johnson. The steady state sliding of rough surfaces. *Wear*, 175:81–92, 1994.
- [43] H. A. Greenwood and J. B. P. Williamson. Contact of nominally flat surface. *Proc. Roy. Soc. Lond. A*, 295:300–319, 1966.
- [44] D. J. Whitehouse and J. F. Archard. The properties of random surfaces of significance in their contact. *Proc. Roy. Soc. Lond. A*, 316:97–121, 1970.
- [45] A. P. Green. Friction between unlubricated metals: a theoretical analysis of the junction model. *Proc. Royal Soc. London- Ser. A*, 228:191–204, 1954.
- [46] F. P. Bowden and D. Tabor. *The friction and lubrication of solids. Part 2*. Oxford University Press, Amen House, London, 1964.
- [47] H. Petryk. Slipline field solutions for sliding contact. *I. Mech. E.*, C140:987–994, 1987.
- [48] B. Avitzur, M. Eto, and E. Kay. Treating rolling vs. sliding friction by the wave model. *Wear*, 156:211–237, 1992.
- [49] K. L. Johnson. *Contact mechanics*. Cambridge University Press, Cambridge, 1985.
- [50] J. M. Challen, L. J. Mclean, and P. L. B. Oxley. Plastic deformation of a metal surface insliding contact with a hard wedge: its relation to friction and wear. *prsa*, 394:161–181, 1984.

- [51] A. J. Black, E. M. Kopalinsky, and P. L. B. Oxley. An investigation of the different regimes of deformation which can occur when a hard wedge slides over a soft surface: the influence of wedge angle, lubrication and prior plastic working of surface. *Wear*, 123:97–114, 1988.
- [52] H. Moalic, J. A. Fitzpatrick, and A. A. Torrance. The correlation of the characteristics of rough surfaces with their friction coefficients. *Proc. Inst. Mech. Engrs.*, 201(C5):321–329, 1987.
- [53] J. D. Bressan, G. Genin, and J. A. Williams. The influence of pressure, boundary film shear strength and elasticity on the friction between a hard asperity and a deforming softer surface. In *Proc. 25th. Leeds-Lyon Symposium on Tribology*, pages 79–90, 1999.
- [54] A. Kapoor. A re-evaluation of the life to rupture of ductile metals by cyclic plastic strain. *Fatigue Fract. Engng. Mater. Struct.*, 17(2):201–209, 1994.
- [55] E. M. Kopalinsky, P. L. B. Oxley, and H. T. Young. A strain-hardening slipline field analysis of the plastic deformation observed in a model asperity interaction experiment. *J. Mech. Phys. Solids*, 38(6):765–785, 1990.
- [56] A. A. Torrance. The calculation of residual stresses in worn surfaces. *Proc. I. Mech. E. (Lond.)*, 208:113–119, 1994.
- [57] A. A. Torrance and F. Zhou. Fracture modes in wear particle formation. In *20th Leeds-Lyon Symposium on Tribology*, pages 521–529, 1993.
- [58] W. H. Roberts. Some current trends in tribology in the U.K. and Europe. In *Int. Conf. on Tribology, Tokyo 8-10 July 1985, Japan Society of Lubrication Engineers*, 1985.
- [59] J. M. Challen, E. M. Kopalinsky, and P.L.B. Oxley. An asperity deformation model for relating the coefficients of friction and wear in sliding metal friction. *I. Mech. E.*, C156/87:957–964, 1987.

- [60] A. A. Torrance and A. Parkinson. Towards a better surface finish for bearing materials. In *Proc. 19th. Leeds-Lyon Symposium on Tribology*, 1993.
- [61] A. A. Torrance. Using profilometry for the quantitative assessment of tribological function: PC-based software for friction and wear prediction. *Wear*, 181–183:397–404, 1995.
- [62] P. Lacey, A. A. Torrance, and J.A. Fitzpatrick. The relation between the friction of lubricated rough surfaces and apparent pressure. *ASME Trans., J. of Tribology*, 111:260–264, 1989.
- [63] J. Galligan, A.A. Torrance, and G. Liraut. A scuffing test for piston ring / bore combinations: Pt. 1 stearic acid lubrication. *Wear*, 236:199–209, 1999.
- [64] J. Galligan, A.A. Torrance, and G. Liraut. A scuffing test for piston ring / bore combinations: Pt. 2 formulated motor lubrication. *Wear*, 236:210–220, 1999.
- [65] F. P. Bowden and D. Tabor. *The friction and lubrication of solids. Part 1*. Oxford University Press, Amen House, London, 1950.
- [66] B. J. Briscoe, B. Scruton, and F.R. Willis. The shear strength of thin lubricant films. *Proceedings Royal Society of London A*, 333:99–114, 1973.
- [67] K. L. Johnson. Aspects of friction. In *Proc. 7th. Leeds-Lyon Symposium on Tribology*, pages 3–12, 1980.
- [68] R. M. Mortier and S.T. Orszulik. *Chemistry and technology of lubricants*. Blackie Academic and Professional, London, 1997.
- [69] A. J. Black, E. M. Kopalinsky, and P. L. B. Oxley. Sliding metallic friction with boundary lubrication: an investigation of a simplified friction theory and of the nature of boundary lubrication. *Wear*, 137:161–174, 1990.

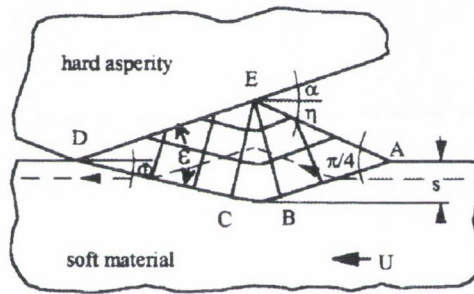
- [70] T. M. Beagley. The rheological properties of solid rail contaminants and their effect on wheel/rail adhesion. *Proceedings IMechE*, 190(39):419–428, 1976.
- [71] M. Godet. The third body approach: a mechanical view of wear. *Wear*, 100:437–452, 1984.
- [72] Y. Berthier, M. Godet, and M. Brendle. Velocity accommodation in friction. *Tribology Transaction*, 32:490–496, 1989.
- [73] P. Jacquemard, M. H. Meurisse, and Y. Berthier. From phenomenology to the concepts which flow from the third body. Application to radial face seal. In *Proc. 22nd. Leeds-Lyon Symposium on Tribology*, pages 91–102, 1996.
- [74] S. Descartes and Y. Berthier. Load carrying loci: link with the rheology and the flows of solid third body. case of third body formed from a MoSx coating. In *Proc. 25th. Leeds-Lyon Symposium on Tribology*, 1999.
- [75] K. P. Haff. Grain flow as a fluid-mechanical phenomenon. *Journal of Fluid Mechanics*, 134:401–430, 1983.
- [76] A. A. Lubrecht, C. Chan Tien, and Y. Berthier. A simple model for granular lubrication, influence of boundaries. In *Proc. 22nd. Leeds-Lyon Symposium on Tribology*, volume 31, pages 377–385, 1995.
- [77] H. Heshmat. The quasi-hydrodynamic mechanism of powder lubrication: Part 3- on theory and rheology of triboparticulates. *Tribology transaction*, 38(2):269–276, 1995.
- [78] I. Iordanoff and Y. Berthier. First steps for a rheological model for the solid third body. In *Proc. 25th. Leeds-Lyon Symposium on Tribology*, pages 551–559, 1999.
- [79] R.A.C. Slater. *Engineering Plasticity*. The Macmillan Press LTD, 1977.

- [80] H. Ford. *Advanced Mechanics of Materials*. Longmans, 1963.
- [81] W. Prager. *An Introduction to plasticity*. Addison-Wesley, Reading, Mass, 1959.
- [82] J. M. Alexander. A slipline field for the hot rolling process. *Proc. Inst. Mech. Engrs.*, 169:1021, 1955.
- [83] T. C. Firbank and P. R. Lancaster. Plane-strain drawing between dies with a circular profile and zero exit angle. *Int. J. Mech. Sci.*, 6:415–420, 1964.
- [84] L. E. Farmer and P. L. B. Oxley. A slipline field for plane-strain extrusion of a strain-hardening material. *J. Mech. Phys. Solids*, 19:369–388, 1971.
- [85] P. Dewhurst and I.F. Collins. A matrix technique for constructing slipline field solutions to a class of plane strain plasticity problems. *Int. J. Num. Meth. Engng.*, 7:357–378, 1973.
- [86] A.P. Green. Theoretical investigation of the compression of a ductile material between smooth flat dies. *Phil. Mag.*, 42:900–918, 1951.
- [87] E. W. Shimmin and P. L. B. Oxley. Some numerical slipline field solutions for drawing through circular dies. *Int. J. Mech. Sci.*, 25(11):785–802, 1983.
- [88] I.F. Collins. The algebraic-geometry of slipline fields with applications to boundary value problems. *Proceedings Royal Society of London A*, 303:317–338, 1968.
- [89] H. Petryk. Non-unique slipline field solutions for the wedge indentation problem. *J. de Mecanique Appliquee*, 4(3):255–282, 1980.
- [90] E.W. Shimmin. *A theoretical and experimental investigation of deformation in plane strain rolling and drawing through circular dies*. PhD thesis, Faculty of Engineering, The University of New South Wales, 1982.

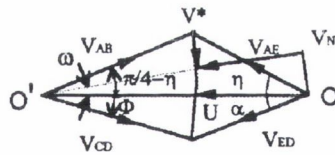
- [91] R. Hill. On the limits set by plastic yielding to the intensity of singularities of stress. *J. Mech. Phys. Solids*, 278(2):278–285, 1954.
- [92] A. V. Olver, H. A. Spikes, A. F. Bower, and K. L. Johnson. The residual stress distribution in a plastically deformed model asperity. *Wear*, 107:151–174, 1986.
- [93] L. E. Farmer and P. L. B. Oxley. A computed-aided method for calculating the distributions of strain-rate and strain from an experimental flow field. *Journal of strain analysis*, 11(1):26–31, 1976.
- [94] A. Jullien, M.H. Meurisse, and Y. Berthier. Determination of tribological history and wear through visualization in lubricated contacts using a carbon-based composite. *Wear*, 194:116–125, 1996.
- [95] S. Descartes, M. Cassard, Y. Berthier, A. Ginet, and A. Aubert. Mosx, a solid lubricant : yes, but which scales of tribological interpretation should be used ? the consequences on the friction of mechanisms. In *Proc. of the Sixth Space Mechanisms and Tribology Symposium, 4-6 octobre 1995, Zurich*, pages 29–34, 1995.
- [96] Y. Berthier. Experimental evidence for friction and wear modeling. *Wear*, 139(1):77–92, 1990.
- [97] E. M. Kopalinsky and P. L. B. Oxley. An investigation of the mechanics of sliding metallic wear under lubricated conditions. *Wear*, 214:38–46, 1998.
- [98] Y. Berthier. *Mecanismes et tribologie*. PhD thesis, I.N.S.A., U.C.B., Lyon, France, 1989.

Appendix A

The wave model [2]: friction calculation



(A) SLIP-LINE FIELD



(B) HODOGRAPH

Figure A.1: Slipline field proposed by Challen and Oxley [2] for the sliding wedge problem

With this model, as shown in figure (A.1), the deformation is represented as a standing wave and the straight line joining A and D must be parallel to U to satisfy volume constancy. The value of f determines the inclination of the sliplines to DE. These conditions together with the further condition that the sliplines must be inclined at an angle $\pi/4$ to the stress-free surface EA to satisfy equilibrium, define the slipline field and it follows from geometry that:

$$\alpha + \Phi = \frac{1}{2} \arccos(f) \quad (\text{A.1})$$

and

$$\eta = \arcsin\left[\frac{\sin(\alpha)}{\sqrt{(1-f)}}\right] \quad (\text{A.2})$$

where Φ is the angle between CD and U and is measured positive. The hodograph shows that there is a discontinuity in the tangential component of velocity across the slipline ABCD so that material which enters and leaves the field with a velocity U flows in the directions AE and ED in the regions ABE and CDE and along a curved path in the centred fan region BCE, as shown by the typical streamline given in figure (A.1).

Sliding at the interface ED is accommodated by shearing of the interfacial film. The shear stress k_s which acts parallel to the sliplines and the mean compressive (hydrostatic) stress p which acts normal to the sliplines in this region are found by starting at the free surface AE where $p = k_s$. Applying the stress equilibrium equation referred to sliplines (Hencky equations) along the slipline ABCD which gives:

$$p = \left[1 + 2\left(\frac{1}{4}\pi + \Phi - \eta\right)\right]k_s \quad (\text{A.3})$$

where $\frac{1}{4}\pi + \Phi - \eta$ is the angle subtended at the centre of the fan BCE. By resolving forces it can be shown that the tangential force F and normal force N are given by:

$$F = \left[\left[1 + 2 \left(\frac{1}{4} \pi + \Phi - \eta \right) \right] \sin \alpha + \cos(\alpha + 2\Phi) \right] \cdot ED \cdot k_s \quad (\text{A.4})$$

$$N = \left[\left[1 + 2 \left(\frac{1}{4} \pi + \Phi - \eta \right) \right] \cos \alpha + \sin(\alpha + 2\Phi) \right] \cdot ED \cdot k_s \quad (\text{A.5})$$

where ED is the length of the interface. For a given normal load, ED can be found from equation (A.5). The basic laws of friction are therefore satisfied with F proportional to N and independent of the area of the contacting surfaces. From equations (A.4) and (A.5) and by substituting for Φ and η from equations (A.1) and (A.2) the coefficient of friction $\mu = F/N$ can be expressed as:

$$\mu = \frac{F}{N} = \frac{(A_s \cdot \cos(\alpha) + \sin(2\epsilon - \alpha)) \cdot ED \cdot k_s}{(A_s \cdot \cos(\alpha) + \sin(2\epsilon - \alpha)) \cdot ED \cdot k_s} \quad (\text{A.6})$$

where:

$A_s = 1 + \frac{\pi}{2} + \arccos(f) - 2\eta - 2\alpha$, from which, for $0 \leq f < \cos(2\alpha)$, μ will lie in the range $0 \leq \mu < 1$.

Appendix B

The chord approximation model [1] and the developed chord model [3]: friction calculation

B.1 The chord approximation model [1]

In this model shown in figure (B.1), the two-dimensional rigid, circular asperity pushes a plastic wave in the softer material. The area of contact between the asperity and the deformed material is approximated by its chord and is assumed to be confined ahead of the lowest point D of the circle. The chord approximation allows the slipline field and associated hodograph previously established by Challen and Oxley [2] for wedge shape asperities to be used. In this last model, the asperity angle α is a constant parameter and only the length of the interface ED and hence the scale of the plastic zone increases with the normal load N . For a circular asperity of radius R , α and ED are now interrelated and depend on the geometrical and loading conditions. Introducing this last feature and defining the strength of the interfacial film by the Tresca factor $f = \frac{\tau}{k}$, where τ is the shear strength of the interfacial film and k is the shear flow stress of the soft material, Challen and Oxley [2]

developed the following equations:

$$\eta = \arcsin\left[\frac{\sin(\alpha)}{\sqrt{(1-f)}}\right] \quad (\text{B.1})$$

$$\Phi = \frac{1}{2} \arccos(f) - \alpha \quad (\text{B.2})$$

$$\frac{DE}{R} = 2 \sin(\alpha) \quad (\text{B.3})$$

from the slipline field geometry analysis, where η and Φ are two angles describing the slipline field and

$$\frac{F}{kR} = 2 \sin(\alpha) [\cos(\alpha + 2\Phi) + (1 + 2(\frac{\pi}{4} + \Phi - \eta)) \sin(\alpha)] \quad (\text{B.4})$$

$$\frac{N}{kR} = 2 \sin(\alpha) [\sin(\alpha + 2\Phi) + (1 + 2(\frac{\pi}{4} + \Phi - \eta)) \cos(\alpha)] \quad (\text{B.5})$$

$$\mu = \frac{[\cos(\alpha + 2\Phi) + [1 + 2(\frac{\pi}{4} + \Phi - \eta)] \sin(\alpha)]}{[\sin(\alpha + 2\Phi) + [1 + 2(\frac{\pi}{4} + \Phi - \eta)] \cos(\alpha)]} \quad (\text{B.6})$$

from the stress analysis where F and N are the frictional and normal forces per unit width and μ the resulting friction coefficient.

This steady-state field is associated with low load conditions, and hence low angle α of the chord. For high angles α , a double chord model was proposed where a continuous chip formation is considered. It is not presented here because only the rubbing regime is investigated in the present work.

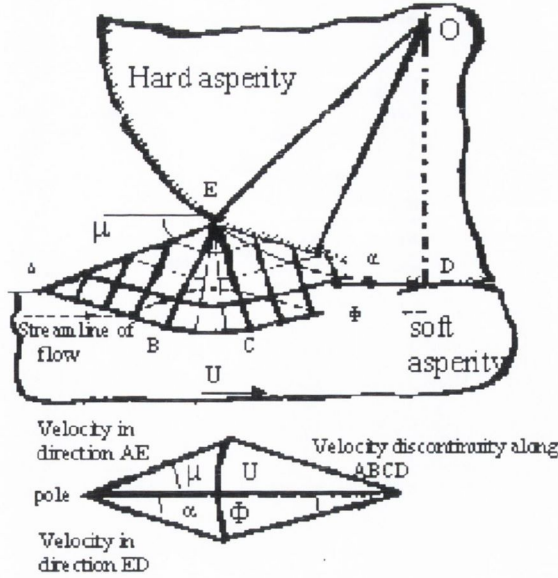


Figure B.1: Chord approximation model developed by Challen and Oxley [1]

B.2 The developed chord model [3]

The chord approximation model has been developed for the configuration where the lowest point in contact D between the circular asperity and the softer material is not on the center line of the circle, as shown in figure (B.2). The parameter β_c defines the angle between the radius OD and the center line as shown in figure (B.2). The hodograph associated with the slipline field is equivalent to the one associated with Challen and Oxley's model [1]. The new geometrical relation between the chord ED , the radius R of the cylinder and the two angles α and β_c is as follows:

$$\frac{DE}{R} = 2 \sin(\alpha - \beta) \quad (\text{B.7})$$

Equations (B.1), (B.2), (B.6) can still be used but (B.4) and (B.5) become:

$$\frac{F}{kR} = 2 \sin(\alpha - \beta_c) [\cos(\alpha + 2\Phi) + (1 + 2(\frac{\pi}{4} + \Phi - \eta)) \sin(\alpha)] \quad (\text{B.8})$$

$$\frac{N}{kR} = 2 \sin(\alpha - \beta_c) [\sin(\alpha + 2\Phi) + (1 + 2(\frac{\pi}{4} + \Phi - \eta)) \cos(\alpha)] \quad (\text{B.9})$$

For a given normal load per unit width N , the associated chord angle α is relatively higher for the developed model than the original one, and hence associated with higher friction coefficients. This change can be seen in figure (B.3) where the dotted lines represent the variations of μ with (N/kR) for $f = 0$ and various values of the parameter β_c . The value of $\beta_c = 0$ corresponds to the chord approximation model [1].

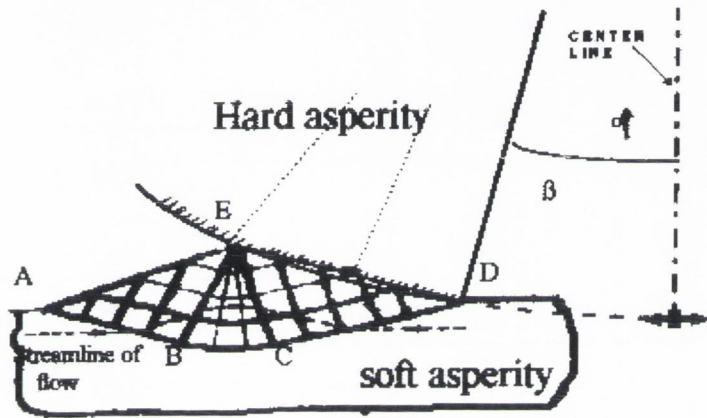


Figure B.2: The developed chord model

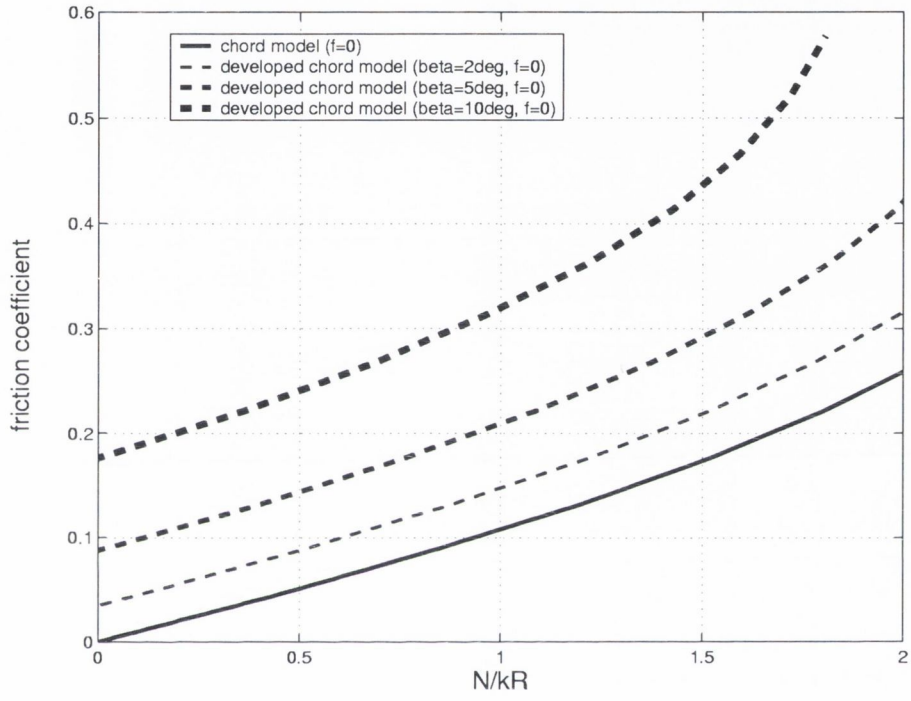


Figure B.3: Variation of μ with N/kR for the chord model [1] and the developed chord model for different β_c and $f = 0$

Appendix C

Geometrical properties of a slipline field - Stress and velocity boundary value problems [4, 5]

C.0.1 Hencky's first theorem

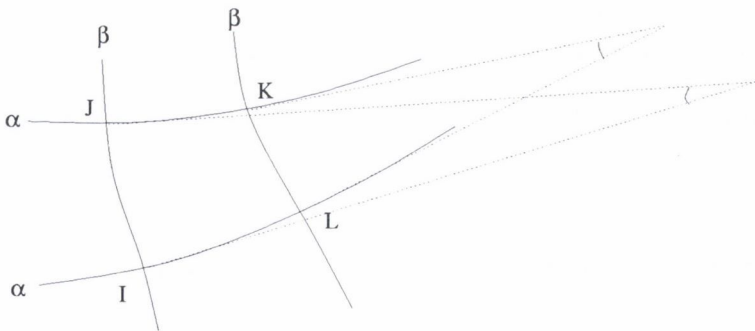


Figure C.1: Typical slipline field, demonstrating Hencky's first theorem

Consider a curvilinear quadrilateral IJKL, as shown in figure (C.1) bounded by two α lines, (IL) and (JK), and by two β lines, (IJ) and (LK). From the Hencky stress equations, it follows:

$$p_K - p_I = (p_K - p_J) + (p_J - p_I) = 2k(2\phi_J - \phi_K - \phi_I) \quad (\text{C.1})$$

and

$$p_K - p_I = (p_K - p_L) + (p_L - p_I) = 2k(\phi_K - \phi_I - 2\phi_L) \quad (\text{C.2})$$

therefore,

$$\phi_K - \phi_L = \phi_J - \phi_I \quad (\text{C.3})$$

Equation (C.3) is known as Hencky's first theorem. It states that if we pass from one slipline to another of the same family along any intersecting slipline, the angle turned through and the change in pressure are constant.

C.1 Second boundary value problem

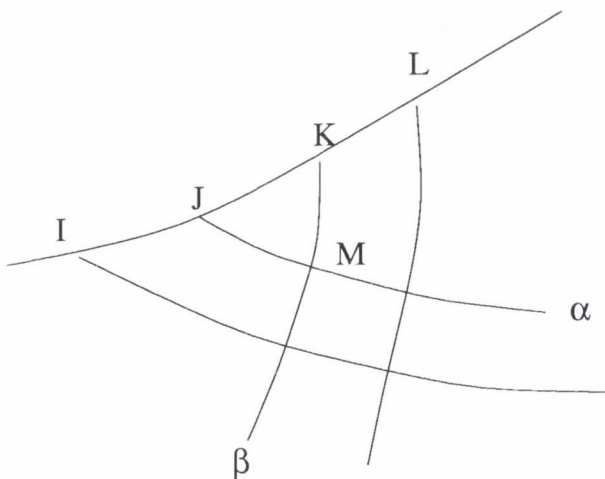


Figure C.2: Second boundary value problem

It concerns the determination of the slipline field defined by a curve (IJKL), (the stress free surface for example), as shown in figure (C.2) along which the stresses are known. Since the stress components are known, p and ϕ are known.

If J and K are two adjacent points on the curve (figure (C.2)), the nodal point M, which is the intersection of the α line through J and the β line through K, can be obtained approximately as follows:

1. from the Hencky equations, the value of ϕ at M is:

$$\phi_M = \frac{1}{4k}(p_J - p_K) + \frac{1}{2}(\phi_J + \phi_K) \quad (\text{C.4})$$

2. the coordinates of M can be found by replacing the segments of sliplines (JM) and (MK) by straight lines passing through J and K that make angles ϕ and $(\phi' + \frac{\pi}{2})$ with the positive x-direction where:

$$\phi = \frac{\phi_M + \phi_J}{2} \quad (\text{C.5})$$

and

$$\phi' = \frac{\phi_K + \phi_M}{2}. \quad (\text{C.6})$$

If both components of velocity are given along the curve (IJKL), the problem is the same as for the first boundary value problem: the component u_M and v_M can be determine as follows:

$$(u_J - u_M) - \frac{1}{2}(v_J + v_M)(\phi_J - \phi_M) = 0 \quad (\text{C.7})$$

$$(v_K - v_M) + \frac{1}{2}(v_K + v_M)(\phi_K - \phi_M) = 0 \quad (\text{C.8})$$

C.2 Third boundary value problem

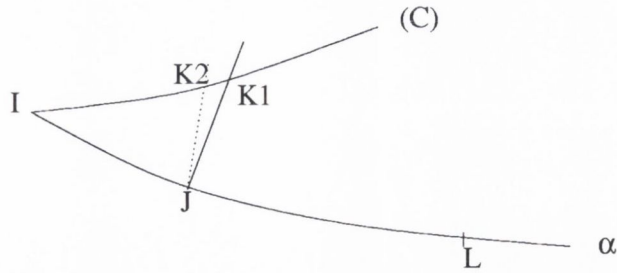


Figure C.3: Third boundary value problem

The third boundary value problem arises when a slipline (IL) and a curve (C), along which ϕ but not p is known, are given as shown in figure (C.3). The procedure to obtain the point K, intersection between the β line going through J (point adjacent to I) and the curve (C) is as follows:

1. K_1 is obtained by constructing a straight line in the β direction going through J to intersect (C).
2. a further straight line through J to meet (C) in K_2 is drawn so that it makes an angle $(\phi + \frac{\pi}{2})$ with the positive x-direction where $\phi = \frac{1}{2}(\phi_J + \phi_{K_1})$.

This procedure is repeated until the desired accuracy is obtained.

If both components of velocity are given along the α line (IL) together with a boundary condition along the curve (C), and if I is not a singularity, the components u_K and v_K are obtained by solving the following system of equations:

$$\left. \begin{aligned} v_J - v_K &= \frac{1}{2}(u_J + u_K)(\phi_J - \phi_K) \\ \text{function}(u_K, v_K) &= 0 \end{aligned} \right\} \quad (\text{C.9})$$

Appendix D

Optimisation of the numerical solution with an ellipse

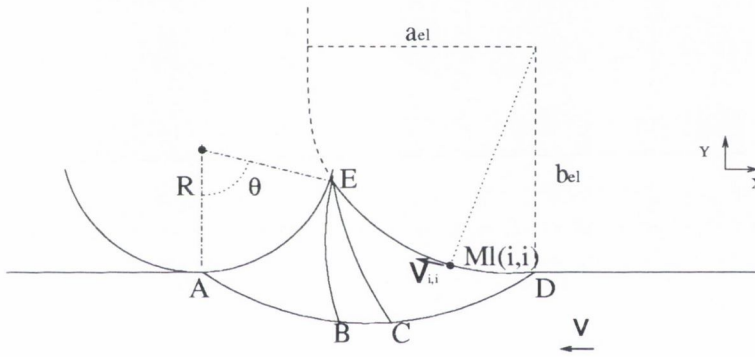


Figure D.1: Boundary conditions for the ellipse

To correct the shape of the free surface, the slope of the velocity vector β_E , (with $\beta_E = \beta_{calc}(n)$), computed in E becomes the tangent to the ellipse at E (refer to figure (D.1)). An ellipse is thus defined, whose radii a_{el} and b_{el} can be expressed as follows:

$$b_{el} = \frac{Y_E^2 + (X_E - X_D)^2 Y_E / c}{2Y_E + (X_E - X_D)^2 / c} \quad (D.1)$$

$$a_{el} = \frac{\sqrt{|c|} b_{el}}{\sqrt{|Y_E - b_{el}|}} \quad (D.2)$$

$$\text{with } c = \frac{-(X_E - X_D)}{\tan(\beta_E)} \quad (D.3)$$

The new boundary conditions along the ellipse (ED) referring to figure (D.1), are:

$$Xl_{i,i} = -(i-1) \frac{X_D - X_E}{n-1} + X_D \quad (D.4)$$

$$Yl_{i,i} = -b_{el} \sqrt{1 - \frac{(Xl_{i,i} - X_D)^2}{a_{el}^2}} + b_{el} \quad (D.5)$$

$$\phi_{i,i} = \frac{\pi}{4} + \arctan\left[\frac{(X_D - X_{i,i})b_{el}^2}{(Y_{i,i} - b_{el})a_{el}^2}\right] \quad (D.6)$$

Appendix E

Calculation of stresses along the interface and of the friction coefficient μ

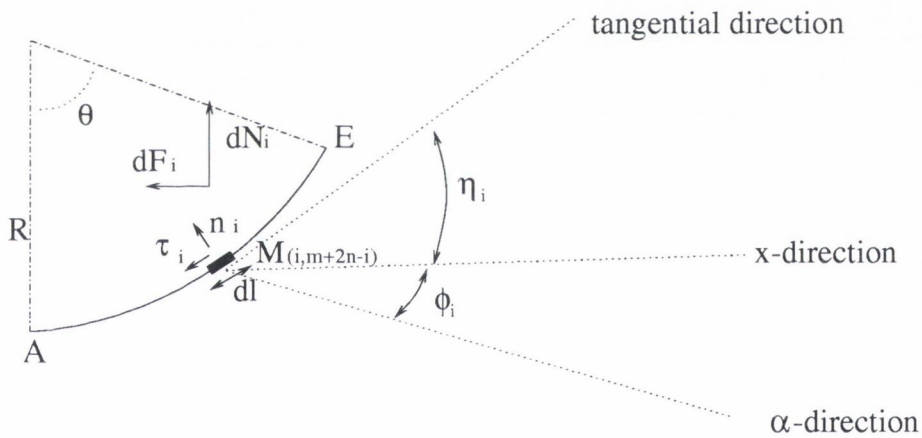


Figure E.1: Calculation of stresses at the interface

The stresses n_i and τ_i at the point $M_{i,m+2n-i}$ of the interface, as shown in figure (E.1) were computed from $p_{i,m+2n-i}$ and k as follows:

$$n_i = p_{i,m+2n-i} + k \sin[2(\eta_i - \phi_{i,m+2n-i})] \quad (\text{E.1})$$

$$\tau_{i,m+2n-i} = k \cos[2(\eta_i - \phi_{i,m+2n-i})] \quad (\text{E.2})$$

The elemental forces dN_i and dF_i acting on the elemental line dl , with $dl = R.\theta/(n - 1)$ were computed as follows:

$$dN_i = [n_i \cos(\eta_i) - \tau_i \sin(\eta_i)].dl \quad (\text{E.3})$$

$$dF_i = [n_i \sin(\eta_i) + \tau_i \cos(\eta_i)].dl \quad (\text{E.4})$$

The resulting forces per unit width N and F were then obtained by integrating the elemental forces along the interface as follows:

$$N = \sum_{i=1}^n dN_i \quad (\text{E.5})$$

$$F = \sum_{i=1}^n dF_i \quad (\text{E.6})$$

Finally the friction coefficient was obtained as follows:

$$\mu = F/N \quad (\text{E.7})$$

Appendix F

Checks on plastic works

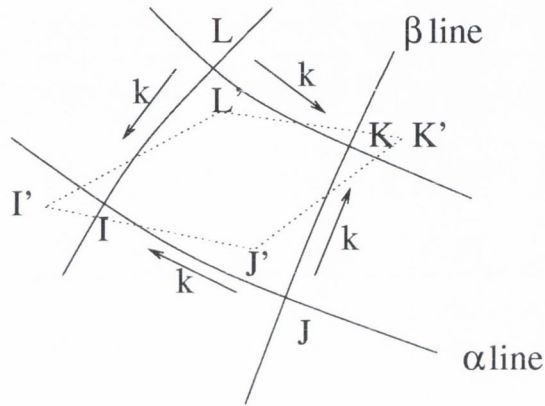


Figure F.1: An element of slipline field showing correct material deformations

Checks were made to ensure that the material deforms in the “correct way” under the action of the applied shear stresses. In figure (F.1), the material should deform in the manner shown under the action of the shear stresses. To ensure that this is the case, the velocity of point K relative to point I is checked to ensure that it has a positive component in the direction from I to K. Similarly the velocity of J relative to L is checked to ensure it has a negative component in the direction from L to J.

The velocities u, v at all nodal points in the slipline field were transformed to x and y component values using,

$$V_x = u \cos(\phi) - v \sin(\phi) \quad (\text{F.1})$$

$$V_y = u \sin(\phi) + v \cos(\phi) \quad (\text{F.2})$$

Along the free surface, to ensure that the plastic work done is positive, a_1 must be positive. The equation used to calculate a_1 is as follows, referring to figure (F.2):

$$a_1 = Vx_{J1}(Y_{K1} - Y_{I1}) - Vy_{J1}(X_{K1} - X_{I1}) \quad (\text{F.3})$$

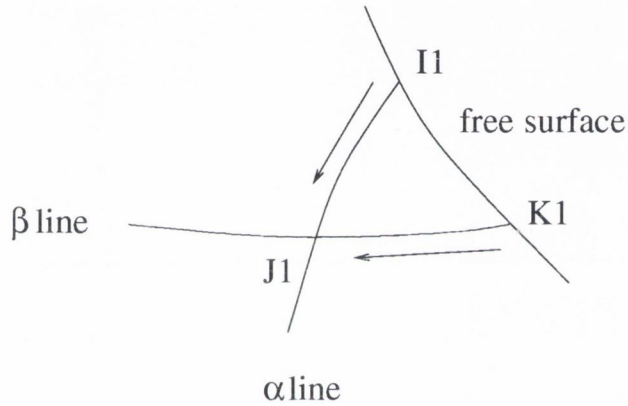


Figure F.2: Computation of material deformation directions along the free surface

Along the interface, to ensure that the plastic work done is positive, a_2 must be positive. The equation used to calculate a_2 is as follows, referring to figure (F.3):

$$a_2 = Vx_{K2}(Y_{I2} - Y_{J2}) - Vy_{J2}(X_{J2} - X_{I2}) \quad (\text{F.4})$$

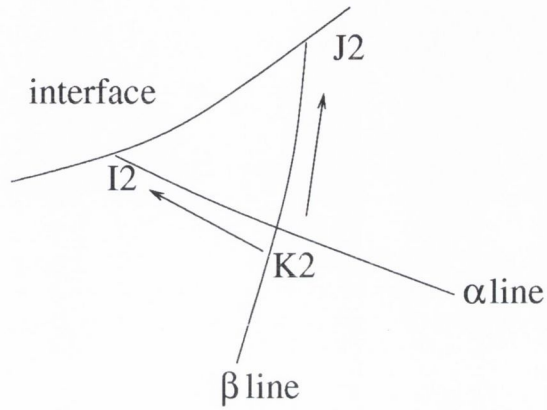


Figure F.3: Computation of material deformation directions along the interface

Anywhere else in the field, to ensure that the plastic work done is positive, a_3 must be positive. The equation used to calculate a_3 is as follows, referring to figure (F.4):

$$a_3 = (Vy_{J3} - Vy_{L3})(Y_{J3} - Y_{L3}) - (Vx_{J3} - Vx_{L3})(X_{J3} - X_{L3}) \quad (\text{F.5})$$

$$a_4 = (Vy_{I3} - Vy_{K3})(Y_{K3} - Y_{I3}) - (Vx_{K3} - Vx_{I3})(X_{K3} - X_{I3}) \quad (\text{F.6})$$

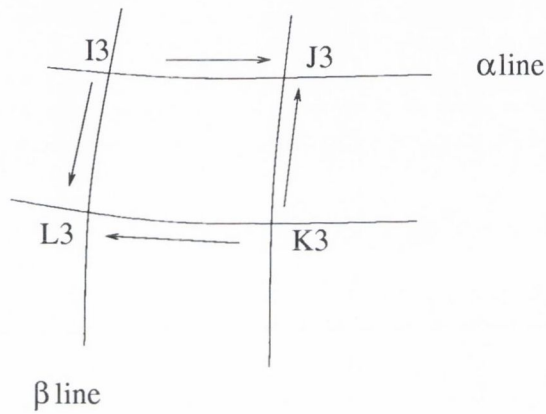


Figure F.4: Computation of material deformation directions in the field

Appendix G

Strain maps

This appendix shows a series of maps and associated data, issuing from our numerical model that give the evolution of the strain pattern for a wide range of conditions.

The data associated with the maps shown in chapter (4) are also given.

It should be noted that $h/h_{max}=0$ corresponds to the free surface and $h/h_{max}=-1$ corresponds to the bottom of the deformed layer.

G.1 Evolution of the angle of the interface θ versus (N/kR) for different values of the Tresca factor f

The map was given in chapter (4).

θ	N_0/kR	N_1/kR	N_2/kR	N_3/kR	N_4/kR	N_5/kR
0.05	0.252	0.2460	0.240	0.233	0.226	0.217
0.10	0.492	0.4800	0.467	0.453	0.437	0.418
0.15	0.719	0.7000	0.679	0.656	0.630	0.599
0.20	0.931	0.9040	0.874	0.840	0.801	0.754
0.25	1.130	1.0900	1.050	1.000	0.945	0.873
0.30	1.300	1.2500	1.200	1.130	1.050	0.926
0.35	1.450	1.3900	1.320	1.230	1.100	
0.40	1.580					
0.50	1.74					

Table G.1: Evolution of the angle of the interface θ versus (N/kR) for different values of the Tresca factor f

where N_1/kR corresponds to N/kR for $f = 0.1$.

G.2 Evolution of the friction coefficient μ with (N/kR) for different values of the Tresca factor f

N_0/kR	$\mu_0 * 10$	N_1/kR	$\mu_1 * 10$	N_2/kR	$\mu_2 * 10$	N_3/kR	$\mu_3 * 10$
0.252	0.252	0.2460	0.455	0.240	0.669	0.233	0.896
0.492	0.508	0.4800	0.718	0.467	0.938	0.453	1.17
0.719	0.769	0.7000	0.985	0.679	1.220	0.656	1.46
0.931	1.030	0.9040	1.260	0.874	1.500	0.840	1.76
1.130	1.300	1.0900	1.540	1.050	1.790	1.000	2.07
1.300	1.570	1.2500	1.820	1.200	2.090	1.130	2.40
1.450	1.850	1.3900	2.110	1.320	2.400	1.230	2.74

Table G.2: Evolution of the friction coefficient μ with (N/kR) for different values of the Tresca factor f

where (N_1/kR) and μ_1 corresponds to (N/kR) and μ for $f = 0.1$.

N_4/kR	$\mu_4 * 10$	N_5/kR	$\mu_5 * 10$
0.226	1.140	0.2170	1.410
0.437	1.430	0.4180	1.710
0.630	1.730	0.5990	2.040
0.801	2.050	0.7540	2.390
0.945	2.390	0.8730	2.790
1.050	2.760	0.9260	3.270
1.100	3.180		

Table G.3: Evolution of the friction coefficient μ with (N/kR) for different values of the Tresca factor f

G.3 Evolution of the depth of the deformed layer (h_{max}/R) versus (N/kR) for different values of the Tresca factor f .

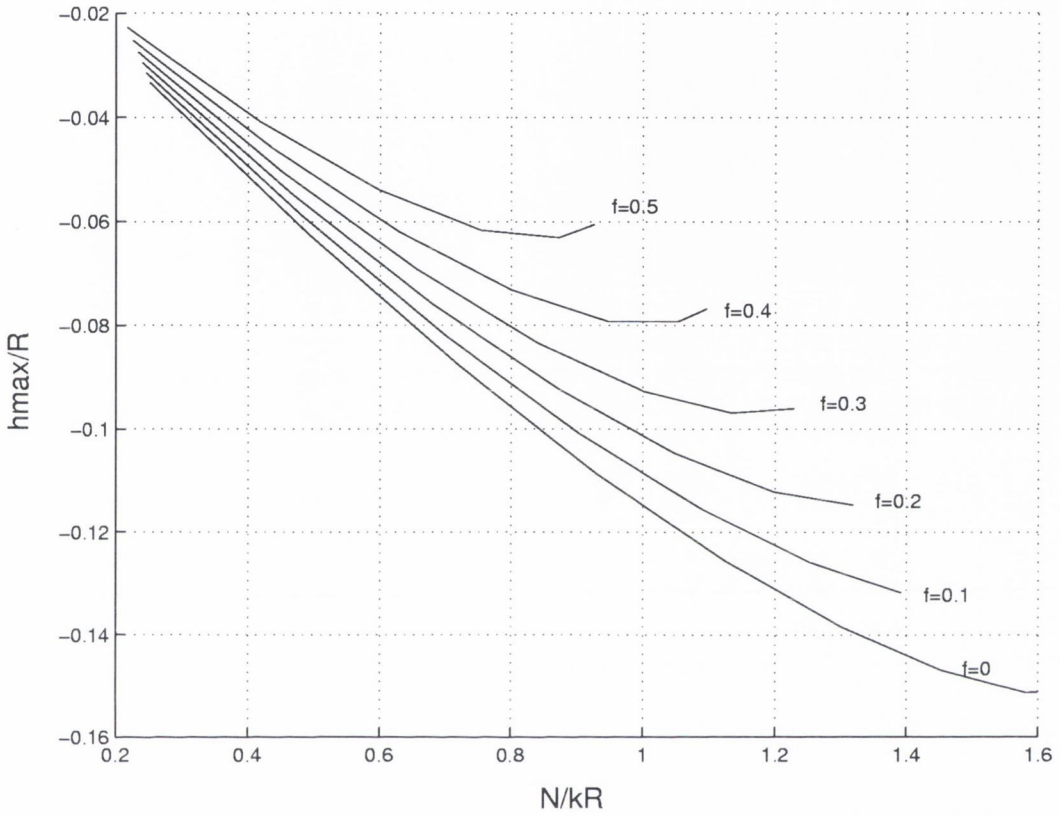


Figure G.1: Evolution of the depth of the deformed layer (h_{max}/R) versus (N/kR) for different values of the Tresca factor f

θ	h_{0MAX}/R	h_{1MAX}/R	h_{2MAX}/R	h_{3MAX}/R	h_{4MAX}/R	h_{5MAX}/R
0.05	-0.00333	-0.00314	-0.00295	-0.00274	-0.00252	-0.00227
0.10	-0.00625	-0.00587	-0.00548	-0.00505	-0.00459	-0.00408
0.15	-0.00876	-0.00819	-0.00758	-0.00691	-0.00620	-0.00539
0.20	-0.01090	-0.01010	-0.00924	-0.00833	-0.00732	-0.00617
0.25	-0.01260	-0.01160	-0.01050	-0.00927	-0.00791	-0.00631
0.30	-0.01380	-0.01260	-0.01120	-0.00969	-0.00793	-0.00606
0.35	-0.01470	-0.01320	-0.01150	-0.00960	-0.00767	
0.40	-0.01510					
0.50	-0.01500					

Table G.4: Evolution of the depth of the deformed layer (h_{max}/R) versus θ for different values of the Tresca factor f

where (h_{1MAX}/R) corresponds to (h_{MAX}/R) for $f = 0.1$.

G.4 Evolution of the shear strain (γ_{xy}) versus the depth (h/h_{max}) for $f = 0.3$ and for different loads (N/kR).

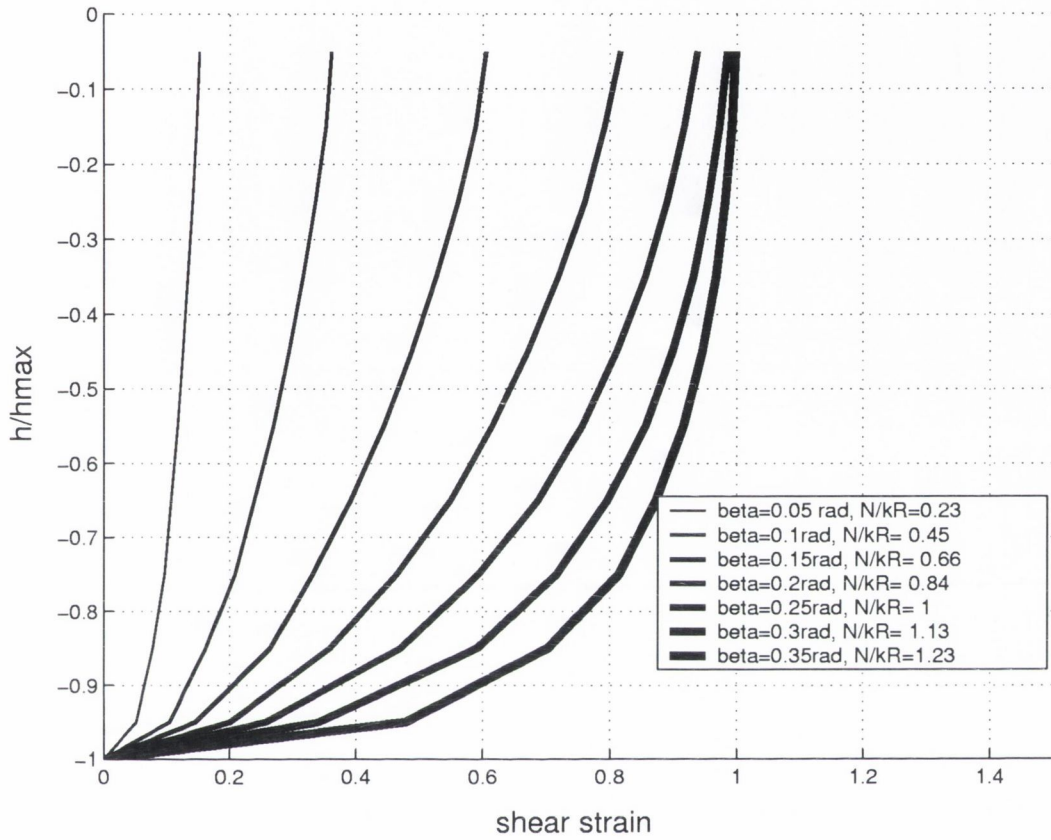


Figure G.2: Evolution of the shear strain γ_{xy} versus the depth (h/h_{max}) for $f = 0.3$ and for different loads (N/kR)

h/h_{MAX}	$\gamma_{xy} * 10$	$\gamma_{xy} * 10$	$\gamma_{xy} * 10$	$\gamma_{xy} * 10$
	N/kR=0.23	N/kR=0.45	N/kR=0.66	N/kR=0.84
-0.05	1.53	3.61	6.05	8.16
-1.50	1.48	3.52	5.88	7.91
-2.50	1.42	3.36	5.60	7.61
-3.50	1.35	3.16	5.26	7.19
-4.50	1.26	2.94	4.88	6.71
-5.50	1.18	2.70	4.44	6.15
-6.50	1.08	2.39	3.91	5.49
-7.50	0.97	2.09	3.31	4.64
-8.50	0.79	1.63	2.64	3.59
-9.50	0.52	1.05	1.47	2.01
-1.00	0.00	0.00	0.000	0.00

Table G.5: Evolution of the shear strain γ_{xy} versus the depth (h/h_{max}) for $f = 0.3$ and for different angles (N/kR)

h/h_{MAX}	$\gamma_{xy} * 10$	$\gamma_{xy} * 10$	$\gamma_{xy} * 10$
	N/kR=1.00	N/kR=1.13	N/kR=1.23
-0.05	9.37	9.85	9.97
-1.50	9.16	9.72	9.92
-2.50	8.89	9.54	9.81
-3.50	8.55	9.31	9.67
-4.50	8.10	8.98	9.45
-5.50	7.57	8.56	9.15
-6.50	6.88	7.96	8.72
-7.50	5.93	7.17	8.14
-8.50	4.71	5.92	7.03
-9.50	2.58	3.42	4.78
-1.00	0.00	0.00	0.00

Table G.6: Evolution of the shear strain γ_{xy} versus the depth (h/h_{max}) for $f = 0.3$ and for different angles (N/kR)

G.5 Evolution of the shear strain (γ_α) versus the depth (h/h_{max}) for $f = 0.3$ and for different loads (N/kR).

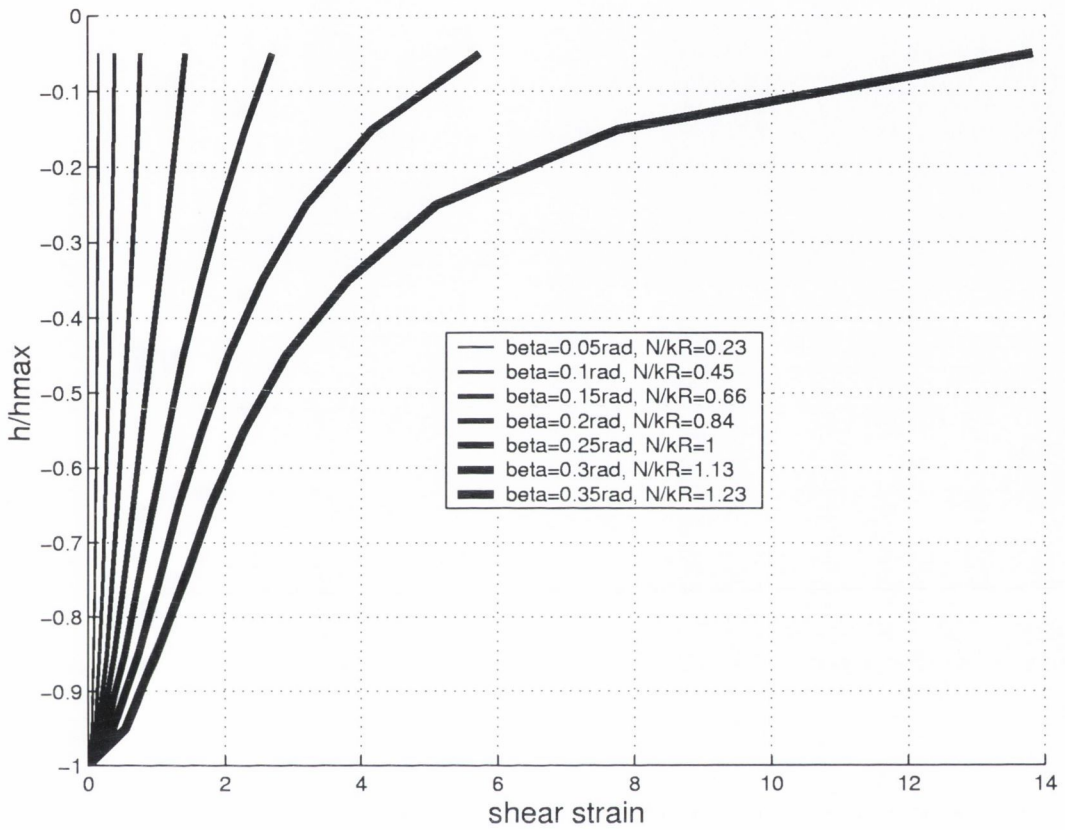


Figure G.3: Evolution of the shear strain γ_α versus the depth (h/h_{max}) for $f = 0.3$ and for different loads (N/kR)

h/h_{MAX}	$\gamma_\theta * 10$	$\gamma_\theta * 10$	$\gamma_\theta * 10$	$\gamma_\theta * 10$
	N/kR=0.23	N/kR=0.45	N/kR=0.66	N/kR=0.84
-0.05	1.55	3.87	7.60	14.1
-1.50	1.50	3.76	7.27	12.9
-2.50	1.43	3.56	6.76	11.7
-3.50	1.36	3.33	6.19	10.4
-4.50	1.28	3.07	5.58	9.05
-5.50	1.19	2.80	4.95	7.79
-6.50	1.08	2.46	4.25	6.57
-7.50	0.98	2.13	3.51	5.24
-8.50	0.79	1.65	2.74	3.85
-9.50	0.52	1.06	1.48	2.05
-1.00	0.00	0.00	0.00	0.00

Table G.7: Evolution of the shear strain γ_θ versus the depth (h/h_{max}) for $f = 0.3$ and for different angles (N/kR)

h/h_{MAX}	$\gamma_\theta * 10$	$\gamma_\theta * 10$	$\gamma_\theta * 10$
	N/kR=1.00	N/kR=1.13	N/kR=1.23
-0.05	26.9	57.2	138.0
-1.50	22.9	41.5	77.6
-2.50	19.5	31.9	50.9
-3.50	16.5	25.4	38.0
-4.50	13.8	20.4	28.9
-5.50	11.6	16.6	22.7
-6.50	9.47	13.2	17.9
-7.50	7.37	10.3	14.0
-8.50	5.34	7.34	9.89
-9.50	2.67	3.64	5.45
-1.00	0.00	0.00	0.00

Table G.8: Evolution of the shear strain γ_θ versus the depth (h/h_{max}) for $f = 0.3$ and for different angles (N/kR)

G.6 Evolution of the maximum shear strains (γ_{xyMAX}) and ($\gamma_{\theta MAX}$) versus the load (N/kR) for different f .

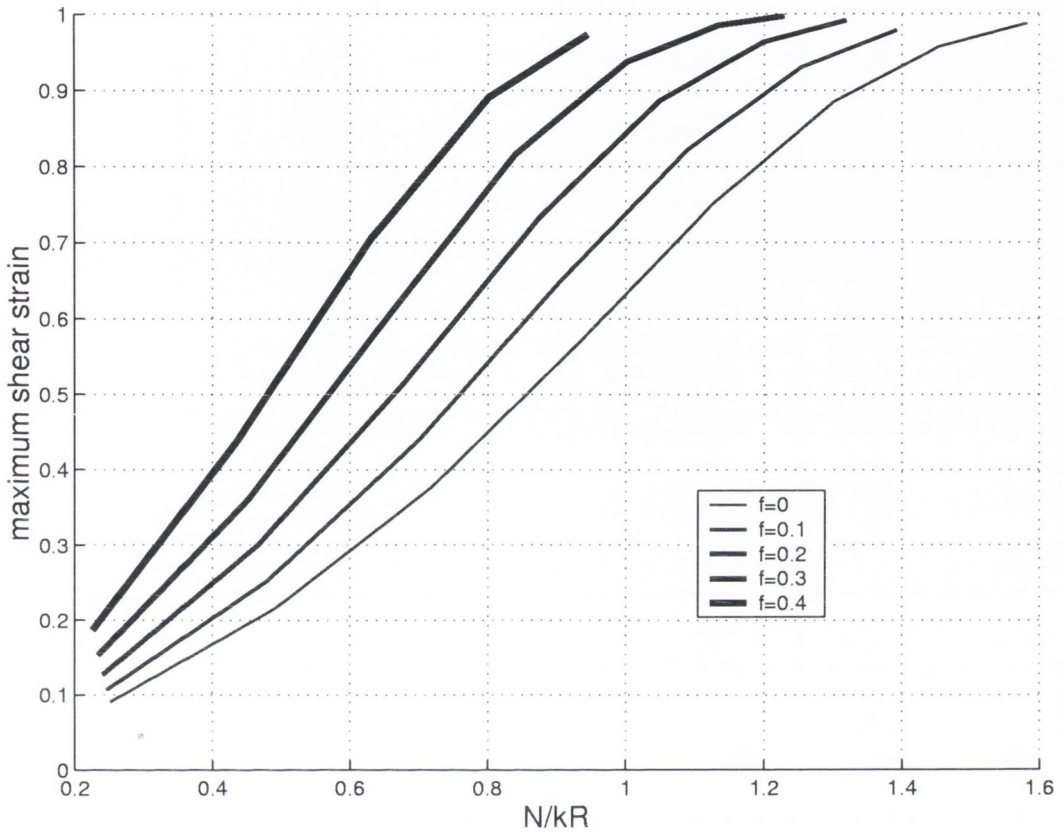


Figure G.4: Evolution of the maximum shear strain (γ_{xyMAX}) versus the load (N/kR) for different f

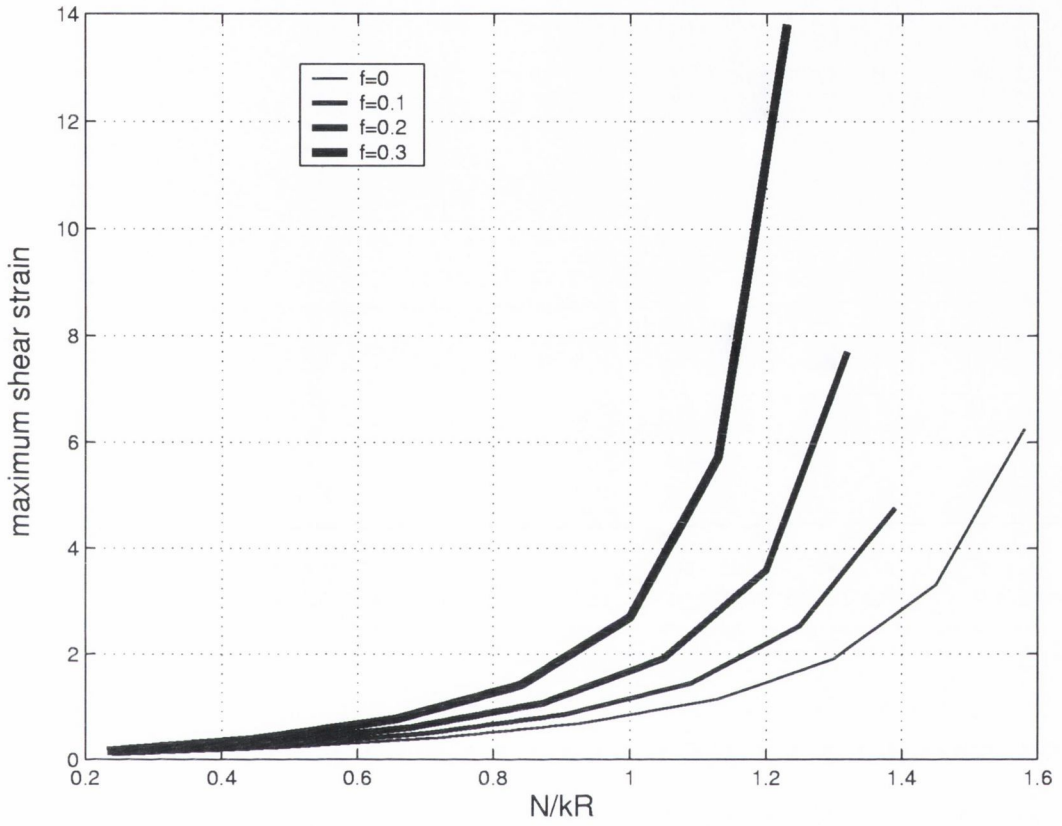


Figure G.5: Evolution of the maximum shear strain ($\gamma_{\alpha MAX}$) versus the load (N/kR) for different f

N/kR	$\gamma_{0xyMAX} * 10$	$\gamma_{0\theta MAX} * 10$
0.252	0.90	0.91
0.492	2.16	2.21
0.719	3.78	4.08
0.931	5.66	6.87
1.130	7.51	10.1
1.300	8.85	19.0
1.450	9.57	33.1
1.580	9.87	62.5

Table G.9: Evolution of the maximum shear strain (γ_{xyMAX}) and ($\gamma_{\theta MAX}$) versus the load (N/kR) for $f = 0$

N/kR	$\gamma_{1xyMAX} * 10$	$\gamma_{1\theta MAX} * 10$
0.246	1.07	1.07
0.480	2.52	2.61
0.700	4.40	4.90
0.904	6.48	8.50
1.130	8.22	1.44
1.300	9.30	2.53
1.450	9.79	4.76

Table G.10: Evolution of the maximum shear strain (γ_{xyMAX}) and ($\gamma_{\theta MAX}$) versus the load (N/kR) for $f = 0.1$

N/kR	$\gamma_{2xyMAX} * 10$	$\gamma_{2\theta MAX} * 10$
0.240	1.27	1.28
0.467	3.01	3.15
0.679	5.17	6.04
0.874	7.32	10.7
1.050	8.86	19.1
1.200	9.63	35.9
1.320	9.92	77.0

Table G.11: Evolution of the maximum shear strain (γ_{xyMAX}) and ($\gamma_{\theta MAX}$) versus the load (N/kR) for $f = 0.2$

N/kR	$\gamma_{3xyMAX} * 10$	$\gamma_{3\theta MAX} * 10$
0.233	1.53	1.55
0.453	3.61	3.87
0.656	6.05	7.60
0.840	8.16	14.1
1.000	9.37	26.9
1.130	9.85	57.2
1.230	9.97	138.0

Table G.12: Evolution of the maximum shear strain (γ_{xyMAX}) and ($\gamma_{\theta MAX}$) versus the load (N/kR) for $f = 0.3$

Appendix H

Determination of the Tresca factor f

H.1 Test procedure

The Tresca factor f is an input of the slipline field model. It depends on the materials used and on the lubricant (in our situation, on the triplet C.B.N. / STEARIC ACID / ALUMINIUM and on the triplet C.B.N. / STEARIC ACID / COPPER). In order to assess the value of f in an independent way, friction tests were performed with C.B.N. wedges of various angles α , under the same lubrication conditions as for the cylinder tests (chapter (5)) for both materials.

A picture of one of the wedges used is shown in figure (H.1). The wedge is 3.15mm in width. The set-up and procedure are the same as those described in chapter (5). Several tool holders were made with different orientations to get the desired attack angle α . The applied load W were within the range 400 – 600N.

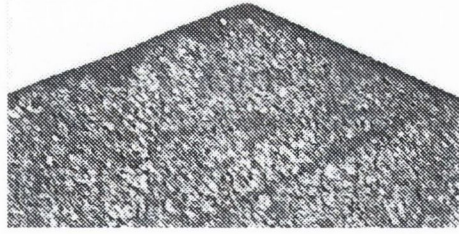


Figure H.1: Wedge in C.B.N.

H.2 Friction results

Measured friction coefficients are compared to the predictions of the wedge model in figures (H.2) and (H.3) for aluminium and copper respectively.

The chosen value of f was the one which best fits the experimental data. A value of $f = 0.05$ was obtained this way for both materials.

However, deviations from theory can be observed for the lowest and highest attack angles tested. These discrepancies can be firstly explained by the lack of accuracy of the attack angle measurement. This was done by direct measurements on the tool with a microscope after each test. The surface of the tool were not perfectly regular and the measurements were not repeatable with a high accuracy. For the lowest loads, these deviations can also be attributed to experimental errors as the set-up was not accurate enough for small loads. It might also be due to elastic effects [8, 63, 64]. For the highest loads, a change of regime (sort of cutting as continuous removal of material) was observed for the aluminium alloy, which can explain the deviations from theory. The copper was tested for only three angles α .

Figures (H.4) and (H.5) show how the detached particles lie on the wedge after a test on aluminium and copper respectively. For both figures, the entry of the contact is on the left:

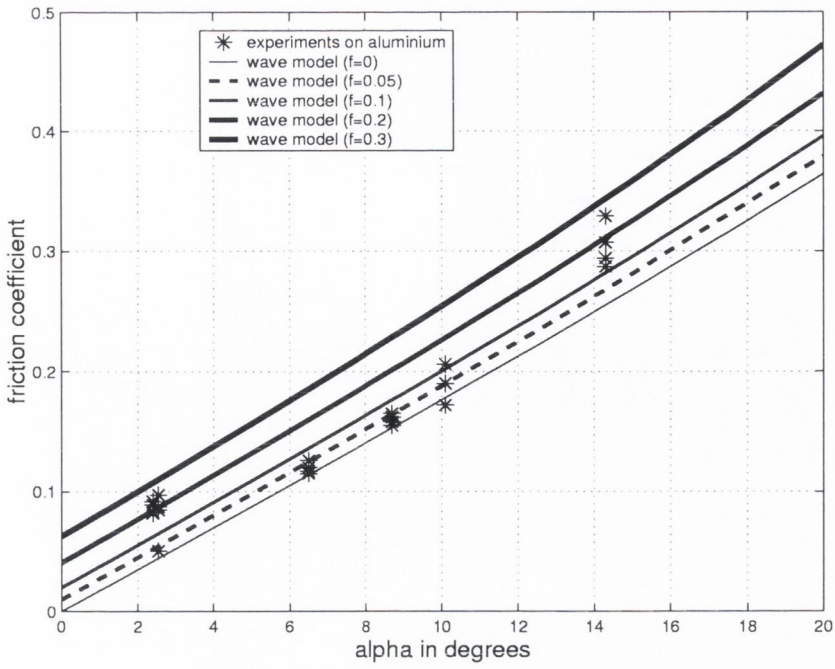


Figure H.2: Experiments with wedge-shaped asperities on aluminium

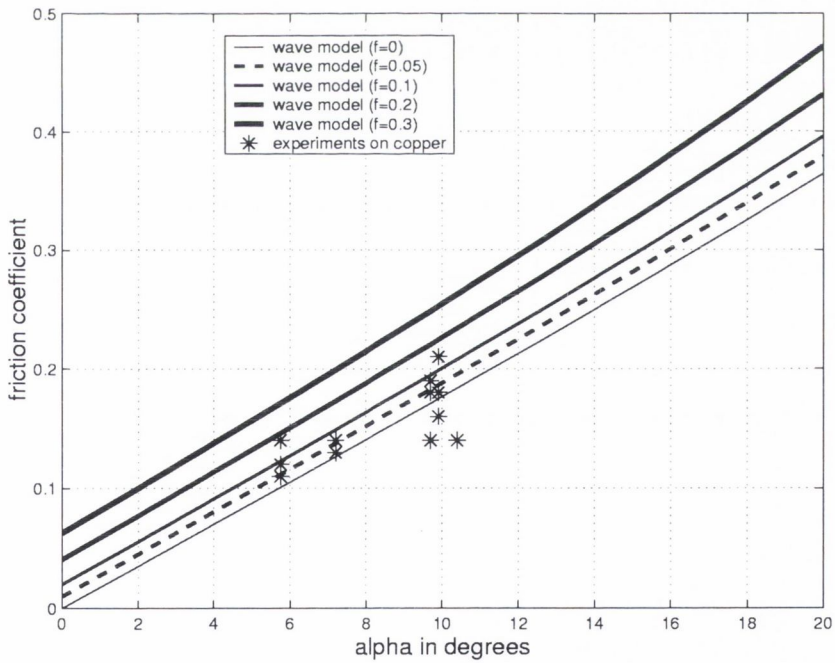


Figure H.3: Experiments with wedge-shaped asperities on copper

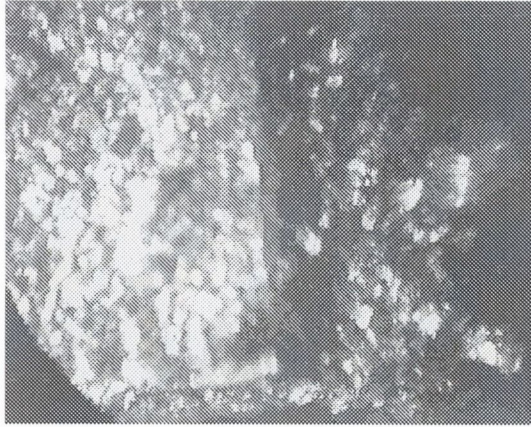


Figure H.4: Particle organisation inside the contact area on the wedge - Aluminium - $W = 500N$

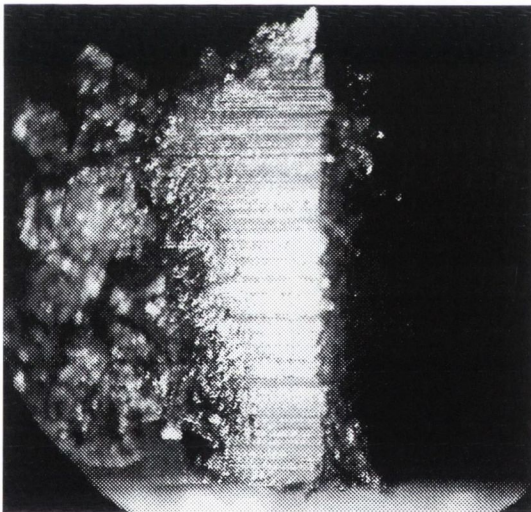


Figure H.5: Particle organisation inside the contact area on the wedge - Copper - $W = 500N$

H.3 Data

H.3.1 Data for aluminium

α in degrees	μ
2.4	0.0920
2.4	0.0890
2.4	0.0830
2.4	0.0820
6.5	0.1170
6.5	0.1150
6.5	0.1200
6.5	0.1260
8.7	0.1650
8.7	0.1550
8.7	0.1620
8.7	0.1580
10.1	0.1720
10.1	0.1900
10.1	0.1900
10.1	0.2060
2.55	0.0847
2.55	0.0876
2.55	0.0506
2.55	0.0971
14.3	0.2940
14.3	0.2870
14.3	0.3290
14.3	0.3070

Table H.1: Data for the wedge tests - Aluminium

H.3.2 Data for copper

α in degrees	μ
5.75	0.1200
5.75	0.1100
5.75	0.1400
9.91	0.1800
9.91	0.2100
9.91	0.1600
10.4	0.1400
10.4	0.1400
10.4	0.1400
18.95	0.3200
18.95	0.3180
7.2	0.1400
7.2	0.1300
9.7	0.1900
9.7	0.1400
9.7	0.1800

Table H.2: Data for the wedge tests - Copper

Appendix I

Velocity accommodation mechanism in a three body contact

In the third body approach [71, 12, 72, 98, 9], it is considered that the velocity difference between first bodies is accommodated across the interface which means that the interface possesses its own velocity field and dynamics. Progress in understanding and modelling friction in such situations requires paste dynamics studies and an identification of both modes (how friction is generated) and sites (where is friction generated) of velocity accommodation.

Figure (I.1) is a simple three body contact model. It includes the two first bodies or rubbing specimen, the two third body/first body interfaces or screen, which have their own specific composition and the third body bulk.

The manner in which the difference in velocity between rubbing solids is accommodated across the interface is defined here as the velocity accommodation mechanism. Velocity accommodation mechanisms, which governs friction and wear, have been identified during visualisation tests. Figure (I.1) shows that in a three body contact, the velocity can be accommodated at five different sites S_i which include the two first bodies S_1 and S_2 , the two screens S_3 and S_4 , and the third body bulk S_5 , and according to four different modes M_j

at each site which are the elastic M_1 , the rupture M_2 , the shear M_3 and the rolling M_4 modes. Thus 20 velocity accommodation mechanisms can be encountered. Each mechanism is identified by one $S_i M_j$ code. $S_3 M_3$ for instance signifies that the velocity is accommodated in the third body bulk through shear.

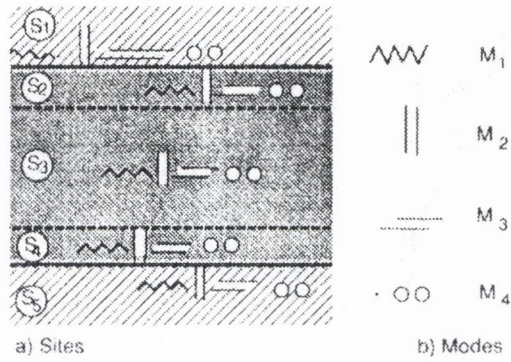


Figure I.1: Velocity accommodation in a three-body contact. Taken from [12]

Appendix J

Presentation of the finite element models

J.0.3 Description of the models

The finite element models were constructed using commercial software (ANSYS 5.4) to represent a hard cylinder and a hard cut cylinder indenting and sliding over a softer metal.

The models are shown in figures (J.1) and (J.2). The dimensions of both models are shown in figure (J.3). For both models, the hard cylinder B is represented as a perfectly elastic solid with a Young's modulus of 207 GPa. It is supported by a block A of low modulus (4 GPa) to allow it to ride up to form a stable plastic wave. The soft metal C is represented as linear isotropic hardening solid with a Young's modulus of 70 GPa, a tensile yield strength of 280 MPa and a hardening modulus of 4 MPa. A value of $k = 180$ MPa has been taken for the calculation of N/kR . Four-noded elements were used throughout (Visco 106 for the 2011, Plane 42 for the rest) to allow the contact to be modelled with the software's contact elements (contact 48). The friction at the interface was set to zero, as the model would not converge if friction were present.

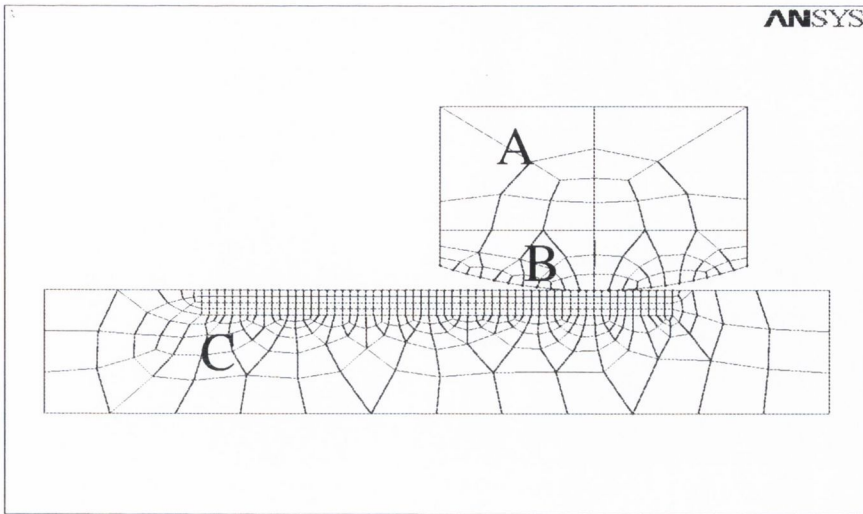


Figure J.1: Full cylinder model

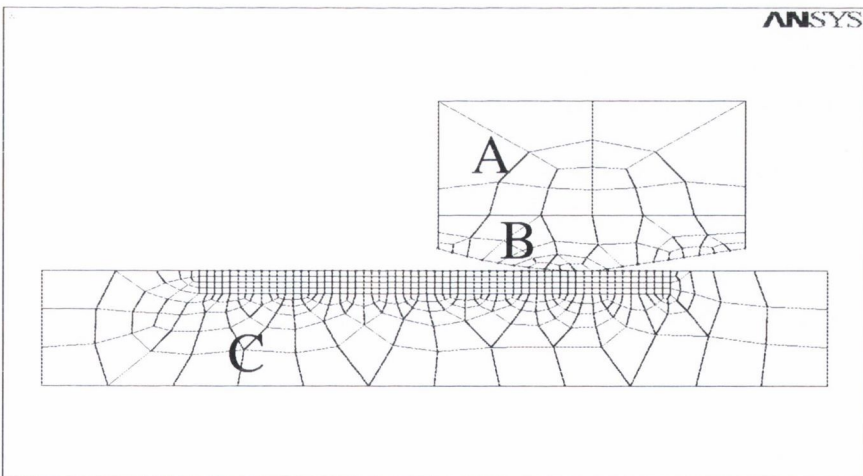


Figure J.2: Cut cylinder model

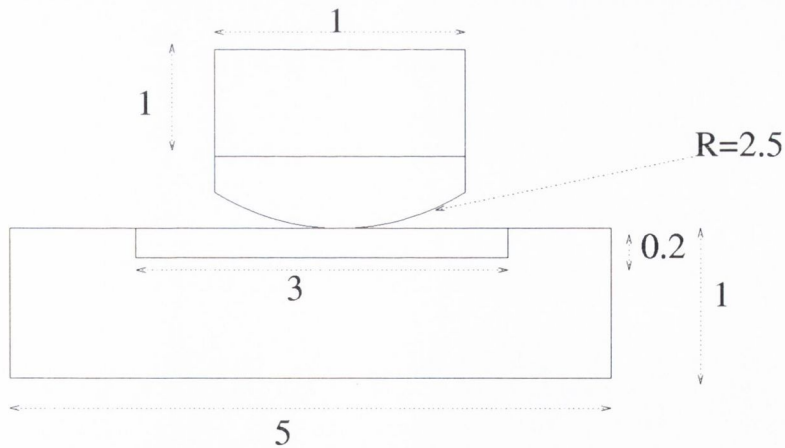


Figure J.3: Size of the models in mm

J.0.4 Scheme of the simulations

The simulations are split into two parts:

1. firstly, the rigid cylinder is indented into the soft surface to impose some degree of penetration. A vertical displacement Δy is imposed on the block C.
2. secondly, the cylinder B and the block C are translated horizontally.

The details of the simulations performed are given in tables (J.1) and (J.2) for the full cylinder and for the cut cylinder respectively.

The simulation with a full cylinder and $\Delta y = 0.15$ mm requires 17 hours of CPU time running on a 450 MHz Pentium 2 PC with 64 Mb RAM.

A sequence for this simulation is shown in figure (J.4), where the friction coefficient μ and the effective vertical displacement $\Delta y_e/R$ of the cylinder are plotted versus the imposed horizontal displacement $\Delta x/R$. Though the friction coefficient reaches a constant value at the end of the simulation, it can be seen that the cylinder gradually climbs slightly back towards the free surface level but does not reach the original free surface level as in the slipline field model. Thus steady-state conditions are not perfectly achieved in these simulations.

Δy in mm	N in N.	N/kR	μ
0.15	1024	2.40	0.1600
0.13	911	2.14	0.1400
0.11	793	1.86	0.1100
0.09	660	1.55	0.1000
0.07	514	1.21	0.0700
0.06	433	1.02	0.0300
0.05	358	0.84	0.0300
0.04	277	0.65	0.0290
0.02	131	0.31	0.0050

Table J.1: Details of the FEA simulations for the full cylinder

Δy in mm	N in N.	N/kR	μ
0.15	949	2.23	0.2100
0.13	852	2.00	0.1800
0.11	752	1.77	0.1600
0.09	638	1.50	0.1200
0.07	495	1.16	0.0960

Table J.2: Details of the FEA simulations for the cut cylinder

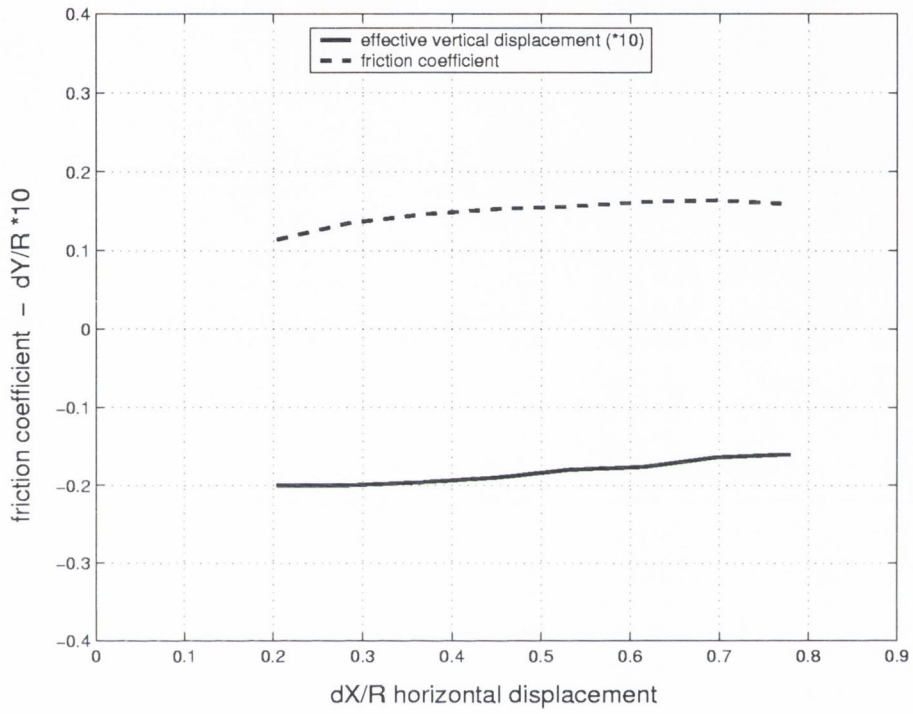


Figure J.4: dashed line: plot of μ - full line: plot of the effective vertical displacement $\Delta y_e/R$ of the cylinder - versus $\Delta x/R$, the imposed horizontal displacement

Appendix K

Friction data

This section provides the experimental data collected from the tests with the use of a full cylinder and a cut cylinder.

For a given test, the frictional and normal forces were time averaged to remove the effects of experimental noise and vibrations on the signal. For each set of tests, an example of the measured frictional and normal force is given.

K.0.5 Friction tests on aluminium

FULL CYLINDER EXPERIMENTS

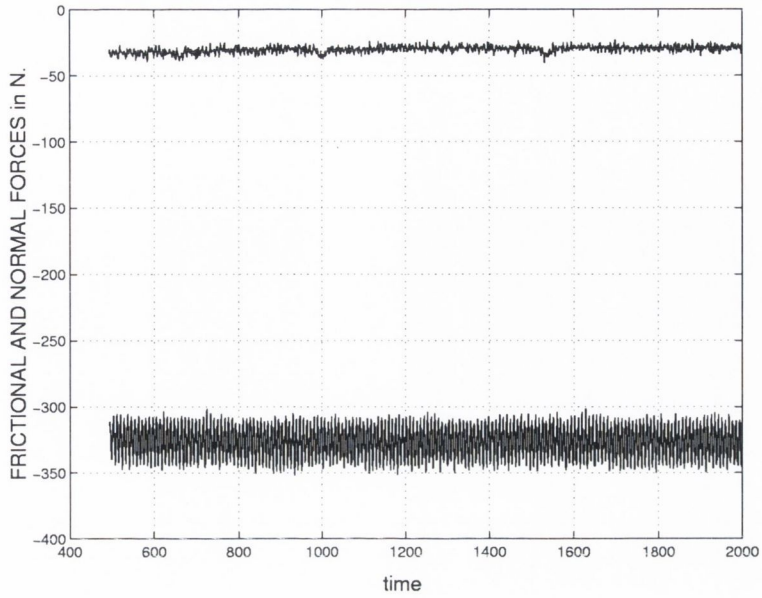


Figure K.1: Measured normal and frictional forces of a test with a full cylinder on aluminium

N in N	N/kR	μ			
174	0.152	0.1100	410	0.357	0.0910
211	0.184	0.0950	510	0.444	0.0890
307	0.267	0.1100	630	0.549	0.1020
409	0.356	0.1100	770	0.671	0.1160
515	0.449	0.1100	272	0.237	0.1140
610	0.532	0.1100	365	0.318	0.1150
715	0.623	0.1200	439	0.383	0.1150
795	0.693	0.1100	555	0.484	0.1200
885	0.771	0.1200	745	0.649	0.1400
635	0.553	0.1100	580	0.505	0.1120
620	0.540	0.0960	257	0.224	0.1240
617	0.537	0.1200	376	0.328	0.1390
213	0.186	0.0930			
327	0.285	0.0930			

Table K.1: Data for the full cylinder tests - Aluminium

CUT CYLINDER EXPERIMENTS

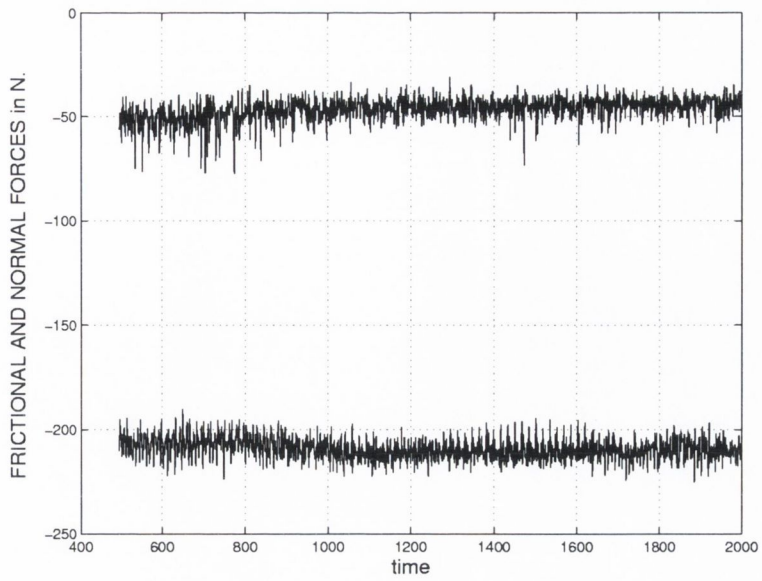


Figure K.2: Measured normal and frictional forces of a test with a cut cylinder on aluminium

N in N	N/kR	μ			
207	0.180	0.1700	307	0.266	0.1840
297	0.259	0.2270	346	0.301	0.1970
400	0.349	0.2460	381	0.332	0.2090
480	0.418	0.2570	446	0.389	0.2190
255	0.222	0.1790	504	0.439	0.2260
350	0.305	0.2120	526	0.458	0.2470
440	0.383	0.2740	493	0.430	0.2410
207	0.180	0.1760	187	0.163	0.1010
315	0.274	0.1860	234	0.204	0.1720
395	0.344	0.2660	289	0.252	0.1820
205	0.179	0.1930	301	0.262	0.1970
267	0.233	0.1950	378	0.329	0.2110
			261	0.227	0.182
			362	0.315	0.203
			460	0.401	0.226

Table K.2: Data for the cut cylinder tests - Aluminium

K.0.6 Friction tests on copper

FULL CYLINDER EXPERIMENTS

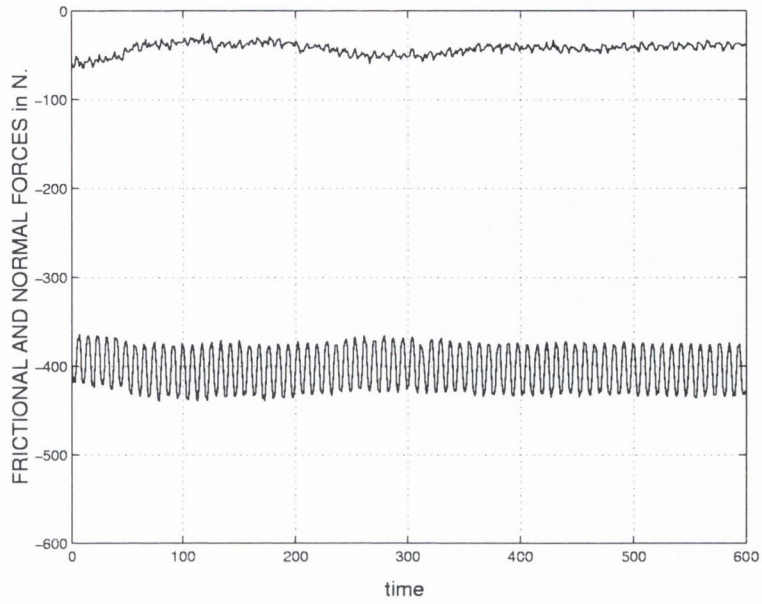


Figure K.3: Measured frictional and normal forces of a test with a full cylinder on copper

CUT CYLINDER EXPERIMENTS

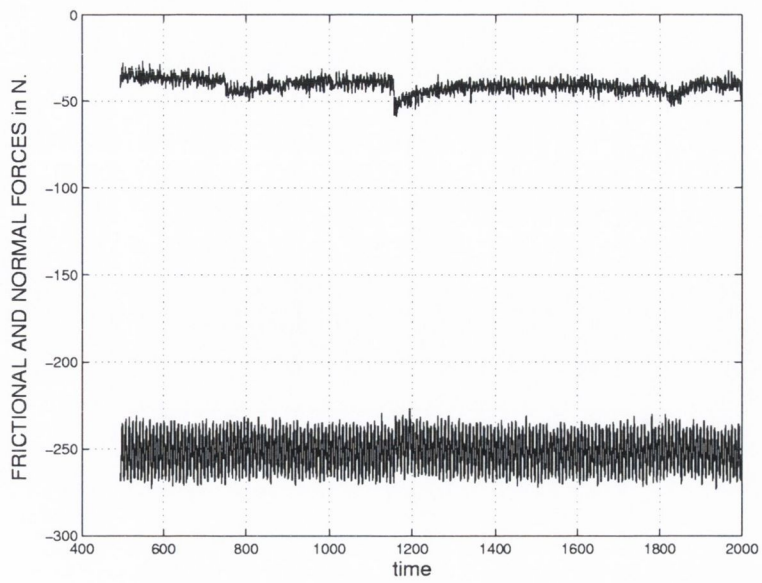


Figure K.4: Measured normal and frictional forces of a test with a cut cylinder on copper

N in N	N/kR	μ			
			466	0.523	0.1160
245	0.275	0.0780	520	0.584	0.1140
317	0.356	0.0990	560	0.629	0.1430
367	0.412	0.0940	625	0.702	0.1460
410	0.460	0.1220	720	0.809	0.1530
402	0.451	0.1080	505	0.567	0.1620
490	0.550	0.1110	610	0.685	0.1670
530	0.595	0.1330	715	0.803	0.1720
565	0.635	0.1120	520	0.584	0.0980
415	0.466	0.1400	620	0.696	0.0880
450	0.505	0.1500	760	0.854	0.1430
156	0.175	0.1300	460	0.517	0.1200
220	0.247	0.1260	245	0.275	0.1010
267	0.299	0.1130	301	0.338	0.1140
321	0.361	0.1060	362	0.407	0.1040
379	0.426	0.1270	466	0.523	0.1160
414	0.465	0.1260	520	0.584	0.1140
450	0.506	0.1300	560	0.629	0.1430
500	0.562	0.1340	625	0.702	0.1460
545	0.612	0.1440	720	0.809	0.1530
245	0.275	0.1010	505	0.567	0.1620
301	0.338	0.1140	610	0.685	0.1670
362	0.407	0.1040	715	0.803	0.1720

Table K.3: Data for the full cylinder tests - Copper

N in N	N/kR	μ
251	0.282	0.1630
216	0.242	0.1750
314	0.353	0.1450
411	0.462	0.1390
520	0.584	0.2370
193	0.217	0.0778
241	0.271	0.1370
300	0.337	0.1350
337	0.379	0.1620
409	0.459	0.1860
530	0.595	0.2530
221	0.248	0.1060
338	0.379	0.1250
465	0.522	0.2190
165	0.185	0.1400
202	0.227	0.1240
232	0.261	0.1300
310	0.348	0.1240
357	0.401	0.1500
410	0.470	0.1530

Table K.4: Data for the cut cylinder tests - Copper

Appendix L

Compression tests

The compression tests have been performed using a standard test method. The specimen were shaped as bars, with a length of $L = 38\text{mm}$ and a diameter of $D = 13\text{mm}$. In figures (L.1) and (L.2), one of the tests performed are presented for aluminium and copper respectively.

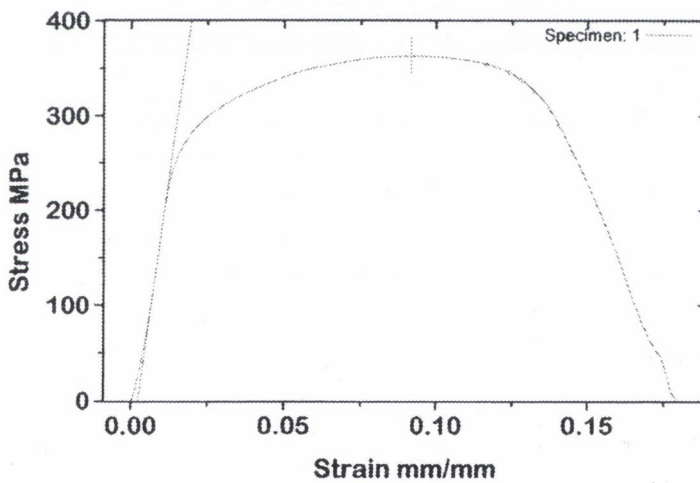


Figure L.1: Compression test on aluminium

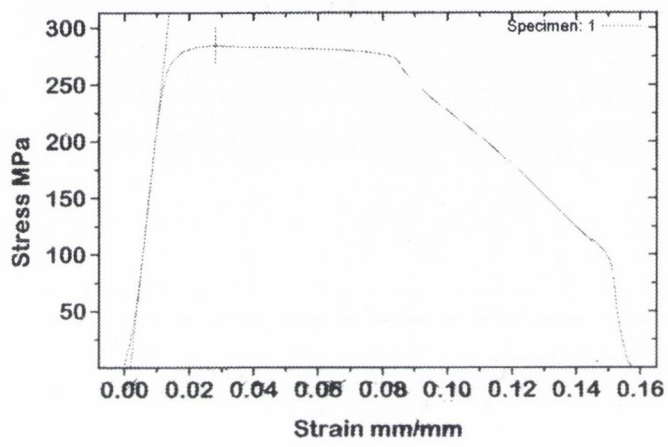


Figure L.2: Compression test on copper